Doctoral Thesis in Physics

Tunnel magneto-Seebeck effect: Improving the effect size

Spintronics and spincaloritronics

Alexander Böhnke

July 21, 2016

Bielefeld University
Department of Physics

Declaration

I wrote this thesis by myself and used none but the indicated resources. Text and figures were partly taken from corresponding publications, which originate directly from this work.

(Alexander Böhnke)

Reviewers:

Prof. Dr. Günter Reiss, Bielefeld University

Prof. Dr. Christian Heiliger, Justus-Liebig-Universität Gießen

Printed on non-aging paper ISO 9706
Bielefeld University, Department of Physics
Center for Spinelectronic Materials & Devices

Doctoral thesis
July 21, 2016

Contents

Chapter 1

Introduction

The emerging field of spin caloritronics[1,2], which focuses on the interaction between spin and heat transport in materials, has gained strong interest in recent years. Primarily the prospect that thermal spin transport enables new mechanisms for thermal-to-electric energy conversion, makes the investigation of spin caloritronic effects particularly interesting for energy conversion applications, e.g., waste heat recovery in modern electronics. A promising approach to attain this objective is the tunnel magneto-Seebeck (TMS) effect.

The TMS effect was predicted from *ab initio* theory by Czerner *et al.*[3] and experimentally discovered by Walter *et al.*[4] and Liebing *et al.*[5] in Co-Fe-B/MgO/Co-Fe-B magnetic tunnel junctions (MTJs) in the year 2011. MTJs are nanopatterned spintronic devices that consist of a nanometer thick insulating tunnel barrier (e.g., MgO) sandwiched between two ferromagnetic electrodes (e.g., Co-Fe-B). The fundamental mechanism behind the TMS effect is the altering of the Seebeck coefficients in an MTJ when the relative alignment of the magnetizations of the electrodes is reversed. If a temperature gradient is applied to the MTJ, this altering of the Seebeck coefficients can be observed as a change of the Seebeck voltage. No additional power source that provides a bias voltage is needed to obtain this signal. Thus, the readout of the MTJs by the TMS effect allows the use of waste heat generated in electronic devices to operate, e.g., memories or sensors,

without an additional power source. This makes the TMS effect particularly interesting for reducing the power consumption of future electronic devices.

One important benefit of the TMS effect, compared to other spin caloritronic effects, like the Spin-Seebeck effect[6,7], is the fact that it is observed in MTJs, which are already implemented in up-to-date electronic devices, such as hard discs or random access memories. Today, the readout of these devices is performed via the tunnel magnetoresistance effect (TMR) under an externally applied bias voltage. The TMR effect describes the change of the resistance of an MTJ depending on the relative magnetization orientation of its ferromagnetic electrodes. It was first discoverd by Julliere using Fe/Ge-O/Co tunnel junctions in 1975[8]. Today, the insulating layer mostly consists of amorphous Al_2O_3 or crystalline MgO[9,10] in combination with a wide range of electrode materials, such as ferromagnetic alloys[11], Heusler compounds[12], superconductors[13], and even antiferromagnets[14]. Intense research has led to stable logic devices with effect ratios of several hundred percent. The versatility and robust nature of MTJs has made them the backbone of modern spintronics[15,16]. Carefully designed MTJs enable effects like spin-transfer torque or spin-orbit torque switching. These discoveries opened a broad field for new devices, such as the magnetoresistive random-access-memory (MRAM). This variety of new effects in combination with the adaptable material parameters of MTJs makes them particularly interesting for the use in spin caloritronic devices.

Although these facts already reveal the large potential of MTJs, the relatively new spin caloritronic counterpart to the TMR effect, the TMS effect, has gained relatively little attention when considering the development of new devices. The reasons for this lack of interest are most likely due to the low Seebeck voltages of only a few microvolt, and the low effect ratios of only a few percent, being much less than for the established TMR effect. However, so far only Co-Fe or Co-Fe-B based MTJs with MgO or Al_2O_3 barriers have been investigated[4,5,17–25]. These material combinations have proven to be ideal for high TMR effect ratios. Nonetheless, this does not necessarily imply their suitability for the generation of high TMS effects, due to the different transport mechanisms[4]. Accordingly, it is not surprising that recent *ab initio* calculations by Geisler and Kratzer[26] predict higher TMS effects for MTJs that contain half-metallic Heusler compound electrodes.

The scope of this work is, to obtain a simplified, yet accurate model for the prediction of high TMS effects to enable a fast material screening. Furthermore, this study aims at an experimental evidence that MTJ devices with tailored density of states (DOS), in particular with half-metallic Heusler compound electrodes, can significantly improve the TMS effect.

In order to obtain information on the thermoelectric transport in the MTJs, the Landauer-Büttiker formalism [27] is applied and the influence of different DOSs on the size of the Seebeck coefficients and the TMS effect is evaluated.

To prove the feasibility of the proposed material parameters, the TMS effect is investigated using a number of different methods and on various types of MTJs. In this context, firstly, a new method for shifting the chemical potentials through the DOS of the electrodes by using an external bias voltage and simultaneously determining the Seebeck effect in the MTJs is introduced. Secondly, it is investigated whether the nearly half-metallic Heusler compounds Co_2FeAl and Co_2FeSi provide the desired high TMS ratios.

This thesis is organized as follows: In Chapter 2 the theoretical foundation for the effects that are treated in the experimental sections are presented. This includes a detailed introduction to the TMR and Seebeck effects. With this knowledge the TMS effect is derived, and a model, based on the DOSs and the transmissions of the MTJs in the Landauer-Büttiker formalism, is elaborated. This includes a method to obtain the TMS effect size from the shape of the DOS. Additionally, the nonlinearized Landauer-Büttiker formalism is used to investigate the TMS effect under an applied bias voltage. Furthermore, the nonlinearized formalism can be applied to study the influence of the temperature dependent shifts of the chemical potentials in the electrodes on the Seebeck coefficients.

In Chapter 3 the methods and techniques necessary for the experimental observation of the TMS effect are introduced. This chapter concentrates on the optical and electronic setup, and links the theory to the applied techniques. It also explains the sample design and the methods necessary for the preparation and characterization of the samples. Furthermore, COMSOL simulations are proposed for determining the temperature profile in the MTJs.

Chapter 4 presents the results obtained with the methods in Chapter 3. It begins with basic TMS experiments on Co-Fe-B/MgO/Co-Fe-B MTJs. This is followed by a discussion of the temperature profile in the MTJs for different heating scenarios. After this more general insight into the TMS effect, the analysis focuses more detailed on the connection of the TMS effect to the DOS of the MTJs. First, the behavior of the TMS effect under an applied bias voltage is revealed. This section of Chapter 4 also compares the experimental determined dependence of the Seebeck effect on an external bias voltage to the predicted results from the model in Chapter 2. Second, the TMS effect in Heusler based MTJs is investigated and compared to Co-Fe-B based MTJs. This includes a connection to the model, that has been derived from the Landauer-Büttiker formalism and the DOS in Chapter 2.

Finally, Chapter 5 summarizes the theoretical and experimental findings. It also gives an overview of ongoing experiments, and an outlook on new ideas for future investigations.

Chapter 2

Theoretical background

The TMS effect complements the well established TMR and charge Seebeck effects. Hence, a basic understanding of both effects is of significant importance for elaborating a theoretical framework. The precise descriptions of these effects are unavoidably connected to the concept of the density of states (DOS). Whereas atoms exhibit discrete energy levels, in periodic solids, that consist of a large number of atoms, these energy levels form bands. The exact shapes and positions of the bands are determined by the periodic lattice of the solid, e.g., its crystal structure, and the type of atom at each position of the lattice. Still the concept of bands does not yet clarify how many states are available for electrons. For gaining a number that describes this property, it is necessary to evaluate the number of electronic states that are available in a certain energy interval. This is taken care of by the DOS, which represents the number of available electronic states per energy[28]. The DOS largely determines the electronic properties of solids. Insulators, for example, exhibit a gap in the DOS that is too wide for charge carriers to be excited into the conduction band. Thus, they cannot conduct electrical current. In metals, the conduction bands are partly filled by electrons allowing an easy excitation of electrons into higher states and an easy charge transport. In semiconductors, a smaller gap is found than in insulators. This gap allows a thermal excitation of charge carriers from the valence bands into the conduction bands. For ferromagnets, e.g., the electrodes of the MTJs,

the DOS is different for spin-up and spin-down electrons[16]. In general, more states are available for spin-up electrons in the majority DOS, than for the spin-down electrons in the minority DOS. This imbalance between the two spin species explains the presence of the macroscopic magnetic moment of ferromagnetic materials. Furthermore, the abundance of one sort of spin can lead to a spin-polarized charge transport in ferromagnetic materials.

In the first two sections of this chapter, the TMR effect and the charge Seebeck effect are explained based on the DOS. In the second part of the theory chapter the TMS effect is introduced. First, it is discussed in a similar fashion as the TMR and charge Seebeck effects, by using the DOS. Afterwards, the Landauer-Büttiker formalism is presented. It combines the concept of the charge Seebeck effect based on the DOS with the tunneling process in the MTJs. In other words, this formalism connects the DOSs of the electrodes to the electronic properties of the tunnel barrier. The linearized form of this formalism is particularly useful for the derivation of the transport coefficients, i.e., the conductance and the Seebeck coefficient, of the MTJs. Hence, this linearized form is used to discuss the size of TMS effects for different material combinations by comparing their DOSs and transmissions.

The nonlinearized form of the Landauer-Büttiker formalism allows the implementation of two gradients across the barrier, e.g., a temperature difference and a voltage drop. This description is applied to treat the bias dependence of the TMS effect and the influence of the temperature dependence of the chemical potentials in the electrodes.

2.1. Tunnel magnetoresistance

Before immersing more deeply into the subject of spin caloritronic effects in MTJs, this section provides a basic introduction to the well establish spintronic effect in MTJs known as tunnel magnetoresistance (TMR). It is crucial to understand the physics behind the TMR effect to pinpoint the differences and similarities between the TMR effect and its spin caloritronic counterpart, the TMS effect (section 2.3), as both are observed in equivalent sample structures. The following sections present a summary of the most

important theoretical background for the TMR effect, as it can be found in, e.g., Refs. 16 and 29.

Figs. 2.1a and b sketch the schematic cross section of an MTJ consisting of two metallic ferromagnets separated by a thin insulating layer. The insulator acts as a tunnel barrier for charge carriers traveling between the two ferromagnetic electrodes. The indicated tunneling current is driven by an external bias voltage V_{bias} applied to the electrodes, allowing the determination of the resistance of the MTJ. Fig. 2.1a depicts the MTJ in a state with the magnetization of both ferromagnets aligned antiparallel. For most material combinations this is the state of high resistance. When the magnetization direction of one of the ferromagnets is reversed (Fig. 2.1b) a parallel orientation of the two magnetizations is achieved, and the MTJ reaches its state of low resistance. For simplicity, in the following these two characteristic states are referred to as the antiparallel (ap) and parallel (p) state of the MTJ with the resistances R_{ap} and R_{p}, respectively. To size the change of resistance the effect ratio (TMR ratio) is defined:

$$\mathrm{TMR} = \frac{R_{\mathrm{ap}} - R_{\mathrm{p}}}{R_{\mathrm{p}}} \tag{2.1}$$

2.1.1. The TMR in the free electron model

The first simple explanation for the origin of the TMR effect was given by Julliere[8]. According to his model, the origin of the high and low resistance states can be attributed to the spin-polarization of the ferromagnetic electrodes and spin-polarized tunneling through the barrier. This simplisitc model has been extended by Slonczewski[30] by employing the DOS of the ferromagnetic electrodes $D(E)$ and the elastic tunneling through a rectangular potential barrier to deduce the currents crossing the MTJ. The DOSs of the individual ferromagnetic electrodes are described by the DOS of a free electron gas[31] $D(E) \propto \sqrt{E}$ as sketched in Figs. 2.1c,d. The ferromagnetism of the electrodes is introduced by the exchange splitting, which relatively shifts the DOSs for majority (spin-up) and minority (spin-down) charge carriers. As the applied bias-voltage moves the DOSs left and right of the barrier up or down in energy, the chemical potential μ of one electrode lies

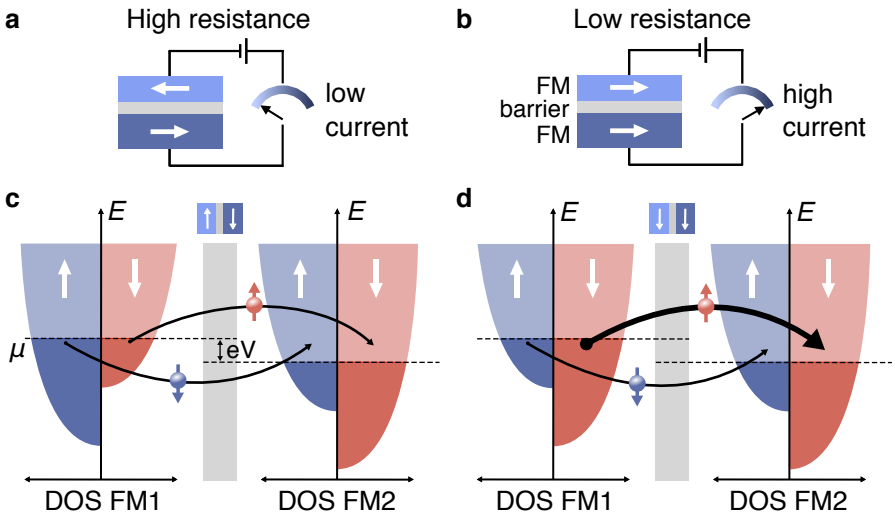

Figure 2.1. The tunnel magnetoresistance effect: Schematic drawing of an MTJ with bias voltage source and ammeter with, **a** antiparallel, and **b** parallel magnetization alignment of the ferromagnetic (FM) electrodes. **c, d** Corresponding density of states (DOS) of the MTJ. The white arrows indicate the direction of the magnetic moments of the electronic states. The black arrows represent the currents crossing the tunnel barrier for each spin orientation. The thickness of the arrows mirrors the size of the current.

lower in energy with respect to the other, allowing electrons to tunnel from occupied into free states.

Since an intermixing of the conduction channels for spin-up and spin-down charge carriers is excluded, this model can be regarded as a two current model for the two spin channels. The current per channel is proportional to the quantity of occupied initial and unoccupied final states with the same spin within the energy interval between the chemical potentials of the electrodes. In the ap state (Fig. 2.1c) the tunnel probability is small, because the electrons travel between the majority DOS of one and the minority DOS of the other ferromagnet resulting in a small number of either initial or final states close to the chemical potentials. However, in the p state (Fig. 2.1d) the number of initial and final states in the majority states is large, such that

a large number of spin-up (red) electrons can tunnel. The resulting current is increased compared to the ap state generating the difference in resistance between these two states.

2.1.2. Coherent and incoherent tunneling

In addition to the DOSs of the ferromagnetic electrodes, the electronic structure of the barrier influences the tunneling process. A more detailed review of the influence of the barrier is given in Ref. 29, which serves as a basis for this section. For example, electrons tunnel differently trough an amorphous AlO_x barrier than through crystalline MgO [29,32,33]. This difference can be attributed to the coupling between the Bloch-states of the electrodes and the evanescent states of the barrier. As amorphous AlO_x exhibits no preferred crystallographic symmetries, Bloch-states with different orbital symmetry can couple equally well to evanescent states in the barrier and, thus, have similar tunneling probabilities. This process is called incoherent tunneling.

MgO, however, possesses distinct symmetries, because of its crystalline structure. Consequently, Bloch-states from the electrodes with Δ_1 symmetry can effectively couple to the evanescent states in the barrier, resulting in a coherent tunneling. This coherent tunneling enhances the tunneling probability for the Δ_1 states, which hold a higher spin-polarization in commonly used ferromagnets (e.g., Fe [34], Co [35], Co-Fe [10], Co-Fe-B [36,37], and Heusler compounds [38]). Therefore, the TMR ratio of MTJs with an MgO barrier is increased compared to amorphous barrier materials (e.g., AlO_x). Recently, the benefical effect of coherent tunneling on the TMR has also been reported for Mg-Al-O barriers [39,40].

2.2. Charge Seebeck effect

After the basics of electron tunneling between two ferromagnets under an applied bias voltage have been introduced in the last section, this section gives an overview on the thermoelectric transport, or Seebeck effect, in conductors. It is based on Refs. 28,41,42.

The classical or charge Seebeck effect was discovered by Thomas Johann Seebeck in the year 1821. Phenomenologically, it describes the generation

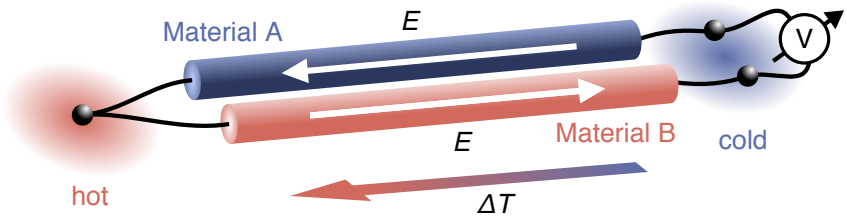

Figure 2.2. Thermocouple consisting of materials A and B with Seebeck coefficients of opposing sign. The cold junctions are connected to a voltmeter that measures the total effective difference in the electric potential along the whole conductor loop[43].

of a voltage along a temperature difference ΔT in a metal or semiconductor[41,42]. The Seebeck voltage or thermovoltage V is proportional to the temperature difference and the Seebeck coefficient S:

$$V = -S\Delta T \tag{2.2}$$

Since this effect is the basis for all spin caloritronic effects that include charge transport, e.g., the TMS effect, this section provides a summary of the most important concepts. This should enable the reader to qualitatively understand the connection of the size of the Seebeck coefficients with the density of states and the occupation function.

2.2.1. A practical view of the Seebeck effect

Experimentally, Seebeck voltages are usually determined using a thermocouple (Fig. 2.2), i.e., a conductor loop consisting of two materials A and B with different Seebeck coefficients S_A and S_B. At one junction the thermocouple is heated to the temperature T_hot, while the other ends of the conductors are connected to the ports of a voltmeter at a lower temperature T_cold. The total voltage measured by the voltmeter is

$$V = \left(S_\mathrm{B} - S_\mathrm{A}\right) \cdot \left(T_\mathrm{hot} - T_\mathrm{cold}\right). \tag{2.3}$$

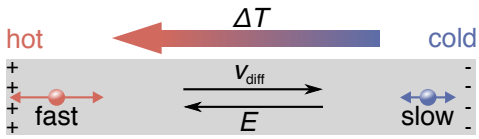

Figure 2.3. Thermal diffusion: Electrons diffuse to the cold end of the conductor. The accumulation of negative charges at the cold end leads to an electric field pointing from cold to hot.

This equation points out that for practical measurements two different materials with $S_A \neq S_B$ have to be used, because, otherwise, the Seebeck voltages along the conductor loop cancel out.

But how are these voltages generated in the first place? In a simple picture, such as in the Drude-Sommerfeld model, the movement of electrons in a metal is described as a gas of interacting particles. Hence, the electrons move with a mean thermal velocity. If this model is applied to the Seebeck effect, different electron velocities are obtained along the wire, because of the temperature difference (Fig. 2.3). Electrons at the hot end move faster than electrons at the cold end. These different velocities result in a net electron diffusion from the hot to the cold end causing a charge imbalance along the conductor. This diffusion current generates an electric field E, which then generates an opposing drift current. In the stationary state, the drift and diffusion currents compensate, which results in a stationary electric field. This generated electrical field can be expressed as an electric potential gradient $-d\phi/dz$ along the conductor, which can be measured as a Seebeck voltage [28].

As this description is derived from the Drude-Sommerfeld model, it is only valid for a free electron gas. In a real solid conductor, however, the electron transport is strongly dependent on the band structure and the related DOS of the material. This dependence explains why different materials possess different Seebeck coefficients. For instance, the Seebeck coefficients of semiconductors change sign when instead of a p-type ($S > 0$) an n-type ($S < 0$) material is observed. This is attributed to the different types of carriers contributing to the charge transport. In an n-type semiconductor

electrons carry the diffusion current, resulting in a negatively charged cold end of the semiconductor. In a p-type semiconductor the holes mainly contribute to the diffusion. This leads to a positively charged cold end of the semiconductor. Conclusively, the generated voltages have opposite signs. This also reverses the sign of the Seebeck coefficient according to Eq. 2.2. However, exclusively considering diffusion currents is not sufficient to accurately describe the Seebeck effect and a deeper understanding is imperative for the optimization of materials with respect to their Seebeck coefficients.

2.2.2. Influence of the density of states

For a detailed qualitative understanding of the connection between the DOS and the Seebeck coefficients, the available charge carriers in the vicinity of the chemical potential μ have to be considered. The following descriptions are mostly based on Ref. 31. The density of available electrons $n(E)$ with an energy E is specified by the DOS $D(E)$ multiplied by the occupation function, namely, the Fermi-Dirac statistics $f(E)$:[31]

$$n(E) = D(E)f(E) = D(E)\frac{1}{1+\exp\left(\frac{E-\mu}{k_\mathrm{B}T}\right)}, \tag{2.4}$$

where k_B is the Boltzmann constant, and T the temperature. For zero temperature the Fermi-Dirac distribution describes a step function with the step at the Fermi energy $\mu(T = 0\,\mathrm{K}) = E_\mathrm{F}$, but for higher values the function is smeared out in a range of a few $k_\mathrm{B}T$. As $n(E)$ is the density of occupied states per energy E, states are occupied below and unoccupied above E_F at $T = 0\,\mathrm{K}$. Fig. 2.4 features three different characteristic DOSs. Each graph sketches the occupation around μ in the cold ($T = 0\,\mathrm{K}$) and the hot end of the material according to the Fermi-Dirac distribution. In general, electrons travel between occupied states and free states, which means that electrons above μ can travel from hot to cold, whereas electrons below μ travel from cold to hot. In this picture, a high Seebeck coefficient is expected when one of the currents is much larger than the other, resulting in a large net current from one end of the material to the other.

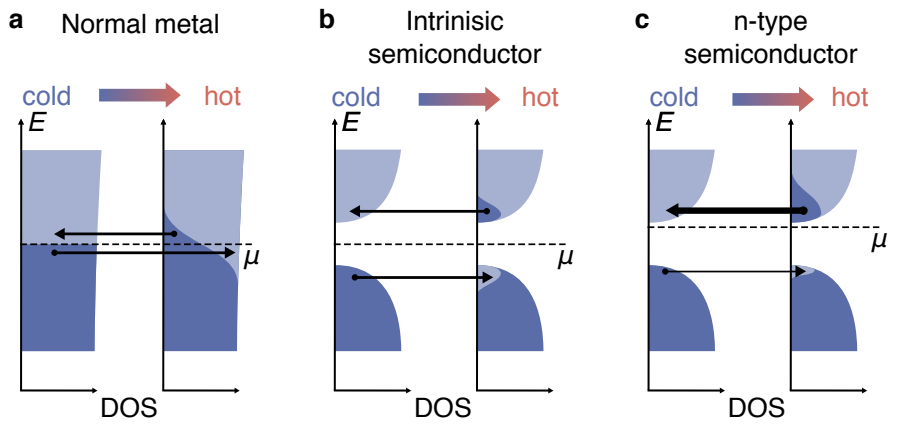

Figure 2.4. Seebeck effect for different DOSs: **a** In a metal the amount of occupied states below μ is similar to the number of unoccupied states above μ. Accordingly, the net current between hot and cold is small, resulting in low Seebeck coefficients. **b** In an intrinsic semiconductor the amount of occupied states in the conduction band equals the amount of unoccupied states in the valence band. This also leads to a small net current and low Seebeck coefficients. **c** In an n-doped semiconductor μ is shifted towards the conduction band, allowing more electrons to be excited from the donor levels into the conduction band than holes generated in the valence band. This results in an increased electron current from hot to cold and higher Seebeck coefficients.

Neglecting the energy dependent mobility of charge carriers in conductors, an important relation between the DOS and the value of the Seebeck coefficient is already identified by considering the model DOS of three different materials, i.e., a metal, an intrinsic semiconductor and a heavily doped n-type semiconductor (Fig. 2.4).

In a metal with a flat DOS (Fig. 2.4a) the two aforementioned opposing currents have the same size, because of the similar amount of occupied and unoccupied states above and below μ. In an intrinsic semiconductor (Fig. 2.4b) the DOS looks differently, due to the band gap between the valence and the conduction bands. Nonetheless, the net current is still small, because μ is positioned in the middle of the gap. Only if donor states are introduced that shift μ towards the conduction band (Fig. 2.4c) exist more

occupied states in the conduction band above μ than free states (holes) in the valence band below μ. This imbalance generates a sizable net current from hot to cold resulting in a large negative Seebeck coefficient. For a p-type semiconductor μ is shifted towards the lower edge of the gap, evoking more unoccupied electron states (occupied hole states) in the valence band. Therefore, the net current is reversed and a large positive Seebeck coefficient is expected.

Hence, two essential mechanisms are extracted from the dependence of the Seebeck coefficients on the DOS. First, the slope $dD(E)/dE$ of the DOS in the vicinity of μ influences the height of the Seebeck coefficient. For a flat DOS (Fig. 2.4a) the Seebeck coefficient is small. Only if the slope is steep is the Seebeck effect increased. A DOS with a gap to separate the electron transport above and below μ is even more beneficial. Second, a high slope of the DOS alone does not lead to a high Seebeck effect. Only if the DOS is asymmetric with respect to μ is the Seebeck coefficient large. For example, this is realized when μ is not positioned in the middle of the gap of a semiconductor.

Neglecting the mobility is a highly simplified approach and, therefore, it should be treated with great caution. However, in Sec. 2.3.3 it will be shown that in a lot of cases this straightforward picture can reveal the same information about the suitability of a material for spin caloritronic devices as a more sophisticated description.

2.3. Tunnel magneto-Seebeck effect

In the course of the last sections, a fundamental understanding of the charge Seebeck effect (Sec. 2.2), and the spin dependent tunneling in MTJs (Sec. 2.1) which constitutes the basis for the TMR effect was gained. In this section this knowledge about the thermal transport and the spin degree of freedom is combined to obtain a deeper insight into the TMS effect.

The TMS effect [4,5,17,18,20,23–25] describes the altering of the Seebeck coefficients S_p and S_ap of an MTJ by switching the magnetization alignment of the ferromagnetic electrodes between the p and ap state. Experimentally, the size of this change is determined by applying a temperature difference

ΔT across the tunnel barrier and measuring the generated Seebeck voltage $V_{\mathrm{p,ap}} = -S_{\mathrm{p,ap}}\Delta T$ as sketched in Fig. 2.5a,b. This method assumes a constant ΔT for both states of the MTJ. To size the effect, the TMS ratio [4] is defined in the style of the TMR ratio as

$$\mathrm{TMS} = \frac{S_{\mathrm{p}} - S_{\mathrm{ap}}}{\min\left(|S_{\mathrm{p}}|, |S_{\mathrm{ap}}|\right)} \overset{\Delta T_{\mathrm{p}} = \Delta T_{\mathrm{ap}}}{=} \frac{V_{\mathrm{ap}} - V_{\mathrm{p}}}{\min\left(|V_{\mathrm{ap}}|, |V_{\mathrm{p}}|\right)}. \tag{2.5}$$

As the $S_{\mathrm{p,ap}}$ and the voltages can be negative, the division by the minimum of the absolute values is inevitable.

2.3.1. The TMS in the free electron model

In this thesis a simplistic description is introduced which highlights that the origin of the TMS effect is ascribed to the DOSs of the electrodes (Figs. 2.5c,d). Therefore, the free-electron model for the electrodes (like for the TMR effect, Sec. 2.1) and the simplified model for the charge Seebeck effect (Sec. 2.2) are combined. In the TMR effect, the bias voltage causes a relative shift of the chemical potentials μ in the electrodes, which evokes the tunnel current. In the TMS effect the temperature gradient is the driving force for electrons to cross the tunnel barrier. The resulting diffusion currents are described analogously to the ordinary charge Seebeck effect (Sec. 2.2). Assuming the DOS of the free-electron model $D(E) \propto \sqrt{E}$, the current from hot to cold above μ is higher than the reversed current from cold to hot below μ. This is attributed to the slightly larger amount of occupied states above μ and the enhanced transmission of electrons with higher energy [44].

However, in the TMS effect that is based on the tunneling between ferromagnetic electrodes a distinction between the two spin-channels is made. Since spin-flip processes are neglected during the tunneling process, again, the transport of charge carriers over the barrier is treated individually for both spin-channels, similarly to the TMR effect (cf. Sec. 2.1). In the ap state of the MTJ (Fig. 2.5c) the currents in both spin channels are small, because of a lack of either initial or final states (all contributing current paths are marked by arrows). The small net current over the barrier in both spin-channels results in a small Seebeck coefficient S_{ap} and, hence, a small voltage V_{ap}.

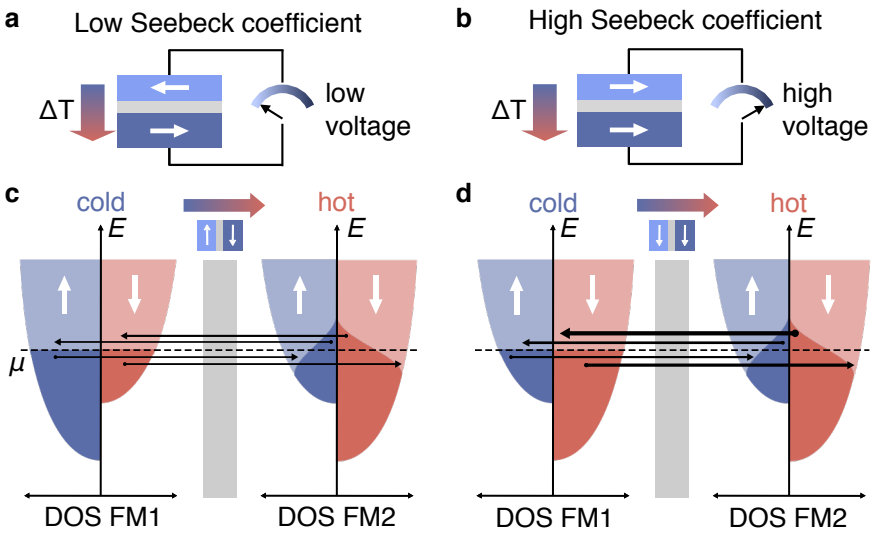

Figure 2.5. The tunnel magneto-Seebeck effect: a, b For determining the Seebeck coefficients $S_{\mathrm{p,ap}}$ in the antiparallel and the parallel state, respectively, a temperature gradient is applied across the MTJ and the generated Seebeck voltages $V_{\mathrm{p,ap}}$ are measured. **c, d** Sketches of the DOS for a cold $T = 0K$ (FM1) and a hot (FM2) ferromagnet in the free-electron model for the ap and the p states, respectively. The broadening of the occupation is exaggerated for illustration purposes. The black arrows indicate the direction of electrons passing the barrier. The width of the arrow symbolizes the size of the corresponding diffusion current. A high net current leads to the generation of a large electric field, resulting in a large Seebeck coefficient.

In the p state the number of states in the spin-up channel is increased (marked by thicker arrows). This increase gives rise to a slightly larger net current and, thus, a larger Seebeck coefficient S_{p} and a larger voltage V_{p}.

Although this model is highly simplified, it explains the first TMS experiments by Walter et al.[4] surprisingly well. For $Co_{26}Fe_{54}B_{20}/MgO/Co_{26}Fe_{54}B_{20}$ MTJs they find $S_{\mathrm{ap}} = -99.2\,\mu\mathrm{V\,K^{-1}}$ has a smaller absolute value than $S_{\mathrm{p}} = -107.9\,\mu\mathrm{V\,K^{-1}}$. This is particularly remarkable, since in this description any influence of the electronic structure of the barrier and the exact shape of the DOS on the tunneling process are neglected. Still, this simple picture based on the the free electron model with $D(E) \propto \sqrt{E}$ cannot be used for

real materials, because their DOS often exhibits features like gaps or peaks in the vicinity of the chemical potential that drastically influence the Seebeck coefficients[45]. This becomes obvious when looking at the Seebeck coefficients of $Co_{40}Fe_{40}B_{20}/MgO/Co_{40}Fe_{40}B_{20}$ MTJs. Here $S_{ap} = -232\,\mu V\,K^{-1}$ is found to be larger than $S_p = -223\,\mu V\,K^{-1}$ [17]. Therefore, the next section will investigate how the model can be adapted to describe real ferromagnetic materials and how the electronic properties of the barrier can be included.

2.3.2. Thermoelectricty in the Landauer-Büttiker formalism

So far, it has only been dealt with the descriptions of the classical Seebeck and the TMS effect in the free electron picture (Sec. 2.3.1), or in macroscopic bulk samples (Sec. 2.2). However, for the TMS effect the charge transport between two electrodes separated by a nanometer thick tunnel barrier has to be considered. Therefore, a description appropriate for the transport in the nano regime has to be employed.

For this purpose the Landauer-Büttiker formalism is introduced. The fundamental description of this formalism is based on Ref. 28. The description of thermoelectric transport in the Landauer-Büttiker formalism follows Ref. 27.

The general idea behind this formalism is sketched in Fig. 2.6. Two reservoirs at temperatures T_L and T_R, and chemical potentials μ_L and μ_R are connected by a channel that allows charge transport, e.g., ballistic conduction or elastic tunneling, as in MTJs. The current through the channel is influenced by the energy dependent transmission $\mathcal{T}(E)$ of the channel and the difference of occupation in the left and right reservoir $f_L(E) - f_R(E)$. As only small devices are investigated, the transport through the channel is treated as elastic, meaning that electrons entering the channel with the energy E on one side, also leave the channel with the same energy E on the other side. Elastic scattering is allowed. Under these assumptions the energy dissipation, e.g., the creation of heat due to the current, occurs in the reservoirs[46].

For a better understanding of the following formulas, two different transport scenarios are investigated (Fig. 2.6). First, a voltage is applied between the two reservoirs and the current is determined, as it would be done in a

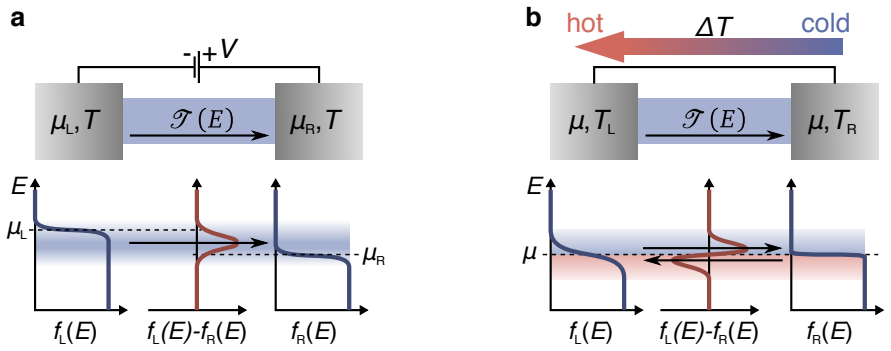

Figure 2.6. Landauer transport between two reservoirs with temperature $T_{L,R}$ and chemical potentials $\mu_{L,R}$. $f_{L,R}(E)$ are the corresponding occupation functions. The net current is proportional to the transmission $\mathcal{T}(E)$ between the reservoirs and the difference in the occupations $f_L(E) - f_R(E)$. A current is generated by, **a** applying a voltage V between the two reservoirs at a constant temperature T, or **b** a temperature difference $\Delta T = T_L - T_R$ under short circuit conditions ($\mu_L = \mu_R = \mu$).

resistance measurement. In a second example, a temperature gradient is applied to the reservoirs under short circuit conditions and the thermocurrent is determined. This gives access to the Seebeck coefficient of the system.

If a voltage $V = (\mu_L - \mu_R)/e$ is applied to the reservoirs at the same temperatures $T_L = T_R = T$, the occupation functions of the left and right reservoirs are shifted with respect to each other without changing their thermal broadening (Fig. 2.6a). Accordingly, the occupied states in the left reservoir have a higher energy than the occupied states in the right reservoir. This energy difference allows electrons to flow from left to right. Of course, only states in the interval between $f_L(E) - f_R(E)$ can contribute to the current. The shape of this difference with respect to the energy is displayed in red in the lower panel of Fig. 2.6b. As the transmission $\mathcal{T}(E)$ is energy dependent, not all of the states in the interval contribute equally to the transport. For obtaining the total current, the difference in occupation is multiplied by the transmission and it is summed over all energies:

$$I = \frac{2e}{h} \int dE \left[f_L(E) - f_R(E) \right] \mathcal{T}(E), \tag{2.6}$$

where e is the elementary charge and h is Planck's constant.

The description of the current in equation 2.6 is universally valid as long as the occupation function and the energy dependent transmission are known. For the example in Fig. 2.6a the difference of the two occupation functions is created by assuming different chemical potentials in the left and right reservoir, due to an applied voltage.

In Fig. 2.6b both reservoirs are electricly connected. Under these short circuit conditions, no voltage builds up and the chemical potentials $\mu_\mathrm{L} = \mu_\mathrm{R} = \mu$ are equal. The chemical potential, however, is not the only coefficient that influences the Fermi occupation of the reservoirs, but the temperature is an important parameter as well (cf. Eq. 2.4). Thus, applying a temperature gradient between the reservoirs results in a different broadening of the occupation functions $f_\mathrm{L}(E)$ and $f_\mathrm{R}(E)$ (lower panel of Fig. 2.6b). Again, this gives rise to a difference $f_\mathrm{L}(E) - f_\mathrm{R}(E)$, which changes sign around the chemical potential. This distribution implies that electrons above the chemical potential μ move from hot to cold (left to right), whereas electrons below μ move from cold to hot. At first sight, one might receive the impression that an equal amount of electrons travels in opposite directions and the net current amounts to zero. This would be true, if the transport did not depend on the energy dependent transmission $\mathscr{T}(E)$. The transmission contains the information on the transport mechanism in the channel, as well as the availability of states in the reservoirs depending on the DOS. This property of the transmission links the Landauer-Büttiker description to the aforementioned model of diffusive currents and their connection to different DOSs (cf. Sec. 2.2.2). Furthermore, with the transmission $\mathscr{T}(E)$ a parameter to include the electronic properties of the tunnel barrier into our model is found.

Two important properties of the transmission have been omitted so far. $\mathscr{T}(E)$ does not only depend on the energy E but also exhibits a dependence on the temperature T and the bias voltage V [47]. These parameters have to be taken into account when the Landauer-Büttiker formalism is used for the quantitative prediction of tunnel currents from *ab initio* theory (cf. Secs. 2.4.2 and 2.4.1). They are less important for the qualitative understanding of thermoelectric transport in the Landauer-Büttiker formalism, and, hence, are neglected in the following sections.

2.3.3. Linearized Landauer-Büttiker formalism

A widely used approach for the description of thermoelectric transport in the Landauer-Büttiker formalism has been introduced by U. Sivan and Y. Imry[27] in the year 1985. It is used by, e.g., Heiliger *et al.* and Kratzer *et al.* to perform *ab initio* calculations of the thermoelectric properties of MTJs, and other nanostructures[3,4,19,26,45,48,49]. This model assumes small voltages and temperature gradients, allowing a description of the current in the regime of linear response

$$I = \left(\Delta\mu/e + S\Delta T\right) \cdot G, \tag{2.7}$$

where $\Delta\mu$ is the difference in chemical potential and G is the conductance. Under open circuit conditions ($I = 0$), for example in a voltage measurement, this equation yields $V = \Delta\mu/e = -S\Delta T$, if no external voltage is applied. Hence, this expression resembles the equation for the Seebeck voltage (Eq. 2.2). In a closed circuit, e.g., in a current measurement with $V = \Delta\mu/e = 0$, a Seebeck current depending on the Seebeck coefficient and the conductance remains. Without a temperature difference $\Delta T = 0$, but under an externally applied voltage ($V \neq 0$) Ohm's law is obtained.

The values for the conductance and the Seebeck coefficient are derived by linearizing the universally valid Landauer transport equation (Eq. 2.6). Precisely, this approach is only correct for infinitesimally small differences of the chemical potentials and temperatures between the two reservoirs. Within these restrictions, the conduction is expressed as

$$G = -\frac{e^2}{h} \int dE \left(\frac{\partial f}{\partial E}\right) \mathscr{T}(E), \tag{2.8}$$

and the Seebeck coefficient results in

$$S = -\frac{1}{eT} \frac{\int dE \left(\frac{\partial f}{\partial E}\right) (E-\mu)\, \mathscr{T}(E)}{\int dE \left(\frac{\partial f}{\partial E}\right) \mathscr{T}(E)}. \tag{2.9}$$

A more detailed explanation of the derivation of the equations 2.8 and 2.9 is available in Appendix A.

2.3.4. The linearized and nonlinearized formalism

However, before this linearized formalism, as proposed by Sivan and Imry[27], is applied for further derivations, it is useful to investigate for which temperature gradients and voltages it is still valid. One important property of the MTJs that is neglected in the linearized model is the temperature dependence of the chemical potentials of the ferromagnetic electrodes. In some materials, e.g., in semiconductors with a large difference between the effective masses for holes and electrons, this effect can be very large. Since a temperature difference is generated between the electrodes, the shifts of the chemical potentials μ_L and μ_R in the left and the right electrode, respectively, are different. Thus, a temperature difference ΔT unavoidably generates a difference $\Delta\mu$.

The impact of an additional difference $\Delta\mu$, and hence the temperature dependence of the chemical potentials, can be investigated within the nonlinearized Landauer-Büttiker formalism. Such an investigation has recently been published by Geisler and Kratzer[26]. For the nonlinearized model that includes temperature dependent shifts of the chemical potentials, they set the constraint

$$0 \overset{!}{=} \frac{e}{h} \int dE \left[f_{\mu_\mathrm{L},T_\mathrm{L}}(E) - f_{\mu_\mathrm{R},T_\mathrm{R}}(E) \right] \cdot \mathscr{T}\left(E, \tfrac{\mu_\mathrm{L}-\mu_\mathrm{R}}{e}\right). \tag{2.10}$$

Since they do not allow a Seebeck current, they have to introduce a counter voltage to cancel this current. The size of this voltage resembles the Seebeck voltage obtained from the linearized Landauer-Büttiker formalism for small temperature gradients. They proved this assumption by computing the thermoelectric properties for a $Co_2MnSi/MgO/Co_2MnSi$ MTJ in the linearized Sivan-and-Imry-approach (Sec. 2.3.3) and the nonlinearized Landauer-Büttiker formalism. The Seebeck voltages obtained via the Sivan-and-Imry-approach are similar to the voltages calculated via the nonlinearized Landauer-Büttiker formalism with temperature dependent chemical potentials, as long as the temperature difference ΔT is small, i.e., a few mK.

Thus, their explanation presents an understanding of the Seebeck coefficient $S\left(T_\mathrm{L}\right)$ as a first order Taylor expansion coefficient of the counter voltage

$$V\left(T_\mathrm{L}, T_\mathrm{R}\right) = S\left(T_\mathrm{L}\right) \cdot \left(T_\mathrm{L} - T_\mathrm{R}\right) + \mathscr{O}\left(T_\mathrm{R}^2\right). \tag{2.11}$$

This interpretation clarifies why the two approaches give similar results for small temperature differences. Thus, it is acceptable to use the linearized Landauer-Büttiker formalism for the investigations of the TMS effect in MTJs, as long as the temperature difference is small and no large difference $\Delta\mu$ is generated. Hence, it is used for the following derivations.

2.3.5. The transmission and the chemical potential

The most important parameter in the Landauer-Büttiker formalism (Eqs. 2.8 and 2.9) is the transmission $\mathscr{T}(E)$, but for the Seebeck coefficient also the position of the chemical potential μ is of significant importance. For future considerations, a more detailed discussion of the influence of these parameters on the size of the conductance and the Seebeck coefficient is necessary. A similar investigation has been made in Refs. 50 and 51, which provide the basis for this section.

Taking a closer look at the integral in Eq. 2.8, it can be seen that the size of the conductance is given by the area under the curve $\left(\partial f/\partial E\right)\mathscr{T}(E)$. This picture emphasizes that mainly the states in an interval of a few $k_{\mathrm{B}}T$ around the chemical potential, these are namely those within the thermal broadening of the Fermi function $\left(\partial f/\partial E\right)$, contribute to the charge transport according to the transmission function $\mathscr{T}(E)$. In the following, this area is referred to as the occupied transmission.

The Seebeck coefficient (Eq. 2.9), can be deductively interpreted as the center of mass of the occupied transmission. The position of this center of mass is given with respect to the chemical potential μ, as indicated by the parenthesis $\left(E-\mu\right)$ in the numerator of Eq. 2.9.

Fig. 2.7 displays three model transmissions with the occupied transmission sketched in dark blue, and its center of mass marked by a red line. Three characteristic cases of shapes of the transmission are distinguished; in the first case (Fig. 2.7a), a large transmission without any distinct features is considered. Hence, the occupied transmission is equally distributed around the chemical potential. This symmetry results in the center of mass of the corresponding area being positioned at the chemical potential. Because of the large transmission, a large conductance is found for this case. The

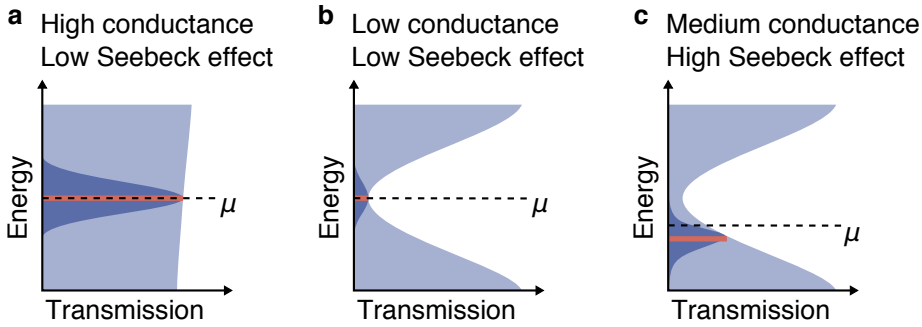

Figure 2.7. Seebeck effect and conduction dependence on transmission: For different transmissions $\mathcal{T}(E)$ (light blue), the area beneath $(\partial f/\partial E)\,\mathcal{T}(E)$ (dark blue), and its geometric center (red) are sketched for, **a** a large and symmetric transmission around μ, **b** a small and symmetric transmission around μ, and **c** an asymmetric transmission around μ.

Seebeck coefficient, however, tends to be small, because the center of mass and the chemical potential are found at the same energy.

In Fig. 2.7b the transmission exhibits a dent around the chemical potential. Thus, the occupied transmission is much smaller than in the first case. This results in a small conductance. Although, a transmission relatively rich in features is investigated, it is still symmetric with respect to the chemical potential, causing a symmetric occupation of the transmission with the center of mass at the chemical potential. Accordingly, the Seebeck coefficient also tends to be small.

In the third case (Fig. 2.7c), the transmission is shifted with respect to the chemical potential. The increase in transmission at the chemical potential enables an intermediate conductance in comparison to the first two cases. As the shift of the transmission also causes an asymmetric occupation, the center of mass shifts below the chemical potential revealing a non-vanishing Seebeck coefficient.

These examples can be summarized in two important statements. First, a high transmission around the chemical potential induces a large conductance. This is independent of the symmetry of the transmission with respect to the

chemical potential. Second, a high Seebeck coefficient can only emerge, if the transmission is asymmetric with respect to the chemical potential. It is, however, not directly associated with the actual area of the occupied transmission.

These findings can be related to the TMR and TMS effects. In an MTJ the transmission of spin-up charge carriers differs from the one of the spin-down charge carriers [47]. In other words, the MTJ has differently sized and shaped transmissions in the p and the ap state. For explaining this concept it is assumed that Figs. 2.7a and b are the transmissions of an MTJ in the p and the ap state, respectively. In this case the MTJ exhibits a high TMR effect, because the conductances of the p and the ap state show a large difference, which is visible from the different sizes of the occupied transmission. The TMS effect, however, is very small, because the center of mass is the same for the p and the ap state.

If, instead, the transmissions of Figs. 2.7b and c are compared, a smaller TMR effect is found, because the areas of the occupied transmissions change less between the p and the ap states. However, the TMS effect in this case is enhanced, as the center of mass moves from a symmetric (vanishing Seebeck coefficient) to an asymmetric (non-vanishing Seebeck coefficient) position with respect to μ. Consequently, a high TMR effect does not necessarily result in a high TMS effect, and vice versa [4].

2.3.6. The transmission and the density of states

In section 2.2.2 the influence of different DOSs on the Seebeck coefficients has already been discussed. In the Landauer-Büttiker formalism the DOS influences the transport only indirectly through the energy dependent transmission. However, investigations of the transmission of full devices, such as MTJs, are rare. In most cases, only *ab initio* calculations of the DOS are available (e.g. AFLOWLIB.org [52]) for making predictions on the electronic properties of the materials used as electrodes. This urges the need to understand the influence of the DOS on the transmission. Particularly, it is of great importance to determine the approximate asymmetry of the transmission from the DOS, as this is the key to easily distinguish between materials with high and low Seebeck coefficient.

The most reasonable approach for gaining a fundamental insight into how the DOS and the transmission are interconnected is density functional theory. This technique is used to calculate the DOSs and the transmission of simple devices, such as MTJs. The benefits of this technique are the accessibility of most parameters of the system, e.g., the electronic structure, the interfaces, the atomic positions in compounds, the material combinations, and the position of the chemical potentials. The main disadvantage of this method is the time consuming numerical computations necessary to obtain the results, in particular for the transmission of an MTJ.

One example of the successful application of this technique to Fe/MgO/Fe tunnel junctions has been published by Heiliger *et al.*[47]. In the first step, they extract the relationship between the local density of states (LDOS) at the Fe/MgO interfaces and the transmission. Besides the LDOS, they are able to identify another major influence on the transmission, namely the filter effect of the barrier material, which has also been predicted by Butler *et al.*[32] for MgO tunnel barriers. In the second step, they apply a bias voltage to the MTJ to relatively shift the DOSs of the two electrodes. This shift of the DOSs evokes that a peak in the transmission crosses the mean chemical potential $\left(\mu_{\mathrm{L}} - \mu_{\mathrm{R}}\right)/2$. They clearly attribute this peak to a peak in the LDOS of the electrodes. Thus, the work of Heiliger *et al.* suggests that, although the transmission is not directly connected to the DOS, it can be used as a first approximation for the transport properties of a tunnel junction.

In another work, Geisler and Kratzer[26] calculated the transmission and the (L)DOS of the Heusler compound based Co_2MnSi/MgO/Co_2MnSi MTJs. Their findings clearly reveal that the gap in the band structure of the minority spins of the Heusler compound electrodes is also found in the transmission of the whole MTJ.

Therefore, simply looking for a DOS with an asymmetric position of the chemical potential with respect to a feature, such as a gap, might be an efficient method for spotting materials that enable high Seebeck coefficients and high TMS ratios in tunnel junctions. This, however, is only valid, as long as it is kept in mind that also the electronic structure of the barrier and the interface can strongly influence the transmission, and, hence, the Seebeck coefficients.

2.4. Enhancing the tunnel magneto-Seebeck effect

In Secs. 2.3.5 and 2.3.6 the asymmetry of the transmission with respect to the chemical potential has been identified as the most efficient parameter for modifying the Seebeck coefficients of an MTJ. Furthermore, the asymmetry of the transmission has been linked to certain asymmetrical features of the DOS, such as peaks or gaps.

In this section, this knowledge is applied to obtain the properties of the optimum DOS, and hence, the optimized materials for high TMS effects. In this thesis the following theoretical descriptions are presented for the first time, and form the backbone for enhancing the TMS effect. As only the position of the chemical potential has to be shifted to alter the Seebeck coefficients, there is no need to modify the actual shape of the DOS. This suggests two approaches.

The most direct approach is replacing the material of the electrodes with a material that possesses a DOS that is rich in features. In most cases these features generate a large asymmetry of the DOS, which translates to an asymmetric transmission with respect to the chemical potential.

A more sophisticated approach is to start from a random material with a non-specific DOS and then modify the chemical potential. To generate a change in the Seebeck coefficient, e.g., to gain a high value, the chemical potential can be shifted externally to an energy where the transmission exhibits a large asymmetry. For example, it can be attempted to find the edge of a gap or a peak. This method strongly benefits from the fact that only the symmetry of the transmission in the vicinity of the chemical potential influences the Seebeck coefficient. Furthermore, from an experimental point of view it avoids the preparation of many samples with slightly different DOSs, provided that it is possible to find a mechanism to externally influence the position of the chemical potential. In the next section the theoretical background necessary for the experimental implementation of this approach is explained.

2.4.1. The influence of a bias voltage on the Seebeck effect

In the introduction to this section, it has been found that shifting the chemical potential with respect to the transmission is a powerful tool to quickly determine information on the interplay of these two material properties.

However, experimentally fulfilling this task is not easy. In this thesis it is found that the most straight forward solution is to simultaneously apply a bias voltage and a temperature difference between the electrodes of the MTJ. The bias voltage shifts the chemical potentials of the two electrodes by eV, causing two effects. Firstly, an additional charge current travels across the barrier, that is only generated by the bias voltage and does not contain any information on the Seebeck effect of the MTJ. Secondly, by varying the bias voltage, the DOSs of the individual ferromagnetic electrodes are scanned for features by the chemical potentials. The broadening of the occupation around the chemical potentials is different for the hot and the cold electrode and, thus, a Seebeck like property of the junction can be probed. A corresponding theoretical description of the phenomena involved in this process is developed in this thesis and is described in the next paragraphs.

The important aspect for the correct theoretical description is, that applying a bias voltage to the MTJ does not shift the mean chemical potential of the linearized Landauer-Büttiker formalism (Eqs. 2.8 and 2.9) through the transmission, but the chemical potentials of both electrodes have to be considered individually. Thus, the linearized Landauer-Büttiker formalism can no longer be applied. Instead, the nonlinearized expression for the current (Eq. 2.6) has to be used. As a drawback, there is no longer a direct link between the asymmetry of the center of mass and the magnitude of the Seebeck coefficients, as it is explained in Sec. 2.3.5. Still, the individual electrodes can be probed separately for their asymmetries.

Since the Seebeck contribution of the junction is desired, the fraction of the current that is only generated by the bias voltage $V_\mathrm{B} = \mu_\mathrm{R} - \mu_\mathrm{L}$ has to be removed. This is done by using a DC bias voltage and an AC heating. The static DC bias generates a DC current and the AC heating generates an AC current on top of this DC background. Feeding this signal to a narrow band-pass filter that removes the DC background and lets the AC signal pass, should yield the portion of the signal that is generated by a temperature difference

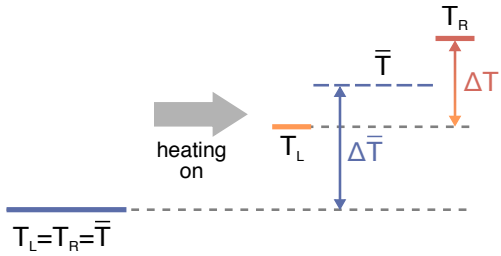

Figure 2.8. Temperatures in the MTJ when heated from one side: When the heating is switched on a temperature difference $\Delta T = T_R - T_L$ is generated. Simultaneously, the mean base temperature $\overline{T}$ rises by $\Delta\overline{T}$.

in the electrodes. However, heating the MTJ does not only generate a temperature gradient ΔT, but also elevates the mean base temperature $\overline{T}$ of the device. Fig. 2.8 illustrates the change of the temperatures from the cold to the heated MTJ. In the cold MTJ the temperatures of the left and the right electrodes, T_L and T_R, are equal to the mean temperature $\overline{T}$ of the MTJ. When the heating is switched on a temperature gradient ΔT is generated, but also the mean temperature is elevated by $\Delta\overline{T}$. Increasing the base temperature $\overline{T}$ results in a change of the resistance of the MTJ. This temperature dependence of the resistance is more pronounced in the ap state than in the p state [10]. Since the filter transmits all changes of the signal at a frequency equal to the modulation frequency of the heating, it does not block the change of current generated by the change of the base temperature. Hence, the filtered current still contains one component that is connected to a Seebeck effect and another contribution that is only generated by a change of the base temperature.

The current generated in the heated (hot) and cold MTJ is expressed by using the Landauer-Büttiker formalism, according to Eq. 2.6:

$$I_{\text{cold}} = \frac{2e}{h} \int dE \mathscr{T}\left(E, V_{\text{B}}, \overline{T}\right) \left[f\left(E, \mu_{\text{L}}, \overline{T}\right) - f\left(E, \mu_{\text{R}}, \overline{T}\right) \right] \tag{2.12}$$

$$= \frac{2e}{h} \int dE \mathscr{T}\left(E, V_{\text{B}}, \overline{T}\right) \Delta f_{\text{cold}} \tag{2.13}$$

$$I_{\text{hot}} = \frac{2e}{h} \int dE \mathscr{T}\left(E, V_{\text{B}}, \overline{T} + \Delta\overline{T}\right) \left[f\left(E, \mu_{\text{L}}, \overline{T} + \Delta\overline{T} - \tfrac{\Delta T}{2}\right) \right. \tag{2.14}$$

$$\left. - f\left(E, \mu_{\text{R}}, \overline{T} + \Delta\overline{T} + \tfrac{\Delta T}{2}\right) \right]$$

$$= \frac{2e}{h} \int dE \mathscr{T}\left(E, V_{\text{B}}, \overline{T} + \Delta\overline{T}\right) \Delta f_{\text{hot}} \tag{2.15}$$

These equations reveal that the current trough the hot MTJ differs from the current through the cold MTJ. This difference has two origins. On the one hand the occupation functions $f\left(E, \mu, T\right)$ change when the heating is turned on, on the other hand the transmission is modified between heating on/off, due to its temperature dependence. For the correct quantitative calculation of the currents it is important to include the bias voltage and temperature dependence of the transmission into the Landauer-Büttiker formalism by employing $\mathscr{T}\left(E, V_{\text{B}}, T\right)$. However, for obtaining a much simpler expression that still allows a good qualitative description, the temperature dependence of the transmission is neglected in the following sections. This is in agreement with theoretical work performed by Heiliger *et al.* [19,47] who also use temperature independent transmissions for calculating the current through MTJs. However, this simplification does not result in temperature independent currents, because of the temperature dependent occupation functions $f\left(E, \mu, T\right)$ that have a major influence on the currents.

Now the detected current after the filter can be expressed as the difference between the current of the cold and the hot MTJ. Accordingly, the measured signal is given by:

$$\Delta I = I_{\text{hot}} - I_{\text{cold}} = \frac{2e}{h} \int dE \mathscr{T}\left(E, V_{\text{B}}\right) \left(\Delta f_{\text{hot}} - \Delta f_{\text{cold}}\right) \tag{2.16}$$

with the energy and bias voltage dependent transmission $\mathscr{T}\left(E, V_{\text{B}}\right)$.

This expression suggests that a signal is only generated, if the Δf are different for the hot and the cold MTJ. However, it also reveals that any difference between the Δf leads to a contribution to the signal ΔI. This is not restricted to the generation of a temperature gradient, but also an increase of the base temperature $\overline{T} + \Delta\overline{T}$ contributes to ΔI. Of course, this equation also points out that a signal is not detected, if there is no modulated heating applied to the MTJ. In that case Δf_{hot} and Δf_{cold} are the same and ΔI is zero.

Investigating the Seebeck and non-Seebeck contributions

The difference $\Delta f_{\mathrm{hot}} - \Delta f_{\mathrm{cold}}$ is caused by different effects. For a more detailed understanding of the impact of the various contributions to this difference, three cases are investigated. In the first case, it is assumed that only a temperature gradient ΔT is generated and the base temperature remains constant $\Delta\overline{T} = 0$. In the second, no temperature gradient is generated, $\Delta T = 0$, but the base temperature is elevated by $\Delta\overline{T}$ during the heating of the MTJ. In the third, both effects occur, the base temperature is enhanced and a gradient is generated across the barrier.

Fig. 2.9 displays the Fermi occupation of the electrodes for these three cases as a function of the energy for a bias voltage of 0.5 V. The bias voltage causes a shift of the chemical potentials of the individual electrodes with respect to the zero bias position of the chemical potential μ_0. The chemical potential of the right electrode μ_{R} is shifted to 0.25 eV and the chemical potential of the left electrode μ_{L} is moved to -0.25 eV. For simplicity, zero temperature is assumed when the heating is switched off, resulting in a step-like occupation function for the cold MTJ.

In the first scenario (Fig. 2.9a), only a temperature gradient is created between the two electrodes. Accordingly, the occupation of the right heated electrode broadens, but the occupation of the left cold electrodes remains unchanged. In the second scenario (Fig. 2.9b), only the base temperature is elevated, causing a similar broadening of the occupation functions in the left and right electrodes. In the third scenario (Fig. 2.9c) both effects occur. Hence, both occupation functions experience a broadening. However, the

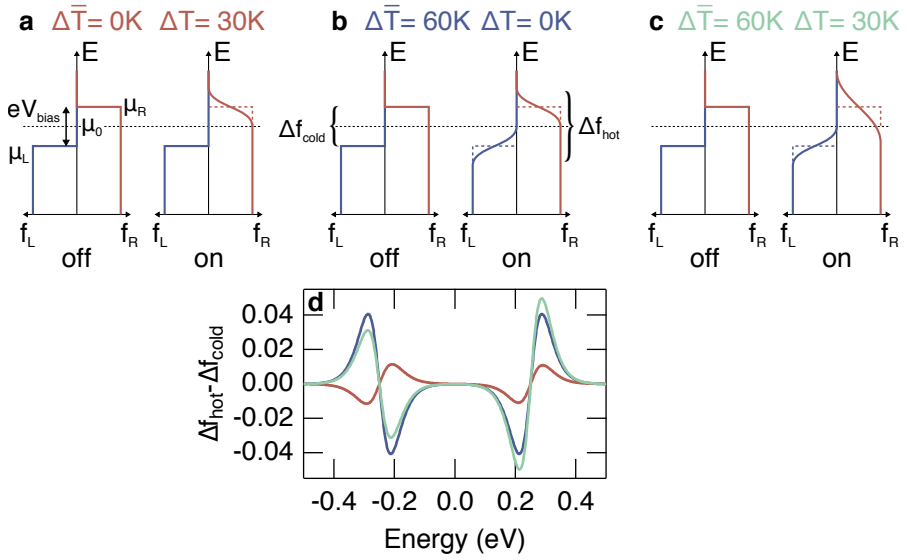

Figure 2.9. Occupation functions for the three different scenarios: a Only temperature gradient. **b** Only increase of mean temperature. **c** Both effects occur simultaneously. **d** Resulting contribution $\Delta f_{\mathrm{hot}} - \Delta f_{\mathrm{cold}}$ to the current difference ΔI between heating on (hot MTJ) and off (cold MTJ) in Eq. 2.16.

right more strongly heated electrode has a wider occupation function than the left cooler electrode.

The different altering of the Fermi occupation in the heated MTJ for the three scenarios yields different contributions to $\Delta f_{\mathrm{hot}} - \Delta f_{\mathrm{cold}}$. Fig. 2.9d displays the resulting $\Delta f_{\mathrm{hot}} - \Delta f_{\mathrm{cold}}$ in dependence on the energy. The largest changes for all scenarios occurs close to the energies of the shifted chemical potentials μ_{L} and μ_{R} of the electrodes at $\pm 0.25\,\mathrm{eV}$. This is not surprising, as it has been seen in Figs. 2.9a-c that the broadening of the occupation functions of the electrodes only affects an interval of a few meV around μ_{L} and μ_{R}. Hence, these are the energies for which different occupations of the hot and the cold electrodes are expected. Furthermore, the data reveal that for different scenarios the contributions possess different symmetries with respect to zero energy. If only the base temperature changes by $\Delta\overline{T}$,

the contribution to $\Delta f_{\text{hot}} - \Delta f_{\text{cold}}$ is symmetric with respect to zero energy. This is due to the equal broadening of the occupation in both electrodes. Accordingly, Δf_{hot} is symmetrically broadened with respect to μ_0, which is chosen to be at zero energy.

If instead only a temperature gradient ΔT generates a difference $\Delta f_{\text{hot}} - \Delta f_{\text{cold}}$, the obtained contribution is asymmetric with respect to zero energy. This asymmetry is generated by the asymmetric broadening of the Fermi occupations with respect to μ_0. In other words, Δf_{hot} is more strongly broadened at the energy μ_R, corresponding to the right heated electrode. The point symmetry observed in Fig. 2.9d is generated because the temperature difference ΔT is defined symmetrically between the left and the right electrode with respect to the mean temperature $\overline{T}$, that is $T_{\text{L}} = \overline{T} - \frac{\Delta T}{2}$ and $T_{\text{R}} = \overline{T} + \frac{\Delta T}{2}$.

Introducing the transmission of the MTJ

So far the obtained results are independent on the electronic structure of the observed MTJ. The information on the electron transport across the barrier is included into the Landauer model through the transmission $\mathscr{T}(E)$. The expression for the obtained signal ΔI (Eq. 2.16), only takes the previously discussed $\Delta f_{\text{hot}} - \Delta f_{\text{cold}}$ and the transmission as parameters. Hence, also the contributions to the detected signal ΔI for the three aforementioned scenarios can be studied by introducing the transmission.

To do so, the transmission for an MgO barrier between two Co-Fe electrodes is modeled. Fig. 2.10a displays such a model transmission in accordance to results of self-consistent *ab initio* calculations based on density functional theory applying a screened KKR (Korringa-Kohn-Rostoker) Green's function method. The effectiveness of this method for the description of experimentally investigated systems has been proven by, e.g., Papanikolaou *et al.*[53], Zeller *et al.*[54] and Heiliger *et al.*[47]. For a Co-Fe/MgO/Co-Fe system the transmission resembles the curve in Fig. 2.10a. With this transmission, the contributions to the signal ΔI for the three heating scenarios (Figs. 2.10b,c) are computed. The calculations performed in this thesis neglect the bias voltage dependence of the transmission. There are two reasons for this. Firstly, it is numerically demanding and time consuming to compute

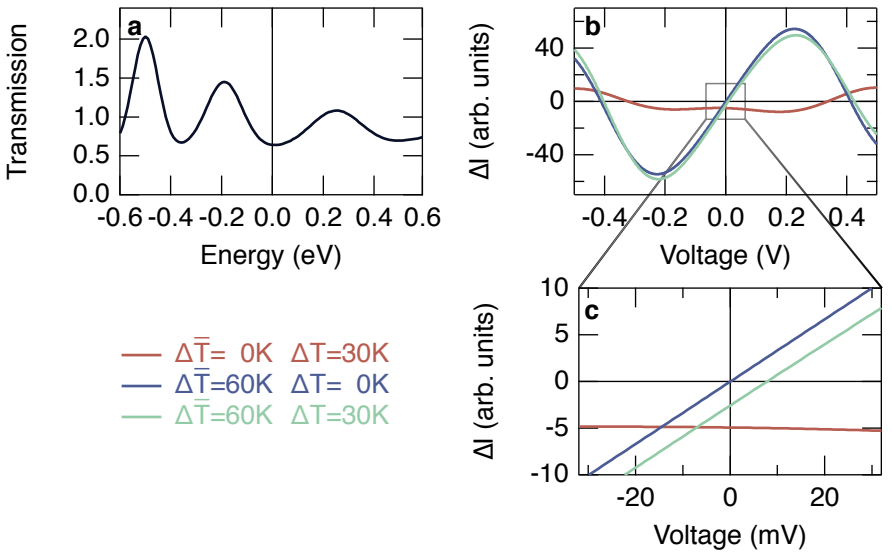

Figure 2.10. Contributions to ΔI for a Co-Fe based MTJ with an MgO barrier: **a** Energy dependent transmission of the MTJ. **b** Obtained signal ΔI for the three different scenarios. **c** Zoomed in cutout of b for bias voltages between ±30 mV.

the bias dependence of the transmission. Secondly, and more importantly, experimentally the bias dependence of the Seebeck effect (cf. Sec. 4.3) is only observe for small bias voltages (±30 mV), for which only small changes of the transmission due to an applied bias voltage are expected[47]. Neglecting the voltage dependence of the transmission intrinsically assumes that the tunnel junction is symmetric, leading to $I(V) = -I(-V)$, i.e., a perfectly antisymmetric IV curve. Thus, it is important to consider this when comparing the calculations presented here with the experimental results (Sec. 4.3). Particularly, it is crucial to check whether the investigated MTJ is symmetric, e.g., by measuring the IV characteristics or the differential conductance in dependence of the bias voltage. With these simplifications it is possible to investigate the contributions to the obtained current signals ΔI without large computational effort.

Although, the MTJ exhibits a transmission rich in features, the pure Seebeck type contribution ($\Delta\overline{T} = 0$, $\Delta T \neq 0$) to ΔI is rather flat for low bias voltages (red curves in Fig. 2.10). This can be nicely seen in Fig. 2.10c, which displays the interval of bias voltages between $\pm 30\,\mathrm{mV}$ in more detail. But even for larger bias voltages ΔI is still nearly perfectly symmetric with respect to zero bias voltage. Nevertheless, a zero-crossing of the signal is found at $\approx \pm 0.3\,\mathrm{V}$. A zero crossing is a remarkable feature, pointing out that applying a bias voltage to an MTJ and determining the Seebeck contribution is a revealing experiment.

For the scenario with elevated base temperature and without a temperature gradient ($\Delta\overline{T} \neq 0$, $\Delta T = 0$), a point symmetric ΔI is found with respect to the origin of zero bias voltage and zero ΔI (blue curves in Fig. 2.10). The curve for ΔI possesses a maximum at $0.22\,\mathrm{V}$ and a minimum at $-0.22\,\mathrm{V}$. In the region of small bias voltages the signal nearly resembles a linear curve with a positive slope.

If both effects occur ($\Delta\overline{T} \neq 0$, $\Delta T \neq 0$), the antisymmetric curve of the second scenario is shifted downwards by the symmetric contribution of the temperature gradient (green curves in Fig. 2.10). This can be seen best in Fig. 2.10c.

To properly understand how the different contributions and symmetries of ΔI are related to the shape of the transmission, the transmission of the real MTJ (Fig. 2.10a) is reduced to its simplified main features. For each feature, the signal ΔI is evaluated separately and, hence, its portion in the real signal can be deduced (Fig. 2.11).

The transmission of the first model contains a single Gaussian peak at $-0.25\,\mathrm{eV}$ that only slightly extends to positive energies (Fig. 2.11a). The voltage dependent contributions to the signal ΔI are similar to the results obtained for the transmission of the "real" MTJ (Fig. 2.10). They exhibit the same symmetries, as well as a maximum and minimum, when a change in base temperature is assumed. However, the Seebeck like contribution ($\Delta\overline{T} = 0$, $\Delta T \neq 0$) does not cross the x-axis.

For the transmission of the second model the Gaussian peak is shifted to $0.25\,\mathrm{eV}$ (Fig. 2.11b). The calculated ΔI for the scenario of an elevated base temperature, but without temperature gradient ($\Delta\overline{T} \neq 0$, $\Delta T = 0$), reveal the exact same results as for the first model transmission with the peak at

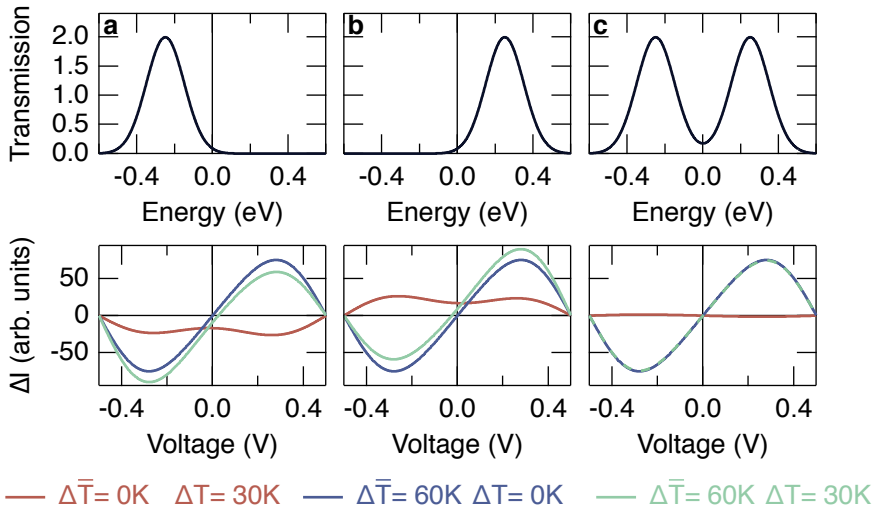

Figure 2.11. Contributions to ΔI for different model transmissions: **a** A peak in the transmission at negative energy. **b** A peak at positive energy. **c** A symmetric transmission with a pseudo-gap.

negative energies. The contribution of the temperature gradient ($\Delta\overline{T} = 0$, $\Delta T \neq 0$), instead, switches from negative to positive values. Thus, the data for ΔI when both effects are present ($\Delta\overline{T} \neq 0$, $\Delta T \neq 0$) is shifted to positive values, instead of negative values, as in the first case.

The transmission of the third model consists of two Gaussian peaks at $\pm 0.25\,\mathrm{eV}$ (Fig. 2.11c). Because the peaks do not decay to zero at zero energy, a finite transmission at zero energy is obtained. In other words, a pseudo-gap with a symmetric transmission is found. If only the base temperature is elevated during heating ($\Delta\overline{T} \neq 0$, $\Delta T = 0$), the resulting ΔI are still the same as for the first two cases. The Seebeck like contribution ($\Delta\overline{T} = 0$, $\Delta T \neq 0$), nonetheless, exhibits a completely different behavior; it is much smaller for all applied bias voltages, compared to the previous cases. Furthermore, it is antisymmetric with respect to zero volt.

After these evaluations the question arises whether there is a simple rule for the connection of the shape of the transmission to the behavior

of the signal ΔI. For the pure non-Seebeck contribution (rise of the base temperature $\Delta\overline{T}$ only) it is impossible to link the shapes of the transmission to ΔI, because the results are the same for all modeled transmissions. On the contrary, the Seebeck like contribution (only ΔT) shows a relationship between the symmetry of the transmission and the size and sign of the obtained signal. For an asymmetric transmission, ΔI is symmetric. The sign of ΔI is determined by the position of the symmetric mean of the transmission. For a symmetric transmission, a much smaller contribution is received and ΔI becomes antisymmetric, instead. These relations can also be extracted from the signal, when not only a temperature gradient is generated, but also the base temperature is elevated.

The experimental determination of a Seebeck effect under an applied bias voltage

From an experimentalist's point of view, the description of the response of the MTJ in terms of the current signal ΔI, that is derived from the nonlinearized Landauer-Büttiker formalism, is highly unsatisfactory. A major drawback is the impossibility of defining the transport coefficients, in particular the Seebeck coefficient. Hence, directly determined Seebeck coefficients from a conventional Seebeck experiment without applied bias voltage cannot be compared to the Seebeck contribution that is generated in an MTJ that experiences a temperature difference and a bias voltage. However, as described in Sec. 2.3.4, in the case of small temperature differences ΔT and small bias voltages V the linearized Landauer-Büttiker formalism represents a first order approximation. Hence, in the linear regime it is possible to derive a bias-Seebeck coefficient S^{bias} from the ΔI signal by employing the equation of the linearized current (Eq. 2.7). It has to be kept in mind, that the bias-Seebeck coefficient S^{bias} can only be observed when a bias voltage and a temperature difference are simultaneously applied to the MTJ.

The description of the currents based on the linearized Landauer-Büttiker model allows to insert experimentally determined transport coefficients, e.g., the conductance, into the equation. Accordingly, a determination of the Seebeck contribution to the total current becomes feasible in the regime of small applied bias voltages. In the following paragraphs this knowledge is

used to relate the current signal to the bias-Seebeck coefficient S^{bias}. The presented derivation has been published in Ref. 18, that directly evolved from the work performed for this thesis. It lays the foundation for the first investigation of the voltage dependence of the TMS effect.

In the linearized Landauer-Büttiker formalism the DC voltage driven contribution to the total current is proportional to the conductance (Eq. 2.8). Experimentally, this is obtained from current measurements without an applied temperature gradient, i.e., when the heating is switched off.

$$I_{\text{off}} = G \cdot V \tag{2.17}$$

These data are usually obtained from TMR measurements, as described in Sec. 3.1.3.

When the heating is switched on the Seebeck current $G \cdot S^{\text{bias}} \Delta T$ is measured additionally. This current is proportional to the conductance G and the Seebeck voltage $S^{\text{bias}} \Delta T$, yielding

$$I_{\text{on}} = \underbrace{G \cdot V}_{I_{\text{off}}} + G \cdot S^{\text{bias}} \Delta T. \tag{2.18}$$

If the resistance R of the MTJ and the total current are known, it is possible to determine the Seebeck contribution as

$$S^{\text{bias}} \Delta T = \frac{I_{\text{on}} - I_{\text{off}}}{G} = \Delta I \cdot R, \tag{2.19}$$

where ΔI corresponds to the output of the narrow band-pass filter, i.e., a lock-in amplifier (Sec. 3.1.7).

This approach, however, neglects the temperature dependence of the resistance of the MTJ. The elevated base temperature causes a decrease of the resistance of the MTJ that is expressed as

$$\begin{aligned} \Delta R &= R\left(T_{\text{off}}\right) - R\left(T_{\text{on}}\right), \text{ with } R_{\text{on}} < R_{\text{off}} = R \\ &\Rightarrow \quad R_{\text{on}} = R - \Delta R \end{aligned} \tag{2.20}$$

With the resistance R determined when the heating is switched off, for example in a TMR measurement.

As the resistance of the MTJ changes under heating on/off, the current generated by the bias voltage is different for the heated and not-heated MTJ. Conclusively, the current difference between on/off is expressed as:

$$\Delta I = I_{\mathrm{on}} - I_{\mathrm{off}} = \underbrace{\frac{S^{\mathrm{bias}}\Delta T}{R-\Delta R} + \frac{1}{R-\Delta R}V}_{I_{\mathrm{on}}} - \underbrace{\frac{1}{R}V}_{I_{\mathrm{off}}} \tag{2.21}$$

$$= \frac{1}{R-\Delta R}\left(S^{\mathrm{bias}}\Delta T + \frac{\Delta R}{R}V\right) \tag{2.22}$$

ΔI consists of two parts depending on the two gradients across the barrier; a current generated by ΔT that is proportional to the bias-Seebeck coefficient S^{bias}, and a voltage-induced current that is proportional to the resistance ratio $\Delta R/R$. In an MTJ, all of these three quantities, S^{bias}, R and ΔR, change when the magnetic state of the MTJ is reversed from p to ap[3,4]. In a bias voltage region where the contributions generated by ΔT and V are comparable, this relationship allows to deliberately tune the current ΔI by the two parameters ΔT and V. Eq. 2.22 reveals two interesting experimental options to exploit the two independent driving forces of the current. Both options are developed in this thesis.

Bias enhanced tunnel magneto-Seebeck effect

In the first variation, an external fixed voltage is applied to the MTJ in the p state that cancels out the Seebeck voltage $S_{\mathrm{p}}^{\mathrm{bias}}\Delta T$ to achieve $\Delta I_{\mathrm{p}} = 0$. Now, when the magnetization is reversed to the ap state, V remains constant, but the resistances change to R_{ap} and ΔR_{ap}, and the Seebeck voltage changes its magnitude to $S_{\mathrm{ap}}^{\mathrm{bias}}\Delta T$ because of the TMR and TMS effects. Thus, the measured ΔI_{ap} will differ from zero. Although, a change in R and ΔR could compensate the change in S^{bias}, this exact cancellation is extremely unlikely for Co-Fe-B/MgO/Co-Fe-B MTJs (the effect ratios for these effects differ by at least one order of magnitude, see Ref. 4). Hence, an on/off switching of the measured current upon magnetization reversal is received. To quantify this effect, the bias-enhanced TMS (bTMS) ratio is defined:

$$\mathrm{bTMS} = \frac{\Delta I_{\mathrm{ap}} - \Delta I_{\mathrm{p}}}{\min\left(\left|\Delta I_{\mathrm{p}}\right|, \left|\Delta I_{\mathrm{ap}}\right|\right)}. \tag{2.23}$$

Bias dependence of the magneto-Seebeck effect

In the second experimental variation, it is estimated how the bias-Seebeck coefficients $S_{\mathrm{p,ap}}^{\mathrm{bias}}(V)$ change with the applied bias voltage. This experiment provides first insights into the influence of the band structure of the electrodes on the TMS. This is made possible by carefully tuning the relative position of the chemical potentials using the bias voltage V as described in detail in Sec. 2.4.1. To suppress non-linearities with respect to V, a small voltage interval that exhibits a linear IV characteristic is chosen, implying $R(V) = R =$ const. and $\Delta R(V) = \Delta R =$ const. Furthermore, contributions from artifacts caused by, e.g., Peltier and Thomson effects are neglected based on estimates using the typical Seebeck coefficients of Co-Fe-B based MTJs[4,17,19,20] (cf. Appendix C.2). Therefore, a linear model is employed to determine the contribution of $(\Delta R/R)V$ to ΔI. Using the information from this model, the non-Seebeck contribution is subtracted from the measured ΔI, and $S^{\mathrm{bias}}\Delta T$ is determined.

Despite the relatively complicated derivation of the signal ΔI from the generated currents in the MTJ, the final result is rather fundamental. A direct connection of the symmetry of the transmission to the shape of the signal ΔI is found. For small temperature differences and voltages it is even possible to regain the Seebeck contribution to the signal. Accordingly, applying a bias voltage to an MTJ and performing a Seebeck current measurement is a powerful approach to gain a deeper insight into the shape of the transmission and to grasp more information on its asymmetry. Since material combinations with a highly asymmetric transmission are desirable for high TMS effects, the gained information is useful to systematically modify the transmission to receive high TMS effects even without applied bias voltage. In the next section it is discussed which materials are suitable for this purpose.

2.4.2. Finding the optimum material

As it has been demonstrated before (Secs. 2.3.5 and 2.3.6), the DOS has a great impact on the Seebeck effect in MTJs. Different DOSs can be implemented into MTJs by replacing the electrode materials. A first evidence for the sensitivity of the TMS effect to a change in the DOS was already

revealed by the first TMS experiments by Walter *et al.* [4] and Liebing *et al.* [5] that yield TMS ratios of −8.8 % and 30 %, respectively. Both used Co-Fe-B electrodes and MgO barriers, but the composition of the Co-Fe-B was strikingly different; Walter *et al.* used $Co_{20}Fe_{60}B_{20}$ (from energy dispersive X-ray analysis Co:Fe 0.32:0.68), whereas Liebing *et al.* used $Co_{60}Fe_{20}B_{20}$ (Co:Fe 0.75:0.25). This change in the composition results in a drastic change of the Seebeck coefficients of the MTJs, although it barely affects the TMR ratios.

A more systematic analysis of different Co-Fe compositions on the TMS effect has been undertaken by Heiliger *et al.* [19], who used *ab initio* alloy theory to calculate the Seebeck coefficients of the MTJs. Their findings exhibit a strong influence of the composition, and, hence, the DOS on the TMS effect. According to their predictions, the variation of the composition can even cause a sign change of the Seebeck coefficients. Furthermore, they find Seebeck coefficients with opposing signs when the MTJ is switched from p to ap. This yields corresponding TMS ratios in a range of ±800 % for the calculated compositions. If theses relatively small modifications of the DOS due to stoichiometry have such a great impact on the TMS effect, replacing the Co-Fe based electrode material with a different material class potentially has an even stronger influence. Furthermore, producing alloys of Fe_xCo_{x-1} is not always feasible. Hence, it is much more promising to investigate half-metallic Heusler compounds for achieving the desired improvements, as it is presented in this thesis.

An introduction to half-metallic Heusler compounds

Heusler compounds were discovered by Friedrich Heusler in 1903 [55,56]. He observed a ferromagnetic behavior of the compound Cu_2MnAl, although it only contains atoms that form non-ferromagnetic solids. This property is found for several materials with the structure X_2YZ, where X and Y are transition metals and Z is a main group element. The crystal structure was unveiled by Bradley and Rodgers [57] in 1934. The structure is described by an fcc lattice with a four-atom basis [58]. The resulting four fcc sub-lattices are denoted as A, B, C and D, which are occupied in the order X-Y-X-Z. The origin of the sub-lattices are shifted by the vectors A : $(1/4, 1/4, 1/4)$, B : $(1/2, 1/2, 1/2)$, C : $(3/4, 3/4, 3/4)$, and D : $(0, 0, 0)$ in Wyckoff coordinates. The resulting

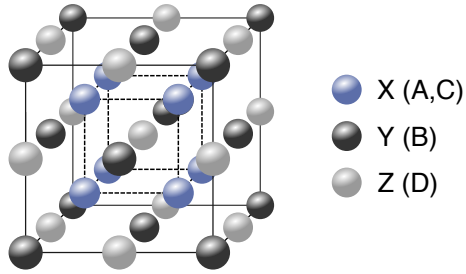

Figure 2.12. Crystal structure of an $L2_1$ Full-Heusler compound X_2YZ: The crystal is described as an fcc lattice with a four-atom basis. The sites A, B, C and D are occupied by the atoms X, Y, X and Z. The origins of the sub-lattices are shifted against each other by 1/4 along the space diagonal and are located at: A : $(1/4, 1/4, 1/4)$, B : $(1/2, 1/2, 1/2)$, C : $(3/4, 3/4, 3/4)$, and D : $(0, 0, 0)$.

structure is sketched in Fig. 2.12 and is referred to as the $L2_1$ structure of X_2YZ full-Heusler compounds.

Half-metallicity is predicted for a variety of Heusler-Compounds [59]. This property is defined by different electronic properties for the spin-up and spin-down charge carriers. One sort of spin exhibits a metallic DOS, whereas the DOS for the opposite spin species possesses a gap around the chemical potential μ.

For some compositions of the form X_2YZ the occupations of the sites B and D by the atoms Y and Z are equal in energy. This degeneracy leads to a random occupation of the B and D sites by atoms Y and Z. Conclusively, the ordering is reduced to the B2 type. The different occupations of the lattice sites in the $L2_1$ and the B2 ordering influence the electronic structure of the materials. For example, the disorder in the B2 structure can cause the gap in the DOS of half-metallic Heusler compounds, to narrow to a pseudo-gap, with a finite number of states present at the chemical potential.

Large charge Seebeck coefficients in Heusler compounds

But why are half-metallic Heusler compounds so fitting for generating high Seebeck coefficients, and high TMS effect ratios in MTJs? This question is

Table 2.1. Charge Seebeck coefficients of Heusler compounds: Magnetic moments, Curie temperatures, and absolute Seebeck coefficients of Co_2YZ compounds (data taken from Balke *et al.* [60]).

Compound	T_c (K)	M_{sat} (5 K) (μ_B)	S (300 K) ($\mu V K^{-1}$)
Co_2TiAl	128	0.75	-55
Co_2TiSi	380	1.96	-27
Co_2TiGe	380	1.94	-22
Co_2TiSn	355	1.97	-34
Co_2MnAl	693	3.96	-4
Co_2MnSi	985	4.97	-7
Co_2MnGe	905	4.98	-15
Co_2MnSn	829	5.03	-33
Co_2FeSi	1100	5.97	-12

answered in this thesis as presented in the next sections. For understanding the ingredients needed for high Seebeck coefficients it is useful to take one step back and remind oneself of the origin of different charge Seebeck coefficients in different materials. As illustrated in Sec. 2.2, semiconductors turned out to have much higher Seebeck coefficients than metals. This difference is attributed to their different DOSs around the chemical potentials. The gap in the DOS of the semiconductor suppresses the transport of either holes or electrons, resulting in a high net diffusion current and, thus, in a large Seebeck effect.

In half-metallic Heusler compounds, a DOS with a gap around the chemical potential for one sort of spins is found, while the other species of spins occupies a metallic DOS. If the transport in such a material is described within the previously introduced two current model for each spin channel (see Sec. 2.3.1), it can be treated as a semiconductor-like transport for one spin orientation and a metal-like transport for the other spin direction. Consequently, a high Seebeck coefficient for the semiconductor-like DOS and a low Seebeck coefficient for the metal-like DOS is expected. Introducing these materials into MTJs allows a selection of these channels by spin-dependent tunneling [8].

The first impact of the gap on the Seebeck effect is revealed when comparing charge Seebeck coefficients of bulk Heusler compounds with free-electron-like metals. At room temperature, $T = 300\,\mathrm{K}$, Co based Heusler compounds possess Seebeck coefficients exceeding $-50\,\mu\mathrm{V\,K^{-1}}$ (see Tab. 2.1), whereas Al only reaches $-1.8\,\mu\mathrm{V\,K^{-1}}$ [61]. For commonly used ferromagnets the Seebeck coefficient is even smaller, for example $0.3\,\mu\mathrm{V\,K^{-1}}$ in pure Fe [62].

The benefits of a half-metallic DOS

The previous comparison of Seebeck coefficients of bulk materials gives a first impression on the benefits of using half-metallic Heusler compounds in MTJs to realize high TMS effects. For a deeper understanding of the mechanisms in MTJs, the model proposed in Sec. 2.3.1 is a helpful tool. It suggests, that a qualitative estimate of the size of the Seebeck effect in MTJs is possible by only considering the DOSs (see Sec. 2.3.6). The spin-dependence of the Seebeck coefficients is taken into account by individually considering the contributions of each spin species to the total tunneling current (two current model). Therefore, in the next paragraphs the knowledge gained in Sec. 2.3.1 is transferred from normal ferromagnetic DOSs to half-metallic DOSs.

Fig. 2.13 depictively compares the thermoelectric transport in an MTJ consisting of two normal ferromagnets (Fig. 2.13a,b) with an MTJ containing one ferromagnet and one half-metal (Fig. 2.13c,d). The contributions of the indicated tunneling currents in Fig. 2.13a,b for a normal ferromagnet (FM1)/barrier/normal ferromagnet (FM2) MTJ have already been discussed in Sec. 2.3.1. Here, only the two most important results are recalled; the currents above and below the chemical potential almost have the same size and, thus, cancel out. As there is only a small net diffusion current, the resulting Seebeck effect is small. This picture does not change significantly when the MTJ is switched from ap to p. However, a small increase of the diffusion currents is observed, since there are more states contributing to the transport in each spin channel. Since the increase is small, only a small TMS effect is generated.

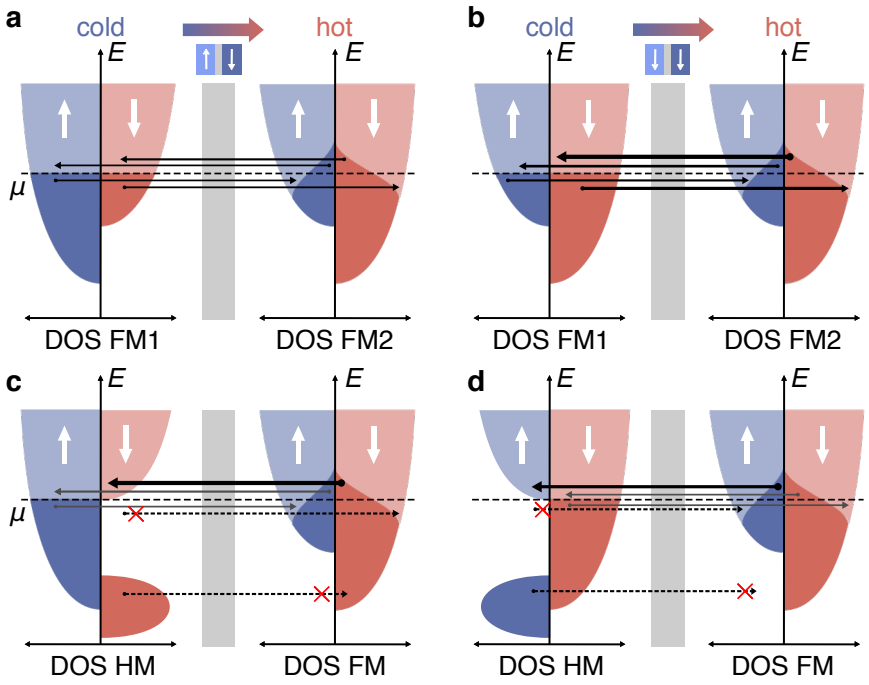

Figure 2.13. Comparison of normal ferromagnet and half-metallic electrodes: Ferromagnet/insulator/ferromagnet MTJ **a** in the ap and **b** in the p state. In an MTJ consisting of two free-electron-like ferromagnetic electrodes diffusion currents above and below μ cancel out. **c,d** Half-metal/Insulator/ferromagnet MTJ, in the ap and the p state, respectively. By replacing one electrode by a half-metal some of these currents are suppressed due to the gap. Thus, the net current is enhanced.

For the MTJ consisting of a half-metal (HM)/barrier/normal ferromagnet (FM) a completely different result is obtained. In the ap state (Fig. 2.13c) the net current is dominated by the electrons traveling from the majority states of the ferromagnet into the minority states of the half-metal (red states) above the chemical potential μ. These electrons can only travel above μ, because below μ either initial or final states are unavailable. This lack of states below μ results in a vanishing diffusion current below μ from the cold into the hot ferromagnet. However, the large amount of states above μ leads to a substantial net diffusion current from the hot ferromagnet to the

cold half-metal. The enhanced net diffusion current results in an increased Seebeck voltage. For the electrons with momentum up (blue states) the transport remains unchanged, because these states still exhibit a metallic DOS.

When the MTJ is switched to the p state (Fig. 2.13d), the net current is still dominated by the transport of electrons above μ from the hot ferromagnet to the cold half-metal. Nonetheless, the current in the p state is decreased, since electrons with momentum up have to travel between the minority states of the ferromagnet and the minority states of the half-metal (blue states). The number of minority states in the normal metal is smaller than the number of majority states, that contributed to the transport in the ap state. In the p state the decreased availability of initial states in the hot normal ferromagnet causes a reduction of the diffusion current, although the amount of final states in the half-metal remains the same as in the ap state of the MTJ. Thus, the Seebeck voltage is smaller in the p state than in the ap state. For electrons with momentum down (red states) the transport remains the same as in Fig. 2.13b.

DOS of Heusler compounds Co_2FeSi and Co_2FeAl

For the following investigations in this thesis two different Heusler compounds are chosen; Co_2FeSi and Co_2FeAl. The TMS effect in MTJs that contain these materials should be predictable from the DOS. Therefore, the DOS is calculated by density functional theory (Fig. 2.14). For computing the DOSs of the Heusler compounds in $L2_1$ ordering the full-potential augumented plane-wave code elk[63] is used. The DOS in B2 ordering is obtained by the SPR-KKR code[64]. The fractional occupation of the Wyckoff-position 1b was realized by the coherent potential approximation. In both cases, the Perdew-Burke-Ernzerhof functional is applied for approximating the exchange correlation interaction.

At first sight, the DOSs of Co_2FeSi and Co_2FeAl in the $L2_1$ ordering (Figs. 2.14a,b) reveal similar features. For the minority DOSs a large number of states is found above the chemical potential adjacent to a gap-like feature for lower energies. Compared to the feature-rich minority DOSs, the majority DOSs of both compounds is relatively flat close to the chemical potential.

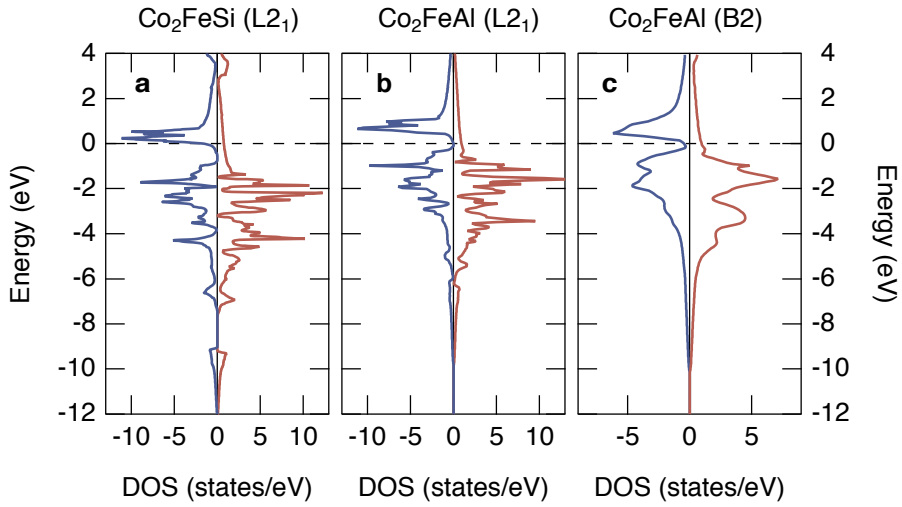

Figure 2.14. Density of states of Heusler compounds: **a** of Co_2FeSi and **b** Co_2FeAl in the L_21 structure, and **c** of Co_2FeAl in the less ordered B2 structure. Positive values of the DOS indicate majority (spin up) states, negative values indicate minority (spin down) states. The chemical potential is chosen to be at zero energy (Co_2FeSi data from Sterwerf[65]).

Consequently, the DOSs of both materials nicely fulfill the shape of the desired "optimum" DOS that is suggested in Fig. 2.13. Hence, they are most likely very suitable for obtaining high Seebeck voltages and high TMS effect ratios.

Looking more carefully, the different positions of the chemical potentials with respect to the gap are recognized. For the Co_2FeAl the chemical potential is placed at a centered position in the gap, whereas for the Co_2FeSi the chemical potential cuts through the lower edge of the characteristic peak of states in the minority DOS, causing the DOS of Co_2FeSi to be highly asymmetric with respect to the chemical potential.

However, this difference is only present, if the Co_2FeAl crystallizes in the $L2_1$ ordering. Co_2FeAl in the less ordered B2 structure does not posses such a pronounced gap in the minority DOS as Co_2FeAl in the $L2_1$ structure

(Fig. 2.14c). Since states remain in the gap, only a pseudo-gap is found in the B2-ordered Co_2FeAl. Furthermore, the width of the gap narrows, such that the chemical potential is nearly cutting through the bottom edge of the peak above the gap. Although, the formation of a pseudo-gap might be disadvantageous in terms of spin-polarization, the higher asymmetry of the DOS with respect to the chemical potential should increase the Seebeck effect in the Co_2FeAl based MTJs. In other words, the B2 ordered Co_2FeAl should resemble the properties of the $L2_1$ ordered Co_2FeSi concerning the thermoelectric transport in MTJs.

Since the ordering of the Heusler compounds has a significant influence on the size and even position of the gap in the minority DOS, its impact is discussed in more detail. The size, position, and how well the gap is pronounced are heavily debated in literature about *ab initio* calculations of the DOS of Heusler compound, e.g., by Meinert *et al.* [66]. For real samples it is even more complicated. Whether the gap in the minority DOS is a proper gap with zero states at a certain energy, or whether it is a pseudo-gap with a finite number of states, sensitively depends on the exact composition and crystallographic order of the compounds [67]. This does not only include the ordering of the compound in the $L2_1$ or B2 phase, but also the presence of impurity atoms, lattice vibrations, and many other deviations from the ideal Heusler structure [68]. However, in Sec. 2.2.2 it has been shown that the most important feature for a high Seebeck effect is a high asymmetry of the DOS in the vicinity of the chemical potential. This condition is fulfilled, even if a small amount of states exists in the gap. Furthermore, Czerner and Heiliger [69], Comtesse *et al.* [45], and Geisler and Kratzer [26] predict that the interface configuration between the Heusler compound and an adjacent material influences the thermoelectric properties in nanostructures much more than minor lattice imperfections. Although their results suggest a strong dependence of the thermoelectric properties on the exact lattice and interface structures, Geisler and Kratzer [26] suggest Heusler compounds to be ideal for high Seebeck and spin-dependent Seebeck coefficients. This, once more, underlines that Heusler compounds might be the perfect candidates for experimental observations of high TMS effects in MTJs.

Chapter 3

Methods & Materials

This chapter gives an introduction to the most important techniques that are necessary for the investigation of the TMS effect. The first section (Sec. 3.1) concentrates on the optical and electrical setups that are specifically designed and optimized for the observation of the TMS effect. The second section (Sec. 3.2) gives a profound description of the sample preparation. In particular, it focuses on the sputter deposition of the layer stacks and the patterning of the MTJs. Different designs are introduced and their advantages and disadvantages are discussed. The third section (Sec. 3.3) contains a brief explanation of the X-ray techniques that are employed for the characterization of the deposited layer stacks. The last section (Sec. 3.4) presents the most important parameters for obtaining the temperature in the MTJs from finite element simulations.

3.1. Tunnel magneto-Seebeck effect setup

In this section the experimental setup for the determination of the TMS effect via laser induced heating is explained. The basic parts of the optical setup, the electrical connection of the nano-patterned sample to the measurement electronics, as well as the electronic components are discussed. Furthermore, parasitic effects that can be generated by the electronics are briefly examined.

This information has partly been published in Ref. 17, which originated directly from this work.

In the last part, a method to perform TMS experiments under an additionally applied bias voltage is introduced. This method is based on the knowledge gained on the transport through MTJs that experience a voltage and temperature drop across the barrier (Sec. 2.4.1).

3.1.1. Optical setup

The optical setup for inducing a temperature gradient in an MTJ through laser heating is depicted in Fig. 3.1. A diode laser (Toptica iBeam smart 640-S) emits laser light with a central wavelength of $\lambda = 637\,\mathrm{nm}$ in a tunable power range of 1 mW to 150 mW. The laser diode is modulated between on/off with a waveform generator (Agilent 3352A) that allows the continuous adjustment of the modulation frequency from a few Hz up to several kHz. This is particularly useful, if the impedances of the samples change.

For achieving a well defined beam spot on the sample, the beam diameter is first expanded by two lenses and then focused down by an infinity corrected microscopy objective (Mitutoyo M Plan Apo 10x) with a primary magnification of 10×, a working distance of 33.5 mm, and a numerical aperture of 0.28. With this setup a beam diameter of down to $\approx 6\,\mu\mathrm{m}$ can be obtained. To enable a homogeneous heating of MTJs with a larger diameter, the beam size is increased by moving the sample out of focus.

The reflected light is collected by an ultrafast photo diode (EOT ET-2030, rise time of $< 300\,\mathrm{ps}$), enabling the measurement of the beam width by the knife edge method [70,71]. Therefore, the beam is moved over a well defined edge on the sample, e.g., the edge of a gold bond pad. As the reflection of the gold surface and the adjacent insulator are different, the diode voltage changes with the spot position. The resulting curve is proportional to the change in power of the reflected light and, since a sharp edge is probed, resembles the lateral beam profile. The change in the diode signal is described by

$$P_{\mathrm{measured}}(x) = \frac{P_{\mathrm{max}}}{2}\left[1 - \mathrm{erf}\left(\frac{\sqrt{2}\,(x - x_0)}{w_0}\right)\right] \tag{3.1}$$

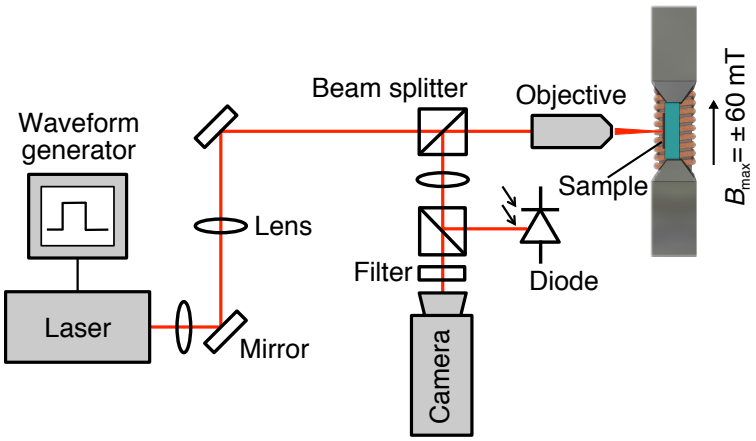

Figure 3.1. Optical setup: For heating, a modulated laser ($\lambda = 637\,\text{nm}$, $P_{max} = 150\,\text{mW}$) is focused onto the MTJ. The position is controlled via a confocal microscope arrangement equipped with a camera.

With the maximum obtained diode signal P_{max}, the position of the beam on the sample x, the position of the edge on the sample x_0, and the radius of the beam waist w_0, that is the $1/e^2$ radius in the lateral intensity distribution of the beam profile. The shape of the measured power $P_{measured}$ (Eq. 3.1) is largely determined by the error function

$$\text{erf}(x) = \frac{2}{\sqrt{\pi}} \int_0^x e^{-t^2} dt \tag{3.2}$$

Exemplarily, Fig. 3.2 displays the obtained values and fits for the sample position adjusted to a narrow and a wide beam width. For all measurements the beam is set to a size larger than the MTJ diameter and the beam size is controlled via the knife edge method.

Furthermore, the photo diode monitors the rise and fall time of the modulated laser signal. This is an important information for investigating the temporal evolution of the Seebeck voltage.

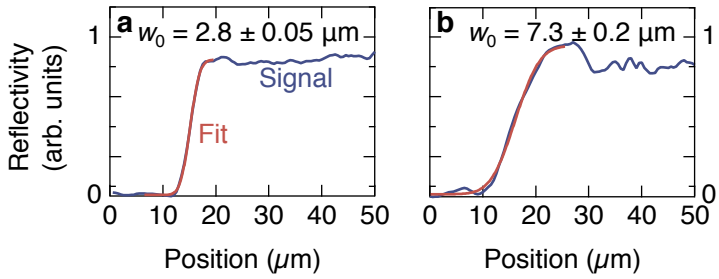

Figure 3.2. Beam waist: Reflectivity for knife edge measurements and corresponding fits of the beam waist w_0. **a** For the sample at the focal position of the beam, i.e., the narrowest beam waist achievable. **b** For the sample moved out of focus.

3.1.2. Connecting the sample to the measurement electronics

The MTJ sample is glued into an IC bond socket with 24 pins, from which 12 pins are used in the experimental setup. The individual MTJs and the bottom contact are connected to these pins by ball-wedge or wedge-wedge bonding with a 25 µm gold wire. Fig. 3.3a displays a light microscope image of an electrically connected sample with a wedge bond on top of the gold contact pad. The bright dot adjacent to the gold contact pad is the MTJ that is still optically accessible by the laser beam, since it is not covered by the wire. In Fig. 3.3b a larger section of the sample is visible. The first pin on the left is connected to the bottom electrode, which is the same for all MTJs. The other wires are connected to the top contacts of different individual MTJs.

For all measurement modes performed with the optical setup, the sample is clamped into a receptacle for the IC bond socket between the pole shoes of an electromagnet that provides a maximum magnetic flux density of ±60 mT to the sample. The receptacle allows electrical access to the sample for connecting the measurement electronics. From the receptacle onward, the signal of each pin is transferred through a coaxial cable ending in a BNC connector. This arrangement allows the individual connection of each MTJ that is equipped with a bond wire, and the bottom contact to the measurement electronics. The exact measurement equipment is determined by the desired measurement to be performed. Each of them will be explained

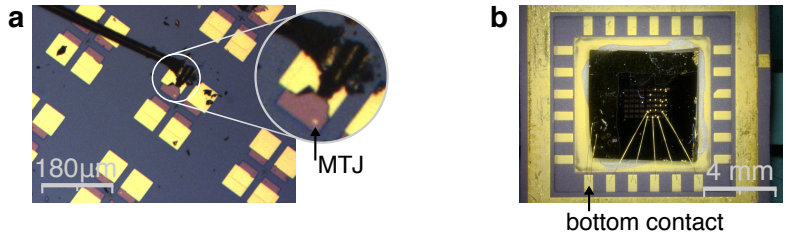

Figure 3.3. Sample in IC bond socket: Microscopy images of, **a** a wedge bond placed on top of a gold contact pad, connected to a single MTJ. The MTJ is still optically accessible, and **b** the sample with the bottom contact (left pin) and several MTJs connected to the socket.

in the course of the next sections. To avoid a dielectric breakdown of the tunnel barrier in the MTJs, the bottom and the top contacts are shorted by a switch, while the measurement electronics connected to the sample are exchanged, i.e., the measurement mode is changed.

3.1.3. Tunnel magnetoresistance in the optical setup

The magnetoresistance of the investigated MTJs is determined inside the optical setup before each TMS experiment. Therefore, a sourcemeter in constant voltage mode (Keithley 2400) is connected to the bottom and top electrodes of the MTJs. When not explicitly indicated, all TMR measurements within this work are performed with a constant bias voltage of 10 mV and the bottom electrode of the MTJ connected to ground. From the generated current and the applied voltage the resistance is determined. The magnetic field provided by the electromagnet is sufficient to switch the MTJs between the p and the ap states. For controlling the switching behavior of the MTJs, the magnetic field is swept over an interval at least larger than the coercive field of one electrode (minor loop), or preferable larger than the coercive field of both ferromagnets (major loop). From the obtained resistance versus field curves, the TMR ratio of the MTJs is determined without removing them from the magneto-Seebeck setup.

Furthermore, in this configuration so called IV characteristics of the MTJs are obtained. These curves are recorded by varying the applied voltages in an interval of several 100 mV around zero bias. The corresponding current (I) is measured and plottet versus the voltage (V). This is an important technique to gain information on the tunneling characteristics of the MTJs and the barrier quality[72]. It is sufficient to record the IV characteristics in the p and ap states. A continuous sweep of the external field is not necessary.

3.1.4. Tunnel magneto-Seebeck voltage

For the determination of the Seebeck voltage of the MTJ, a voltage preamplifier with a subsequent lock-in detection in combination with an oscilloscope to monitor the temporal evolution of the signal is used. An overview of the electronic equipment and the wiring is given in Fig. 3.4. In the standard configuration the connections indicated by the red dashed-dotted lines are used.

For the measurement, the bottom and top contacts of the MTJ are connected to a precision voltage amplifier (DLPVA-100-F-S, input impedance 1 TΩ, switchable gain up to 100 dB, switchable AC/DC coupling, switchable bandwidth 1 kHz/100 kHz). The standard Seebeck measurements are performed with the amplifier in DC mode at a gain of 60 dB (factor of 1000) and a bandwidth of 100 kHz. Similarly to the TMR measurements, the bottom electrode is connected to the ground of the amplifier.

The high impedance of the amplifier is crucial to avoid leakage currents that generate parasitic changes of the detected Seebeck voltages when the MTJ is switched from p to ap. A detailed explanation on how artificial TMS effects evolve from leakage currents through the amplifier is found in Appendix B. Here, it is only pointed out that they are small enough to be neglected for typical sizes of the TMS effect. The largest artificial TMS effect is expected for the MTJs with the highest resistances ($R_\mathrm{p} \approx 2\,\mathrm{M\Omega}$ and $R_\mathrm{ap} \approx 4\,\mathrm{M\Omega}$) that are still three orders of magnitude smaller than the input impedance. The change in resistance causes a maximum artificial TMS effect of $\approx 0.2\,\%$, which is taken into account as an error for the TMS measurements. Nevertheless, the error is small enough to not drastically influence real TMS effects in the order of at least several percent. For MTJs

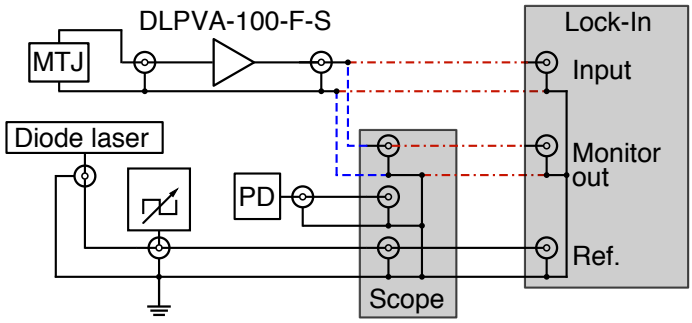

Figure 3.4. Electric connections and electronic equipment: The red dashed dotted lines indicate the connections to the lock-in amplifier. The blue dashed lines symbolize a direct connection of the sample to the oscilloscope without the lock-in amplifier (adapted from Ref. 17).

with resistances of below 100 kΩ the artificially generated TMS effect due to leak currents reduces to less than 0.01 %. Thus, for typical Seebeck voltages of 10 µV to 100 µV in the MTJs with lower resistance, this artificial TMS effect resembles a change in the voltage of $\Delta V = 1$ nV to 10 nV, and, thus, is negligible.

The output voltage of the voltage amplifier is passed to a lock-in amplifier (Stanford Research Systems SR830) set to voltage mode and locked to the modulation frequency of the diode laser. The TMS effect is determined by performing minor or major loops similar to the TMR effect measurements (cf. Sec. 3.1.3). For every point along the loop the external magnetic field is kept constant for a duration of at least three time constants of the lock-in amplifier. This allows the proper saturation of the Seebeck signal after the magnetic field has changed. This lock-in signal in combination with the applied temperature gradient is used to calculate the Seebeck coefficients $S = V/\Delta T$ (Eq. 2.9) in the p and the ap state of the MTJ.

The voltage signal is further controlled by a scope connected to the monitor out of the lock-in amplifier. The scope allows the observation of the saturation of the signal and the choice of the appropriate modulation frequency for the

laser. In addition, the scope can be used to record the temporal evolution of the signal (see Sec. 3.1.5).

3.1.5. Temporal evolution of the Seebeck voltage

The temporal evolution of the Seebeck voltage is an important information for determining the correct frequency for the lock-in measurement. To exactly compare the on/off cycle of the laser with the evolution of the Seebeck voltage not only the voltage signal is fed to the oscilloscope, but also the reference signal from the waveform generator and the response of the photo diode are monitored on individual channels of the oscilloscope.

The voltage signal is fed to the scope via two different paths. First, it can be taken from the monitor out of the lock-in amplifier, as described in the previous section. This is particularly useful, if only the shape of the voltage signal is of interest and a magnetic field sweep is performed. Alternatively, the oscilloscope can be directly connected to the voltage amplifier. The necessary connections are marked by the blue dashed lines in Fig. 3.4. This second method is preferable, if also the size of the signal and the baseline, i.e., when the laser is turned off, are of interest. With this method the signal is only modified by the precision amplifier and, hence, less falsified.

Nevertheless, it has to be taken into account that the scope detects the peak-to-peak voltage $\hat{V}$ of the rectangular voltage input. The lock-in amplifier, however, is only sensitive to the first component of the Fourier series of this signal, because the rectangular signal is multiplied by the sinusoidal internal reference of the lock-in amplifier and integrated over time. This equals a Fourier transformation of the rectangular signal[73]:

$$V_{\mathrm{FT}}(t) \approx \frac{\hat{V}}{2} \cdot (1 + 1.273 \sin(\omega t) + 0.42 \sin(3\omega t) + 0.254 \sin(5\omega t) + \dots) \quad (3.3)$$

When the lock-in is set to the first harmonic, it only detects the first component of this Fourier series. Furthermore, the lock-in amplifier measures the root-mean-square (RMS) value of the first harmonic. Accordingly, the lock-in output of the rectangular input signal yields

$$V_{\mathrm{lock-in}}^{\mathrm{RMS}} \approx 0.45 \cdot \hat{V}. \quad (3.4)$$

For the derivation of the TMS effect ratio from the oscilloscope traces, the voltages in the p and the ap state of the MTJ are recorded under applied magnetic field. For an investigation of the temporal evolution, also the diode signal has to be recorded as a reference signal for the modulation of the heating.

Since the temporal evolution of the Seebeck voltage is recorded in the p and in the ap state of the MTJ, the Seebeck coefficients S_{p} and S_{ap} of the MTJ can also be determined using the saturated peak-to-peak voltage of the oscilloscope. This method in in even better agreement with the definition of the Seebeck coefficient than deriving the Seebeck coefficient from $V_{\mathrm{lock-in}}^{\mathrm{RMS}}$. Taking the RMS Seebeck voltage from the lock-in amplifier (cf. Sec. 3.1.4) only provides the "RMS Seebeck coefficient". However, up to now, Seebeck coefficients of MTJs have always been determined from the lock-in signal, e.g., by Walter *et al.* [4] and Liebing *et al.* [20]. To fulfill this convention introduced in these publications all Seebeck coefficients in this thesis are determined from the lock-in RMS readings, unless it is explicitly specified.

3.1.6. Tunnel magneto-Seebeck current

So far, only Seebeck voltage measurements were introduced. However, Eq. 2.6 suggests that applying a temperature difference to an MTJ also generates a Seebeck current $I = G \cdot S\Delta T$. With the information on the resistance $R = 1/G$ of the sample this current is used to determine the size of the Seebeck voltage $S\Delta T = I \cdot R$ independently of the direct Seebeck voltage measurement introduced in Sec. 3.1.4.

For the measurement of the Seebeck current, the voltage amplifier is removed and the MTJ is directly connected to the lock-in amplifier in current mode (input impedance 1 kΩ to virtual ground[1]). Magnetic field sweeps, similar to the TMR effect and Seebeck voltage measurements, are performed to obtain the switching behavior of the Seebeck current when the MTJ state is changed between p and ap.

[1] Refer to the manual of the SR830 DSP lock-in amplifier for more detailed information.

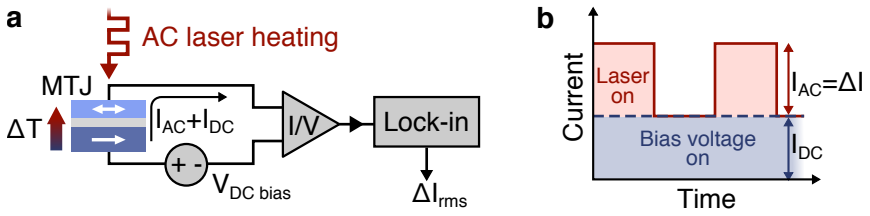

Figure 3.5. Setup for Seebeck effect measurements under applied bias voltage: **a** Schematics of the circuit with the DC voltage source connected to the AC heated MTJ. The generated current is fed to a I/V converter that passes the signal to a lock-in amplifier. **b** Temporal evolution of the laser induced AC Seebeck current and the voltage induced DC current. The lock-in amplifier that rejects the DC current only detects the root-mean-square (rms) value of the amplitude of the AC current generated by the heating of the MTJ.

3.1.7. Seebeck effect under applied bias voltage

In Sec. 2.4.1 was shown that Seebeck effect measurements under an applied bias voltage are an efficient tool to easily tune the chemical potentials in the electrodes of an MTJ. However, it has been revealed that it is not feasible to simultaneously apply a bias voltage and directly determine the Seebeck voltage of the MTJ. To overcome this problem a current measurement under an applied temperature gradient and under an additional bias voltage are performed. In the linear approximation the current contains a Seebeck and a voltage driven contribution (see Eq. 2.6). This enables regaining the bias-Seebeck coefficient from the experimentally detected current signal. In this section, an experimental approach to achieve this objective is introduced.

The circuit for this measurement mode of the TMS setup is depicted in Fig. 3.5a. Like in the standard magneto-Seebeck effect measurements, the modulated laser beam is used to generate a temperature gradient across the MTJ. This gradient leads to an AC Seebeck current inside the MTJ that is fed to a variable-gain transimpedance amplifier (FemtoDLPCA-200 current to voltage converter, gain 10^5 V/A to 10^6 V/A, AC coupling). The cut-off frequency is at least 200 kHz with a rise time of 1.8 ms, which is sufficient for measurements at 1.5 kHz. The amplifier is simultaneously

used to apply the desired DC bias voltage of up to ±300 mV to the MTJ. The output signal of the transimpedance amplifier is passed on to a lock-in amplifier set to AC voltage mode with an integration time of 100 ms. The reference signal for the lock-in amplifier is the signal of the waveform generator, which controls the laser modulation. Hence, the lock-in amplifier provides an improved signal-to-noise ratio and, more importantly, it rejects the DC current that is generated by the bias voltage, which is independent of the Seebeck coefficient. Thus, it only detects the change of the current that is generated by the laser heating of the MTJ (Fig. 3.5b). A detailed description of the contributions to this current signal ΔI is presented in Sec. 2.4.1.

3.2. Fabrication of magnetic tunnel junctions

The MTJ samples for the TMS investigations are fabricated from different sputter deposited layer stacks. All these stacks have in common that they contain two ferromagnetic layers separated by a thin tunnel barrier forming the MTJ. The material of these layers can vary, as well as the exact composition and sequence of the surrounding layers. They are chosen according to the desired properties.

After the deposition and optional thermal annealing the sample stacks are patterned. The cross section of the final sample is depicted in Fig. 3.6a. It displays the MTJs on a bottom contact below the MTJs that extends over the whole area of the sample. The bottom contact provides electrical access to the bottom ferromagnet (FM2) of all MTJs through a single gold contact close to the edge of the sample. The top ferromagnet (FM1) is connected to a top electrode that is placed on top of an insulator. A good quality insulator is crucial to avoid shorting between the top and bottom contact, as well as the individual MTJs. The shape of the top contact still allows optical access to the gold above the MTJ, even if a 25 µm bond wire is placed on the contact pad (Fig. 3.6b, and cf. Fig. 3.3 in Sec. 3.1.2). The position of the top contact with respect to the MTJ, as well as its size and thickness are chosen such that even a large laser spot with a diameter of 20 µm is still fully absorbed by the gold layer (Fig. 3.6c). Thus, a direct laser irradiation of the ferromagnetic layers or the bottom contact trough the insulator is excluded.

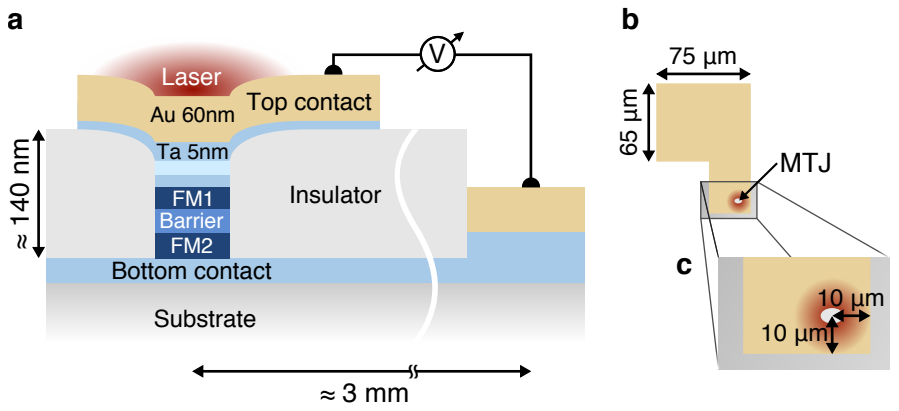

Figure 3.6. MTJ samples after lithography: **a** Schematic cross section of the patterned MTJs consisting of two ferromagnets (FM1, FM2) separated by a tunnel barrier. **b** Top view of a single MTJ with top contact pad and 20 µm laser spot. **c** Enlarged section of the top view. The MTJ is positioned such that a 20 µm laser spot is not extending over the edges of the gold pad.

The lithography process for preparing theses samples is nearly the same for all sample stacks and is explained in the next paragraphs. The deposition of the layer stacks is explained in Secs. 3.2.1 and 3.2.2.

In a first step, the MTJ pillars are produced by electron beam (e-beam) lithography and subsequent Ar ion etching. After the sample is coated with an e-beam negative resist (AR-N 7520-18 at 5000 rpm for 30 s, bake out 2 min at 80 °C) it is exposed using a Zeiss Leo 1530 scanning electron microscope (SEM) equipped with a high precision interferometer sample positioning stage and a Raith lithography unit. A detailed review on electron-beam lithography is found in Ref. 74. After development of the resist, the bottom electrode is covered using a marker pen and the sample is etched by Ar ions until only the MTJ pillars under the exposed resist and a metallic bottom electrode extending over the whole sample remain. The depth of the etching process is monitored by a secondary ion mass spectrometer (SIMS) that collects ions emitted from the etched surfaces. Subsequent to the etching

process, the MTJ pillars are insulated by ≈ 140 nm of a sputter deposited insulator, e.g., Ta_2O_5 or Si_3N_4[2]. Finally, the remaining resist and marker are removed in an ultrasonic bath of 1-Methyl-2-pyrrolidinone to allow electric access to the top and bottom contacts.

In a second lithography step, gold contact pads are placed on top of the MTJs. For this purpose, 5 nm of Ta and 60 nm of Au are DC sputter deposited on the sample. The sample is coated with negative resist and the pattern of the pads is exposed by e-beam lithography. The bottom contact is again covered by applying a marker pen. The exposed and developed sample is Ar ion etched until the insulator adjacent to the MTJs is reached, and no conducting material remains between the contact pads. Finally, the resist and the marker are removed in an ultrasonic bath.

3.2.1. Co-Fe-B/MgO/Co-Fe-B MTJs for bias dependence

For the TMS measurements under an applied bias voltage Co-Fe-B (2.5 nm)/ MgO (1.7 nm)/Co-Fe-B (5.4 nm) pseudo spin valve structures patterned into elliptic MTJs of 4 µm × 6 µm are used. The layer stacks for the MTJs are produced in an home-built ultra high vacuum (UHV) sputtering chamber (base pressure 10^{-9} mbar) on MgO substrates and consist of Ta 10/$Co_{26}Fe_{54}B_{20}$ 2.5/MgO 1.7/$Co_{26}Fe_{54}B_{20}$ 5.4/Ta 5/Ru 3 (numbers represent thickness in nm). After the preparation, the stacks are annealed at 450 °C for one hour in an external magnetic field of 300 mT. The MTJs are patterned using the previously described e-beam lithography and subsequent Ar ion milling. The Ta layer beneath the Co-Fe-B serves as the bottom electrode. SiO_2 or Si_3N_4 are deposited around the MTJs as an insulator. Afterwards, gold contact pads are deposited on top of the MTJs, as sketched in Fig. 3.6. A schematic of the layer stack and function of the individual layers is depicted in Fig. 3.7.

3.2.2. Heusler compound MTJs

For the investigation of the TMS effect with respect to different DOSs, two types of Heusler based MTJs are used. In the first type the MTJ is formed by Co_2FeSi/MgO/$Co_{70}Fe_{30}$. The second type contains a different Heusler

[2]The specific insulators for each MTJ type are given in Secs. 3.2.1 and 3.2.2

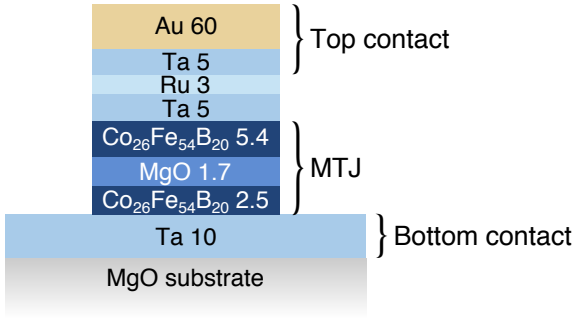

Figure 3.7. Layer stack of the Co-Fe-B MTJs: The $6\,\mu m \times 4\,\mu m$ elliptical MTJ pillars are patterned down to the Ta 10 nm layer that serves as a bottom electrode.

compound, Co_2FeAl, and the MTJs consist of $Co_2FeAl/MgO/Co_{40}Fe_{40}B_{20}$. The layer stacks for these MTJs are sketched in Fig. 3.8.

The layer stacks of the Co_2FeSi based MTJs are prepared in a BesTec DC/RF magnetron co-sputtering system with a base pressure of 10^{-9} mbar. A 5 nm Cr seed layer on top of a 5 nm MgO buffer layer has proven to provide the optimum growth conditions for the Co_2FeSi Heusler compound [65,75]. These layers are sputter deposited on MgO(001) substrate and *in situ* annealed at 700 °C. Afterwards, 20 nm of epitaxial Co_2FeSi are deposited by DC magnetron co-sputtering from elemental targets at room temperature in an Ar atmosphere with a pressure of 2×10^{-3} mbar. The 2 nm thick MgO barrier is RF sputter deposited on top of the Co_2FeSi. A $Co_{70}Fe_{30}$ counter electrode of 3 nm thickness is DC sputter deposited from a composite target. The counter electrode is exchanged biased by a 10 nm thick antiferromagnetic $Mn_{83}Ir_{17}$ layer that is sputter deposited from a composite target. The stack is capped with 25 nm of Ru.

Afterwards, the stack is *ex situ* annealed at 325 °C for 1 h in an in-plane magnetic field of 6.5 kOe. This post annealing process increases the crystallinity of the MgO barrier [76], which is important for coherent tunneling. Furthermore, heating the antiferromagnetic Mn-Ir over its blocking temperature and performing a subsequent field cooling process allows to align the direction of the pinning along the external magnetic field [77].

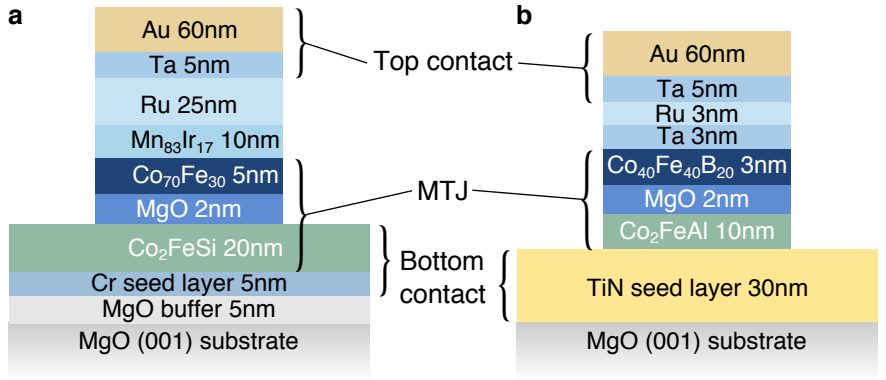

Figure 3.8. Heusler based MTJs: a Top pinned Co-Fe/MgO/Co_2FeSi MTJs. The Co_2FeSi layer also serves as bottom contact. **b** Co-Fe-B/MgO/Co_2FeSi MTJs. Here, the TiN seed layer provides the bottom contact.

For the patterning of the elliptical MTJs the stacks are etched down to the Co_2FeSi layer which serves as a bottom contact, and, accordingly, has to cover the whole sample (see Fig. 3.6). The remaining MTJ pillars of different sizes are insulated by 140 nm of Ta_2O_5. The Ta_2O_5 layer is deposited by reactive RF sputtering from a Ta target in an Ar-O atmosphere with 12 % oxygen. Afterwards, the top contact pads consisting of Ta 5 nm/Au 60 nm are deposited on top of the MTJs.

The layer stack of the Co_2FeAl Heusler compound samples possesses a 30 nm TiN buffer layer directly deposited on a MgO(001) substrate. The TiN layer is reactively sputter deposited in the BesTec sputtering chamber. During the deposition, the substrate is heated to 450 °C, and 2 sccm of nitrogen gas and 20 sccm of argon gas are introduced into the chamber. The nitrogen atoms react with the Ti atoms of the elemental Ti sputter target and form TiN. The 10 nm of Co_2FeAl are sputter deposited from a stoichiometric target in a Leybold CLAB 600 sputtering chamber (base pressure of 10^{-7} mbar) at room temperature. The 2 nm MgO barrier is RF sputter deposited from an MgO target and the 3 nm $Co_{40}Fe_{40}B_{20}$ counter electrode is DC sputter

deposited from a stoichiometric target in the same chamber. A double layer of Ta 3 nm/Ru 3 nm is added for capping of the MTJ layers.

The layer stack is then *ex situ* annealed at 325 °C for 1 h in an in-plane magnetic field of 6.5 kOe to increase the crystallinity of the MgO barrier and to obtain a crystalline Co-Fe layer at the interface to the MgO [76,78].

3.3. X-ray analysis

X-ray diffraction (XRD) is a common technique for determining the crystalline structure of solids. For the investigation of Heusler films, gaining this information is crucial to check the desired crystalline properties of the individual layers. In particular, their electronic structure sensitively depends on the correct crystalline order (cf. Sec. 2.4.2). A more detailed explanation of the technique is found in Refs. 79, 80 and 81. The following short introduction is based on these references.

XRD exploits the diffraction of X-rays on crystals. X-rays with a wavelength λ scatter at the lattice planes of the crystal with an interplanar distance d (Fig. 3.9a). Constructive interference between two scattered waves occurs when the path lengths differ by an integer multiple of the wavelength. The path difference between the interfering waves is $2d\sin(\theta)$, with the scattering angle θ. Accordingly, the constructive interference of X-rays that are scattered by the crystallographic planes is given by Bragg's equation

$$n\lambda = 2d \cdot \sin(\theta), \tag{3.5}$$

where, $n \in \mathbb{N}$ denotes the order of diffraction.

In crystals, planes are indexed by the Miller indices h, k, and l. The notation (h,k,l) defines planes that are orthogonal to the reciprocal lattice vectors $\mathbf{b}_1$, $\mathbf{b}_2$ and $\mathbf{b}_3$ [28,46]

$$\mathbf{G}_{h,k,l} = h\mathbf{b}_1 + k\mathbf{b}_2 + l\mathbf{b}_3$$

Different (h,k,l) are accessed by XRD by tilting the crystal around the axes ψ and φ (cf. Fig. 3.9b).

The X-ray investigations presented in this thesis are performed in a Phillips X'Pert Pro MPD X-ray diffractometer with Cu K_α radiation at a wavelength

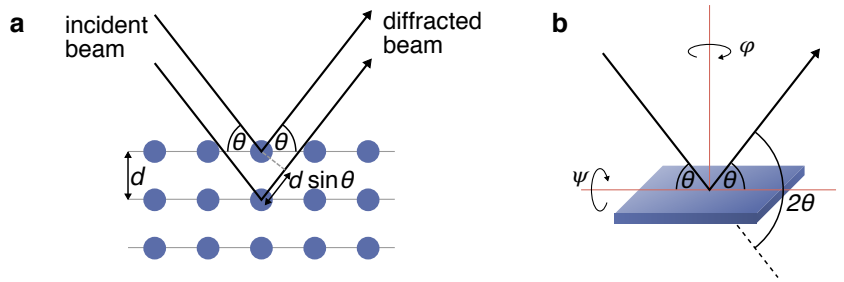

Figure 3.9. Geometry of the XRD measurement: a Diffraction at the lattice planes according to Bragg's equation. **b** By rotating the sample around the angles ψ and φ different lattice planes can be investigated.

of 1.5419 Å in a θ-2θ geometry. Usually, a full XRD scan covers the interval of $2\theta = 20° - 125°$. Standard θ-2θ scans are performed in the Bragg-Brentano geometry. For detecting the Heusler (111), (222) and (444) peaks an Eulerian cradle is used for tilting the sample around the ψ and φ axes.

Furthermore, by using X-ray reflectivity (XRR), the roughness and the thickness of the deposited layers are determined [82,83]. This is particularly interesting for the Heusler layers and the MgO barrier. To perform an XRR investigation the same setup is used as for the XRD scans, but at small θ angles. Small θ angles result in total reflection of the incident beam at the sample surface, but if the angle is slightly enlarged, the intensity of the beam reflected at the surface of the sample falls off rapidly, and reflections of the beam at all interfaces in the sample occur. With rising θ, the interference of the reflected individual beams leads to a pattern of maxima and minima, so called Kiessig fringes. From these fringes, the thickness of the layers, their roughness, and their mass density are deduced [81].

3.4. Finite element simulations

The determination of a temperature difference across the nm thick barrier of an MTJ is a nontrivial task. It is impossible to bring a thermometer close to the electrode/barrier interface to determine the temperatures on each side,

since the thermometer itself strongly influences the thermal conductance through the layer stack. Consequently, up to now it has remained impossible to experimentally determine the temperature gradient in an MTJ directly.

Therefore, COMSOL Multiphysics finite element simulations are performed to determine the rise of the base temperature and the achieved temperature gradient over the MgO barrier, when the laser is applied to the top of the MTJ.

For the simulation, the thermal conductivity κ, the specific heat c_p and the mass density ρ of all layers in the MTJ are needed. An overview of these values is given in Tab. 3.1. The mass densities of the Heusler compounds are determined by XRR experiments where the data are fitted by the Parratt algorithm to obtain the thickness, mass density and roughness of the films. Since data for the thermal conductivity κ of Heusler compounds are not available for Co_2FeSi and Co_2FeAl, values of different Co and Fe based Heusler compounds are compared and an average value of $20\,W\,m^{-1}\,K^{-1}$ [84,85] is used. Furthermore, there are no data available in literature for the specific heat c_p of the Co_2FeSi and Co_2FeAl Heusler compound. However, a value of $424\,J\,kg^{-1}\,K^{-1}$ for Co_2VSi [86] is found in literature. Co_2VSi possess the Heusler structure X_2YZ with $X = Co$ and $Z = Si$, and exhibits a gap in the DOS close to the chemical potential [87,88], similar to the studied compounds.

Yet, it has to be noted that these finite element simulations only give an approximate value for the temperature gradients in the MTJs. Especially, the thermal properties of the thin MgO barriers are currently intensively discussed. So far the thermal conductivity has been assumed to be equal to experimentally determined thin film values by Lee *et al.* [93]. A much more recent work by Zhang *et al.* [96] predicts values of the thermal conductivity that are ten times smaller. An experimental evidence for these predictions is still pending. Of course, these differences in the thermal conductivity of MgO strongly influence the size of the simulated temperature gradient. Hence, the Seebeck coefficients calculated with the data given in Tab. 3.1 should only be compared to values based on similar simulations performed with the same parameters, e.g., in Refs. 4,17,18.

Table 3.1. Material parameters for COMSOL simulations: If not specified otherwise, the values are taken from Refs. 4,20,89,90. The density of the Heusler compounds and the TiN layers are taken from XRR measurements. The thermal conductivities used in the simulations are printed in bold letters. Experimental thin film values are given if available.

Material	$\rho\,(10^3\,\frac{\mathrm{kg}}{\mathrm{m}^3})$	$c_\mathrm{p}\,(\frac{\mathrm{J}}{\mathrm{kg\cdot K}})$	κ_bulk / $\kappa_\mathrm{thin}^\mathrm{exp}\,(\frac{\mathrm{W}}{\mathrm{m\cdot K}})$
Au	19.32	128	**320.0** / 70 [91] – 170 [92]
Cr	7.15	449	**94.0**
Ru	12.37	238	**117.0**
Ta	16.65	140	**57.0**
Ta_2O_5	8.27	306	**0.2**
$Ni_{80}Fe_{20}$	8.7	460	**19.0**
Ir-Mn	10.18	69.7	**6.0**
Co-Fe-B	8.22	440	**86.7**
MgO	3.58	935	48.0 / **4.0** [93]
SiO_2	2.20	1052	**1.4**
Si	2.33	700	**150.0**
SiN	3.11	700	**35.9**
Co_2FeAl	6.8	424 [86]	**20** [84,85]
Co_2FeSi	7.2	424 [86]	**20** [84,85]
TiN	5.45	604 [94]	**28.8** [95]

Chapter 4

Results

4.1. Typical TMS measurements with laser heating

Before immersing deeply into the experimental observations of the TMS and bias TMS effects in different types of MTJs, this section gives a profound introduction to typical TMS experiments and the important information that can be extracted from the data. Since this is an introduction, first, TMR and TMS measurements of the most common MTJ type with an MgO barrier and Co-Fe-B electrodes are presented. As seen before, this material combination sets the benchmark for the development of improved MTJ devices. Consequently, effects observed with other material combinations are always judged against Co-Fe-B/MgO/Co-Fe-B MTJs. Some of the results presented in this section have been published in Refs. 17 and 18, which directly emerged from the work performed for this thesis.

Fig. 4.1a displays the dependence of the resistance of a $Co_{40}Fe_{40}B_{20}$/MgO 1.7 nm/$Co_{40}Fe_{40}B_{20}$ MTJ on an external magnetic field. The resistance changes abruptly between $R_p = 67\,k\Omega$ in the p state and $R_{ap} = 215\,k\Omega$ in the ap state. This switching is caused by the TMR effect (Sec. 2.1). The alignment of the magnetization in the electrodes of the MTJ is indicated by the small arrows. The change in resistance results in a TMR ratio (cf. Eq. 2.1) of 220 %. The clear switching between high and low resistance in combination with a high effect ratio reveals the two most beneficial prop-

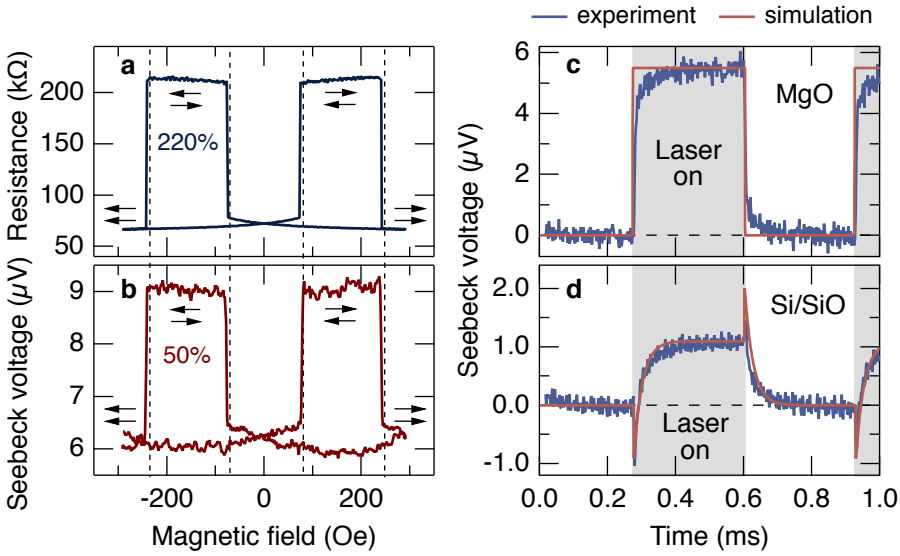

Figure 4.1. Typical TMR and TMS measurments of Co-Fe-B based MTJs: a TMR of a $Co_{25}Fe_{55}B_{20}$ based MTJ at a 10 mV bias voltage. **b** TMS of the same MTJ at 150 mW laser power. **c** Temporal evolution of the Seebeck voltage at 10 mW laser power of a $Co_{40}Fe_{40}B_{20}$ based MTJ on MgO substrate. **d** Temporal evolution of a similar MTJ on Si/SiO_2 substrate. The curves in c and d are recorded in the p state. The red curves in c and d are simulations based on a model circuit [17].

erties of Co-Fe-B/MgO/Co-Fe-B MTJs and their advantages for spintronic applications.

Fig. 4.1b exhibits the TMS effect of the same MTJ. The Seebeck voltage under 150 mW laser power reaches 6 µV in the p and 9 µV in the ap state of the MTJ. This voltage is much too small for the detection of "logic on" or "logic off" in modern electronic devices that are typically operated at "logic on" voltages of ≈ 1 V [97]. Although the MTJ reveals a TMR ratio of 220 % the TMS ratio only amounts to 50 %. This is due to the fact that the TMR and TMS effects are generated by different properties of the electronic states .

If the Seebeck voltage is investigated in dependence of the external field, a switching between the high and low states is observed exactly at the same field values as the switching of the resistance in the TMR experiment. Hence, the change of the Seebeck voltage and the switching of the resistance are related to the same magnetization reversal of the electrodes of the MTJ.

In Figs. 4.1c,d the temporal evolution of the Seebeck voltage in $Co_{40}Fe_{40}B_{20}$/ MgO 1.5 nm/$Co_{40}Fe_{40}B_{20}$ MTJs in the p state on MgO or Si/SiO_2(50 nm) substrates is presented. The traces are recorded at a laser power of 10 mW at a modulation frequency of 1.5 kHz. An additional peak at laser on/off is found when the Seebeck experiments are performed on MTJs on Si substrate. At first sight, this observation is puzzling, since the 50 nm of SiO_2 prevents any electrical contact between the semiconducting Si (resistivity of 20 Ω cm) and the MTJs. This excludes the direct interference of the voltage detection at the MTJ by a Seebeck or photo effect in the Si, as proposed by Xu *et al.* [22]. A closer examination, however, reveals that the additional spikes for the MTJs on Si originate from a Seebeck effect in the substrate that is capacitively coupled to the bottom lead of the MTJs [17]. In an insulator, such as MgO, the Seebeck effect cannot occur, and hence no spikes are observable in the temporal evolution of the Seebeck voltage detected in MTJs on MgO substrate. This assumption is proven by performing simulations of model circuits with and without an additional capacitively coupled voltage source in the substrate. The retrieved curves with capacitively coupled voltage source nicely resemble the spikes observed for the Si substrate (Fig. 4.1d), whereas no spikes are found for the model circuit without a capacitively coupled voltage source (Fig. 4.1c).

These results reveal two important requirements that have to be fulfilled to realize a reliable detection of the TMS effect. First, a sharp laser on/off switching has to be performed to accomplish quick rise and fall times of the voltage signal from the Seebeck effect. The high temporal resolution of the oscilloscope in combination with the sharp on/off switching of the heating allow the detection of parasitic effects, such as the capacitive coupling on Si substrate. Second, it is highly advisable to use insulating substrates that prevent the generation of additional electrical signals generated by inductive or capacitive coupling. The importance of this second point is highlighted by a report on a "Giant thermoelectric effect in Al_2O_3 magnetic tunnel junctions"

with Co-Fe electrodes by Lin *et al.* [24], in which they report Seebeck voltages of up to one millivolt and TMS effect ratios of up to 40 %, which is in the range of the TMR ratio of the investigated MTJs. Recently, however, they had to correct these results, since they found that in their MTJ samples a large photo voltage in the substrate can be the origin of the "[...] large light induced voltage in magnetic tunnel junctions grown on semiconductor substrates"[22]. Hence, they "believe that the large effect could be the result of an experimental artifact"[22]. To avoid any misinterpretation of the signals stemming from conducting or semiconducting substrates, insulating MgO is chosen as substrate for all Seebeck experiments discussed in the following sections of this thesis.

4.2. Temperatures in the MTJs

During the laser irradiation a temperature difference is generated across the MgO barrier of the MTJs. Additionally, the base temperature rises. COMSOL simulations are performed to estimate the size of both effects. An introduction to this method was given in Sec. 3.4. In this section the results of the simulations are presented. For the simulations the MTJ sizes, the laser spot size and the laser power are chosen according to the values used in the experiments. Furthermore, the influence of the size of the laser spot on the temperature profile in the MTJs is investigated.

4.2.1. Heusler compound MTJs

For the simulations of the temperature evolution upon heating in the Heusler compound based MTJs, a round MTJ of 3 µm in diameter is assumed. The laser spot is modeled as a Gaussian beam with a beam waist of 5 µm. This value equals the experimentally determined beam diameter of 10 µm. For the laser with a power of 150 mW, a power of 120 mW is measured at the position of the sample. Hence, this value is used in the simulations.

Fig. 4.2 displays the results of the COMSOL simulations for the Co_2FeAl and Co_2FeSi based MTJs. In Fig. 4.2a it can be seen that a temperature gradient is generated across the barrier of the MTJ, pointing from the bottom Heusler electrode (lower temperature) to the top electrode. The gradient

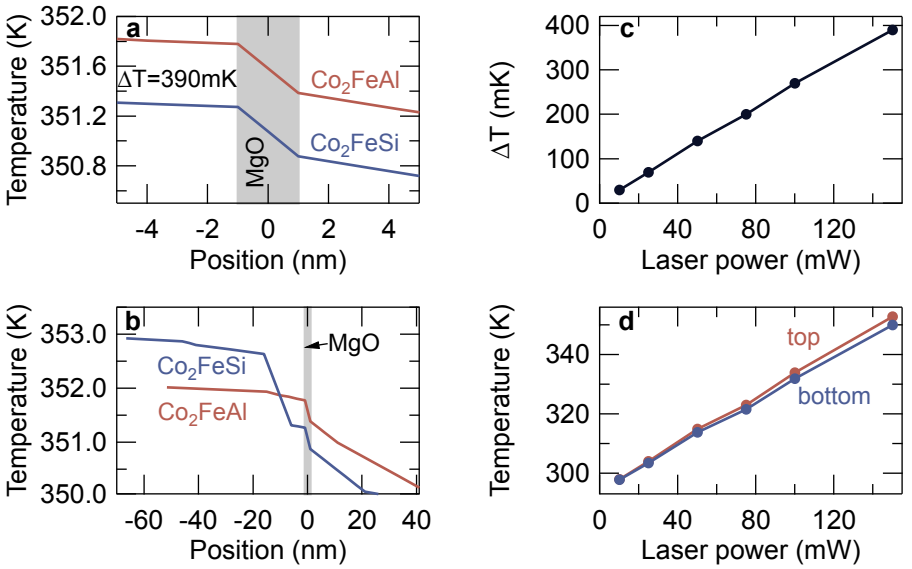

Figure 4.2. Simulated temperature gradients in the Heusler based MTJs: a ΔT across the 2 nm MgO barrier at 150 mW laser power. **b** Temperature evolution over the whole layer stacks. **c** Dependence of ΔT in the Co_2FeAl based MTJs on the applied laser power. **d** Increase of the base temperature $\overline{T}$ with laser power for the Co_2FeAl based MTJs.

across the insulating barrier is much steeper than the gradient generated in the metallic electrodes. This gradient over the barrier is the driving force for the Seebeck induced tunneling of electrons across the electrodes and enters the Landauer model in Eq. 2.9 as ΔT. This gradient is also used to calculate the Seebeck coefficients from the experimentally determined Seebeck voltages. This is in accordance with other TMS experiments performed by Walter *et al.* [4] and Liebing *et al.* [5,20]. The obtained gradients amount to a ΔT of 390 mK for the laser set to a power of 150 mW for both Heusler based MTJ types.

However, if the temperature change at all interfaces, i.e., over all layers of the MTJ (Fig. 4.2b), is considered, a second much larger gradient is

observed in the Co_2FeSi based MTJs. This gradient is attributed to the Mn-Ir pinning layer. Mn-Ir has a much lower heat conductivity than the surrounding layers (cf. Tab. 3.1), and hence, supports the generation of a temperature gradient. For the Co_2FeAl based MTJs that do not contain an Mn-Ir layer, no second gradient, that is equally steep as the gradient over the MgO barrier, is observed. The large second gradient in the Co_2FeSi based MTJs makes it necessary to check if the determined voltage indeed is mostly generated by the temperature gradient across the MgO barrier, and not by the second gradient in the samples. This is done by breaking the MgO barrier and determining the remaining Seebeck voltage, as discussed in detail in Sec. 4.4.

For the Co_2FeAl based MTJs simulations with different laser powers are performed (Figs.4.2c,d). The generated temperature gradients rise linearly with the laser power and range between 30 mK for the laser set to 10 mW and nearly 400 mK for the laser set to 150 mW. Also, the base temperatures for different laser powers rise linearly from room temperature to approximately 350 K at 150 mW laser power. Since the temperature increases linearly with the applied laser power, a linear increase of the Seebeck voltage with laser power is expected. However, due to the simultaneous rise of the base temperature, it is possible to observe the temperature dependence of the Seebeck coefficients. This dependence might lead to a deviation of the Seebeck voltage from the expected ideal linear behavior.

4.2.2. Co-Fe-B based MTJs

The simulation of the temperature gradient in the Co-Fe-B based MTJs, in which the TMS effect under applied bias voltage is investigated, are performed with a spot diameter of 20 µm and the laser power set to 150 mW. The elliptical MTJ has a size of 6 µm × 4 µm. The obtained results exhibit a rise of the base temperature from room temperature (293 K) to 306 K when the laser power is set to 150 mW. Simultaneously, a temperature gradient of 11 mK is generated across the 1.5 nm thick MgO barrier. The calculated value is much smaller than in the Heusler compound MTJs. This is owed to the larger beam diameter, the increased MTJ size and the decreased barrier thickness.

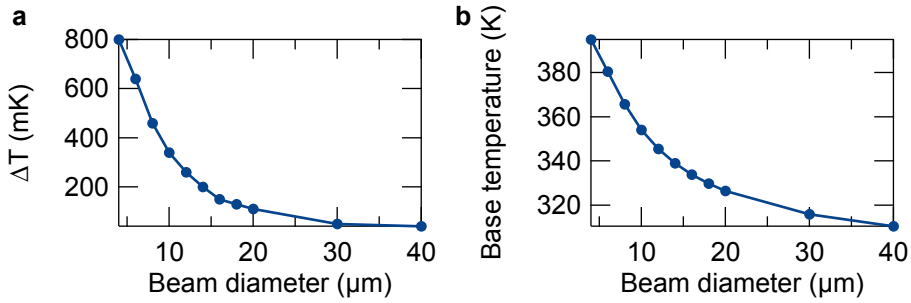

Figure 4.3. Dependence of the temperatures on the beam size in the Co_2FeAl based MTJs: a The temperature difference across the MgO barrier. **b** The base temperature in the center of the MgO barrier. The simulations are performed for the laser set to a power of 150 mW.

4.2.3. Dependence on laser spot diameter

For the Co_2FeAl based MTJs simulations of the temperatures with different sizes of the laser spot have been conducted (Fig. 4.3). The smallest diameter is chosen to be 4 µm and the largest to be 40 µm. Within this range, a significant drop of the temperature difference across the MgO barrier from $\Delta T = 800$ mK for the smallest beam size to 50 mK for the largest beam is obtained. Simultaneously, the base temperature decreases from 390 K to 310 K.

These results reveal how drastically the size of the laser spot influences the Seebeck effect measurements. Hence, the beam size has to be carefully checked before or after each measurement by the knife edge method as described in Sec. 3.1.1.

4.3. Tunnel magneto-Seebeck effect under applied bias voltage

In Sec. 3.1.7 it has been seen, that applying a bias voltage to an MTJ that is heated by a modulated (on/off) heat source generates two effects. The

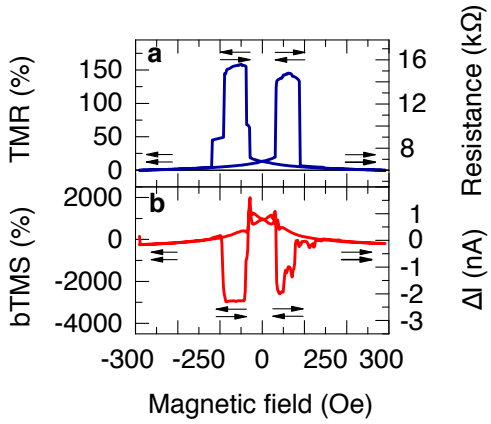

Figure 4.4. Comparison of tunnel magnetoresistance and bTMS effects: a TMR ratio and the resistance of the MTJ under a changing magnetic field. **b** Bias TMS ratio and measured current signal for a bias voltage of $-10\,\mathrm{mV}$ at 150 mW laser power. Here, the on/off behaviour ($\Delta I_\mathrm{p} = 0\,\mathrm{nA}$, $\Delta I_\mathrm{ap} = -2.3\,\mathrm{nA}$) is observed. Hence, the resulting effect ratio reaches nearly $-3000\,\%$ and is much higher than the TMR ratio observed at the same MTJ.

first effect is the bias-enhanced tunnel magneto Seebeck (bTMS) effect (see Eqs. 2.22 and 2.23). The bTMS effect describes the interaction of the currents that are generated by the external bias voltage V_bias and the Seebeck effect. The experimental work concerning this effect and presented in this section has been published in Ref. 18. Within this publication the total suppression of a tunnel current in an MTJ in only one magnetic state was reported for the first time. Up to now, only a change between finite resistances could be achieved by the tunnel magnetoresistance effect (Fig. 4.4a). The switching between on/off of the signal obtained from the MTJ as described by Eq. 2.22, is a new feature only established by the bTMS effect (Fig. 4.4b). It can only evolve from the combination of two gradients across the barrier, i.e., an electric field gradient and a temperature gradient.

To evaluate the TMS effect and its dependence on V_bias, first the tunnel resistance of the MTJ is characterized. Fig. 4.4a shows the dependence of the resistance on the magnetic field; the black arrows indicate the magnetizations

of the ferromagnetic electrodes. The TMR ratio attains approximately 150 %, which is a typical value for MTJs with a thin MgO layer of good quality [98,99]. Hence, the readout of the magnetic state of the MTJ is realized by measuring the resistance.

Nevertheless, the bTMS effect determined at a similar MTJ provides a much higher effect ratio of −3000 % (Fig. 4.4b). In this particular case, the high ratio is realized by combining a bias voltage of −10 mV with a temperature gradient across the barrier that is created using a laser power of 150 mW. The measured signal ΔI is the current difference between the heated and non-heated MTJ, which is approximately 0 nA in the p state and −2.3 nA in the ap state of the MTJ. The high effect ratio is created by this on/off behavior of the signal when the MTJ state is switched between p and ap. The high readout contrast and the on/off behavior are two advantages of the bTMS compared to the TMR effect when it is used to determine the state of an MTJ.

A more detailed investigation of this remarkable result is shown in Fig. 4.5a, where the measured current difference ΔI is plotted as a function of the external magnetic field for different values of V_{bias}. For V_{bias} between −20 mV and 20 mV, the measured values vary drastically and even change their sign (Fig. 4.5b), which again points out the striking result of these experiments; the signal ΔI can be switched on or off by reversing the magnetic state of the MTJ, which is also visible in Fig. 4.4b.

Figs. 4.5a-c show that ΔI reverses the sign from negative to positive for V_{bias} between 0 mV and −10 mV. However, ΔI_{p} and ΔI_{ap} do not change their sign at the same bias voltage. A zero ΔI_{p} is found at −10 mV. This zero crossing of ΔI_{p} and the finite value of ΔI_{ap} yield an infinite bias-enhanced TMS effect according to Eq. 2.22. Using these experimental data, a bTMS ratio of approximately −3000 % at $V_{\mathrm{bias}} \approx -10$ mV as shown in Fig. 4.4b and Figs. 4.5a–c for a laser power of 150 mW, is obtained. Moreover, ΔI_{ap} crosses zero at −3 mV, which is accompanied by a non-zero ΔI_{p}. Accordingly, an increased bTMS ratio is also found for −3 mV.

The divergences of the bTMS ratio become more obvious when a linear model is applied to the measured data and the bTMS ratio is calculated (Fig. 4.5c). This result and the zero crossings of ΔI_{p} and ΔI_{ap} were previously revealed in Eq. 2.22 and become evident by concentrating on small bias

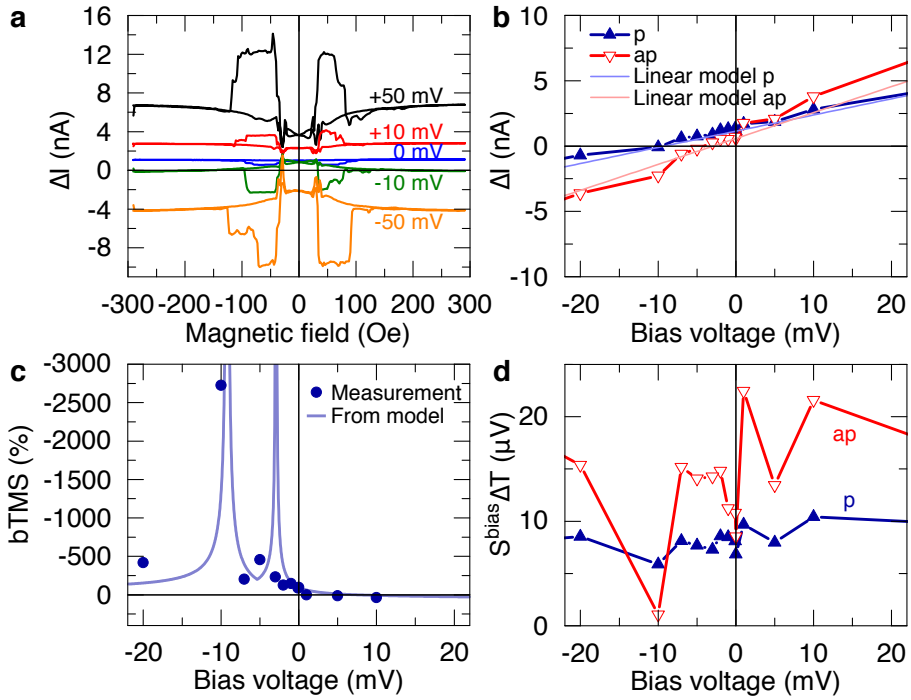

Figure 4.5. Bias tunnel magneto-Seebeck effect: **a** ΔI versus magnetic field for selected bias voltages. At $-10\,\mathrm{mV}$, the p signal is close to zero, whereas the ap signal is non-zero. This difference produces an on/off behavior. **b** Dependence of the measured current signal ΔI on the bias voltage for 150 mV laser power. ΔI_p and ΔI_ap cross zero at different values, which leads to an on/off behavior. The results from the linear model are shown as lines. **c** Bias TMS effect ratio derived from a. The light line is deduced from the linear model. The divergences and the high effect ratios are attributed to the vanishing ΔI in only one magnetic state of the MTJ (on/off behavior) at $-10\,\mathrm{mV}$ and $-3\,\mathrm{mV}$ bias voltage. **d** Seebeck voltages that are derived from Eq. 2.22 after subtracting the linear contribution.

voltages in Fig. 4.5. Since a vanishing ΔI signal is only found in one state of the MTJ at a certain bias voltage, ΔI can be switched from zero to a finite value only by changing the magnetic state of the MTJ. This result implies a potentially infinite contrast, e.g., between the p state ("1") and the ap state ("0") if the readout is performed by the bTMS effect.

The second important experimental result allows a first investigation of the dependence of the TMS effect on the relative position of the Fermi level of the electrodes. However, according to Eq. 2.22, the measured signal includes a component that linearly rises with V, as long as $\Delta R/R$ is constant with V. This correlation is valid for small bias voltages ($-20\,\mathrm{mV}$ to $20\,\mathrm{mV}$) as presented in Fig. 4.6. Hence, the Seebeck voltage $S^{\mathrm{bias}}\Delta T$ is calculated by subtracting $(\Delta R/R)V$ from the measured ΔI shown in Fig. 4.5b. This determination is based on a linear model, which is adapted to the measured $\Delta I\,(V)$ curves to deduce ΔR as the only free parameter. This model considers the measured resistance R and the current at zero bias $\Delta I\,(V=0)$. Then, the information on the variation of the Seebeck voltage $S^{\mathrm{bias}}\Delta T$ at small bias values (Fig. 4.5d) are extracted based on Eq. 2.22.

Fig. 4.6 also reveals, that the temperature dependence of the conductance is different in the p and the ap state of the MTJ, i.e., the curves for laser on/off differ much more in the ap state than in the p state. A similar observation for the temperature dependence of the resistance of Co-Fe-B/MgO/Co-Fe-B MTJs has been made by, e.g., Parkin *et al.*[10]. For extracting the Seebeck contribution from the measured ΔI signal it is crucial to take this into account. However, this is intrinsically implemented into the model (Eq. 2.22) by determining the change of resistance ($\Delta R/R$) for each state individually from the linear fit shown in Fig. 4.5b. Hence, the different values for the $S^{\mathrm{bias}}\Delta T$ in the p and ap state (Fig. 4.5d) are only attributed to the change of the Seebeck coefficients between the p and the ap state, and are not parasitic effects from the different temperature dependencies of R_{p} and R_{ap}.

Measurements with different laser powers on a second similar MTJ are presented in Fig. 4.7. More data obtained at this MTJ can be found in Appendix C.3. Fig. 4.7 displays the dependence of $S^{\mathrm{bias}}\Delta T$ that is extracted from Eq. 2.22 on the bias voltage. These measurements show that a higher laser power results in a higher Seebeck voltage. Furthermore, in the p state a nearly constant Seebeck voltage is observed when changing the bias voltage.

In the p state of the MTJ, the Seebeck contribution to the signal is constant in the interval of bias voltages between $\pm 20\,\mathrm{mV}$. However, the $S^{\mathrm{bias}}\Delta T$ in the ap state of the MTJ vary much more with the bias voltage, which causes a crossing of the p and ap voltages. For the 90 mW laser power, this crossing

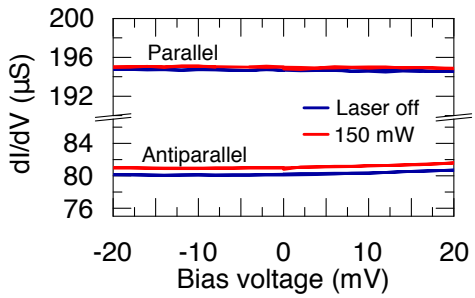

Figure 4.6. Dependence of the differential conductance dI/dV on the bias voltage for the heated (laser power 150 mW) and cold (laser blocked) MTJ: The values for the parallel (p) state and the antiparallel (ap) state have been measured at a magnetic field of 300 Oe and −70 Oe, respectively. In the small bias voltage range, the conductance is approximately constant.

is observed at −15 mV and 5 mV bias, whereas at 150 mW, the crossing is observed at −9 mV and 5 mV.

It should be noted, that the larger resistance of the ap state of the MTJ causes a higher noise level as compared to the p-state. Thus, future experiments should try to reduce the noise by, e.g., working at lower base temperatures. However, the determined Seebeck contributions $S^{\mathrm{bias}}\Delta T$ to the current signals exhibit the same geometries, as predicted by the model in Sec. 2.4.1. As discussed in Sec. 2.4.1, for this comparison it is crucial that the investigated MTJs possess a symmetric behavior with respect to the applied bias voltage. This can be seen from the constant conductance in Fig. 4.6, i.e., $dI(+V)/dV = dI(-V)/dV$. For small bias voltages the theoretical model predicts a linear behavior of ΔI, when a temperature gradient and a change in base temperature are considered (Fig. 2.10). This linear behavior is also found in the experimental data in Fig. 4.5b. If only the pure Seebeck contribution is considered, i.e., in the presence of a temperature gradient without an increase of the base temperature, the model predicts a constant value for the bias range between −20 mV to 20 mV (Fig. 2.10). The same result is exhibited by the Seebeck signal $S^{\mathrm{bias}}\Delta T$ (Figs. 4.5d and 4.7) that is extracted from the experimentally determined current signal ΔI.

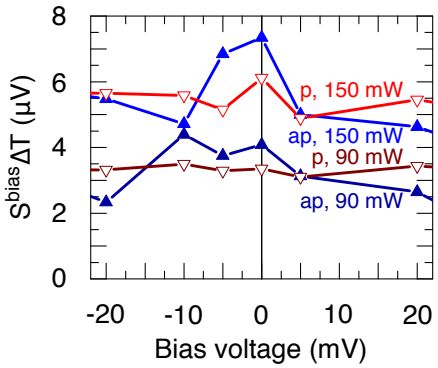

Figure 4.7. Dependence of $S^{bias}\Delta T$ on the bias voltage and heating power: Seebeck voltages that are determined according to Eq. 2.22 for different laser powers in the p and the ap states. The signal rises with increasing laser power.

This agreement is a promising evidence for the correctness of the Seebeck data that are derived from the measurements under applied bias voltage. Hence, this technique constitutes a powerful tool for future material research concerning the thermoelectric properties of MTJs.

The most important objective for future experiments is to find methods to increase the Seebeck contribution to the measured current signal. A precise determination of the Seebeck voltage under an applied bias voltage can provide a deep insight into the transport phenomena and might lead to higher TMS effects. However, this task is challenging because the generation of a temperature gradient in an MTJ unavoidably increases its base temperature. This increase in temperature affects the resistance, which is required to determine the non-Seebeck contribution (Eq. 2.16). Vice versa, the Seebeck effect always disturbs the resistance measurement of the heated MTJ. An independent determination is only possible when the temperature dependence of the resistance is determined separately. However, the temperatures of both electrodes (separated by only a nm thick tunnel barrier) cannot yet be determined.

Hence, instead of indirectly modifying the transmission by an applied bias voltage, currently, it is much more feasible to generate high TMS effects

by directly modifying the transmission of the MTJs. This can effectively be implemented by replacing the electrode material as suggested in Sec. 2.4.2. The realization of this approach is presented in the next section, by using Heusler compounds as electrode material.

4.4. High tunnel magneto-Seebeck effect in Heusler compounds

Based on their DOS it has already been revealed that half-metallic Heusler compounds in MTJs should provide high TMS effects (cf. Sec. 2.4.2). In this section the careful investigation of the TMS effect in two different Heusler compounds, Co_2FeAl and Co_2FeSi, is presented. The preparation and the composition of the layer stacks are described in detail in Sec. 3.2.2.

First, the TMS effect of $Co_2FeAl/MgO/Co_{40}Fe_{40}B_{20}$ MTJs is discussed. These MTJs are patterned on top of a 30 nm TiN buffer layer that serves as a lead to the bottom electrode. Accordingly, magnetic materials are only present in the patterned MTJs themselves. The choice of non-magnetic materials for the leads is important to entirely exclude parasitic effects originating from magneto-transport phenomena, like Nernst effects [1] or the anisotropic magneto thermopower [100], that can lead to a response of the detected voltages to an external magnetic field similar to the TMS effect. Hence, samples with a thick non-magnetic buffer are used to ensure that the detected magnetic switching is only generated in the MTJ and not elsewhere in the sample.

In the second part of this section the TMS effect obtained in $Co_2FeSi/MgO/Co_{70}Fe_{30}$ MTJs is presented. In these MTJs the Heusler compound is grown on top of a thinner 5 nm Cr layer. As the 5 nm Cr layer is too thin to provide sufficient electric contact to the bottom electrode, the magnetic Co_2FeAl is also used as bottom lead.

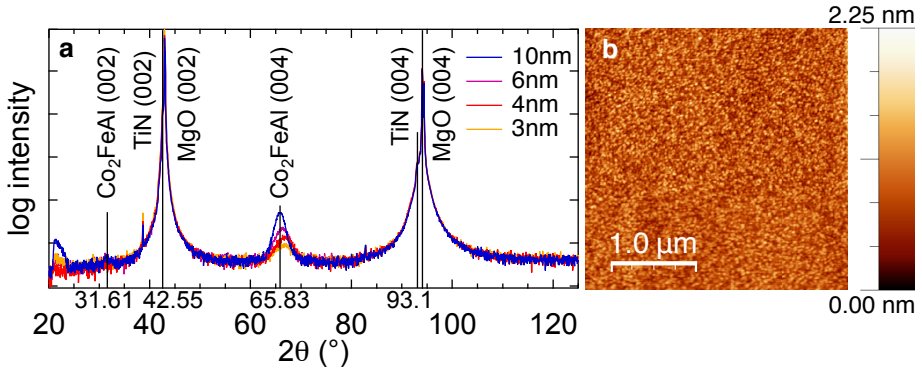

Figure 4.8. Quality of the TiN/Co_2FeAl/MgO layers: **a** X-ray diffraction data obtained from stacks with different Co_2FeAl thicknesses. The expected diffraction maxima are labeled. **b** Micrograph from an AFM analysis of the layer stack with 10 nm Co_2FeAl with a root-mean-square roughness of 0.25 nm

4.4.1. Co_2FeAl based MTJs

Sample quality

Before investigating the thermoelectric properties of the Co_2FeAl based MTJs, the quality of the TiN buffer and the adjacent Co_2FeAl is checked by XRD (cf. Sec. 3.3) and atomic force microscopy (AFM) on half MTJ layer stacks prepared in the same way as the complete MTJ stacks (Fig. 4.8). These results regarding the layer quality of the Co_2FeAl Heusler compounds evolved from a Bachelor thesis by Jana Ludwig [101].

The XRD scans of TiN 30 nm/Co_2FeAl/MgO 2 nm with different Co_2FeAl thicknesses from 3 nm to 10 nm (Fig. 4.8a) unveil that the TiN posseses nearly the same lattice constant as the MgO substrate, since it is only visible as a small shoulder in the MgO peak. The derived lattice constant for the TiN is (4.25 ± 0.10) Å, which is in good agreement with the literature value of 4.24 Å [102]. The XRD results also suggest that a 10 nm Co_2FeAl layer is the optimum choice for the MTJ stacks, as for this thickness the Co_2FeAl (004) peak perfectly matches the expected value of 65.83°. For the Co_2FeAl, a B2 ordering is found by detecting the (222) and (444) peaks, while a (111)

peak, indicating $L2_1$ ordered Co_2FeAl, is absent[103]. The B2 ordering results in a less pronounced and shifted gap in the DOS with respect to the chemical potential (cf. Sec. 2.4.2 Fig. 2.14).

Furthermore, the micrograph obtained by the AFM investigations (Fig. 4.8b) reveals a low root-mean-square roughness of 0.25 nm for the TiN 30 nm/ Co_2FeAl 10 nm/MgO 2 nm layers. This low roughness value is crucial for MTJs with a tunnel barrier of high quality to avoid electrical shorting between the two electrodes through pinholes.

Switching behavior and temporal evolution

After determining the good sample quality of the layers for the Co_2FeAl based MTJs, the electric and thermoelectric transport properties of Co_2FeAl based MTJs are investigated. Fig. 4.9a displays the Seebeck voltage of an elliptically shaped $3\,\mu m \times 1\,\mu m$ sized Co_2FeAl based MTJ under 150 mW laser power at a laser modulation frequency (on/off) of 13 Hz. As the spot diameter of the laser on top of the MTJ is $\approx 10\,\mu m$, a homogeneous illumination of the MTJ is ensured. A sharp switching of the Seebeck voltage between $-216\,\mu V$ in the p and $-434\,\mu V$ in the ap state of the MTJ is observed. This yields a TMS ratio of $-101\,\%$ (see Eq. 2.5). It is noteworthy, that the Seebeck voltage of the Co_2FeAl based MTJs is negative, which is different from the Co-Fe-B MTJs observed by Walter *et al.*[4], Liebing *et al.*[5], and Boehnke *et al.*[17]. Furthermore, the generated Seebeck voltages are much higher, than for the Co-Fe-B based MTJs studied with the same laser setup[4,17,18] and presented in Sec. 4.1. A more detailed comparison of Heusler compound and Co-Fe-B based MTJs is given later (Sec. 4.4.3).

The Seebeck coefficients are calculated from the simulated temperature difference across the MgO barrier of 390 mK (cf. Sec. 4.2.1) and the experimentally determined voltages at a laser power of 150 mW. Seebeck coefficients of $S_p = 554\,\mu V\,K^{-1}$ and $S_{ap} = 1113\,\mu V\,K^{-1}$ are obtained for the p and the ap state, respectively.

The abrupt changes of the Seebeck voltage occur at the same field values and with the same shape as the switching of the resistance of the MTJ. The similarities are nicely seen when the resistance data is plotted on top of the Seebeck voltage (Fig. 4.9a). The resistance, obtained at 10 mV bias

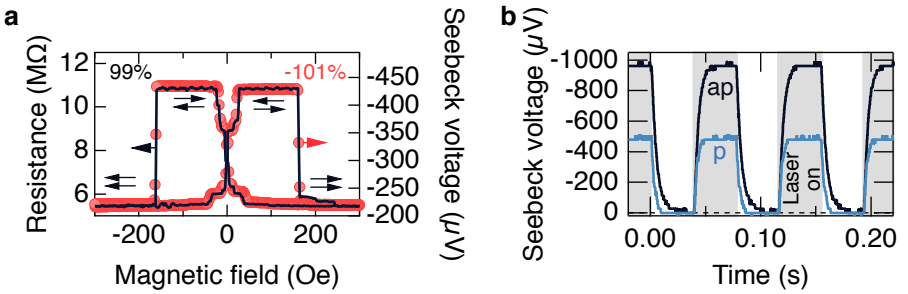

Figure 4.9. Seebeck voltage of a Co_2FeAl based MTJ: a The resistance (left axis) and the Seebeck voltage (right axis) switch at the same fields, i.e., when the magnetic orientation of the ferromagnetic layers changes between p and ap. **b** Temporal evolution of the Seebeck voltage between laser on/off in the p and ap state.

voltage, changes between 5.45 MΩ in the p state and 10.87 MΩ in the ap state, yielding a TMR ratio of 99 % (see. Eq. 2.1).

The similar switching behaviors of the resistance and the Seebeck voltage are first evidences that the reversal of the magnetic orientation of the ferromagnetic electrodes causes the change of the Seebeck voltage. Of course, the fundamental origin is the change of the transport coefficients of the MTJ under magnetization reversal (see Sec. 2.3.3).

Since a modulated heating source in combination with high-resistive MTJs is used, it is crucial to monitor the temporal evolution of the signal. For the correct detection of the Seebeck voltage by the lock-in amplifier, it is highly important that the Seebeck signal saturates after the laser has been switched on or off. During laser on the voltage has to reach a constant plateau, whereas during laser off it should drop back to zero. The rise and fall times of the signal are dependent on the resistance and capacitance of the MTJ[17]; the higher the resistance, the slower is the saturation. Fig. 4.9b displays oscilloscope traces of the Seebeck signal that reveal a saturation of the voltage in the p state after 10 ms and in the ap state after 15 ms when the laser is switched on or off. The increased saturation time in the ap state is attributed to the increased resistance. Accordingly, the modulation of the

laser heating with 13 Hz, corresponding to a laser on period of ≈ 38 ms, is slow enough to allow a correct lock-in detection. The higher values of the voltages detected by the scope compared to the lock-in amplifier are due to the difference in the detection techniques. The scope displays the peak-to-peak voltages, whereas the lock-in amplifier displays the root-mean-square value of the first harmonic of the signal (cf. Sec. 3.1.5). For a conversion to the lock-in-signal, the oscilloscope signal has to be multiplied by a factor of 0.45 (Eq. 3.4). As the oscilloscope traces are recorded in the p and ap state of the MTJ, the temporal traces also disclose the difference of the Seebeck voltage between the magnetic states of the MTJ. The TMS ratio obtained from this difference amounts to ≈ −100 %. Hence, it is nearly of the same size as the TMS ratio obtained from the lock-in measurements in Fig. 4.9a. This good agreement is another proof for the reliability of the correct voltage detection by the lock-in technique.

Power dependence of the tunnel magneto-Seebeck effect

After having received a first impression on the capability of Co_2FeAl based MTJs for providing high Seebeck voltages in combination with large TMS ratios, it has to be proven that the switching and effect size are reproducible. Therefore, the Seebeck voltage is recorded at different laser powers for a second smaller elliptical shaped MTJ of $2\,\mu m \times 1\,\mu m$. The results in Fig. 4.10a emphasize the pristine and reliable switching of the Seebeck voltages between the p and the ap state even down to low heating powers of 10 mW. For zero heating power the signal vanishes due to the absence of a temperature gradient.

In Fig. 4.10c the Seebeck voltages of the MTJ in the p and ap states are displayed for different laser heating powers. The absolute values of the voltages increase linearly with rising laser power from zero to almost $-450\,\mu V$ in the ap state. For 150 mW laser power $V_p = -227\,\mu V$ and $V_{ap} = -442\,\mu V$ are recorded. From these values, the Seebeck coefficients are calculated to $S_p = 582\,\mu V\,K^{-1}$ and $S_{ap} = 1133\,\mu V\,K^{-1}$. This is in the same range as for the first MTJ. The TMS ratios for different heating powers remain nearly constant at approximately −93 %, proving a consistent and reliable readout of the TMS ratio, even under changing heating conditions.

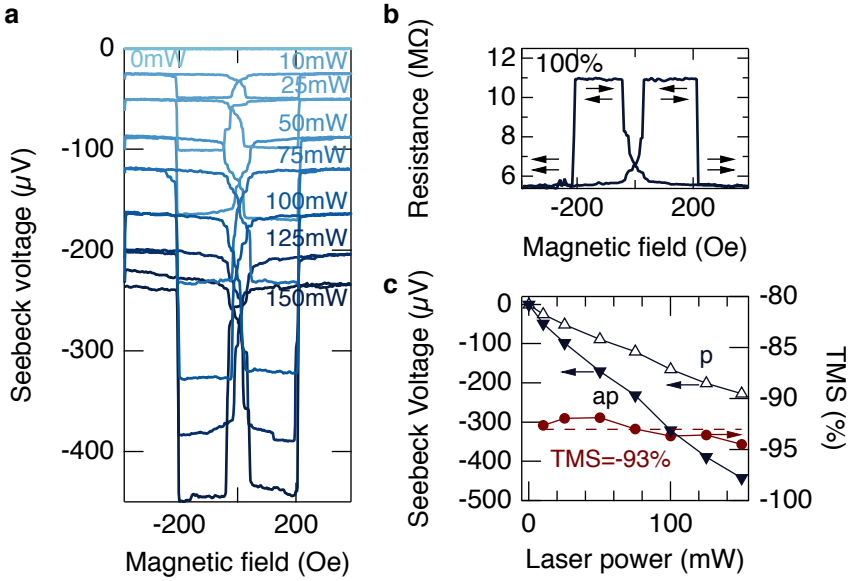

Figure 4.10. Tunnel magneto-Seebeck effect of Co_2FeAl based MTJs: a Dependence of the Seebeck voltage on the magnetic field. **b** Tunnel magnetoresistance. The arrows indicate the magnetic orientation of the ferromagnetic layers. **c** Dependence of the voltage in the p and ap state, and TMS ratio derived from these voltages.

The resistances of this second MTJ (Fig. 4.10b) switch between $R_p = 5.5\,\mathrm{M\Omega}$ and $R_{ap} = 11.0\,\mathrm{M\Omega}$ yielding a TMR ratio of 100 % which is well comparable to the previous MTJ (Fig. 4.9). The power dependence of the previously investigated MTJ is presented in Appendix D.1 and reveals similarly high voltages and TMS ratios.

Contributions from the leads: MTJ after dielectric breakdown

To ensure that the Seebeck voltage is indeed generated by the temperature gradient across the MTJ and not, for example, in the leads, the junction is forced into a dielectric breakdown and the remaining Seebeck voltage is determined (Fig. 4.11). To break the 2 nm tunnel barrier, a bias voltage of 4 V

is applied to the MTJ. The broken tunnel junction disables the spin-dependent tunnelling across the barrier. Hence, the TMR effect in the broken junction vanishes and the resistance drops from a few MΩ to 436 Ω (Fig. 4.11b). A voltage is still detected under laser irradiation, but the characteristic bow tie shape of the Seebeck voltage versus magnetic field curves disappears for the broken MTJ (Fig. 4.11a). The remaining Seebeck voltage still increases with applied laser power, but instead of negative, positive and thirty times smaller voltages are obtained. Although, the bow tie shaped response of the signal to the magnetic field is not visible any more, a barely visible hysteresis curve is detected. Looking at the saturation values of these hysteresis curves, an averaged upper limit for the effect size of 2 % is determine in the broken MTJ (Fig. 4.11c), in contrast to approximately −100 % in the MTJ with an intact tunnel barrier. The origin of this hysteresis is not fully clarifyied, but most likely it is generated by Nernst effects in the ferromagnetic electrodes. It can neither originate from the leads, since these are non-magnetic, nor can it be generated in the substrate, as reported for silicon [17,22], because insulating MgO is used.

The difference in the shape of the voltage versus magnetic field curves, the opposite sign of the voltage, and the strongly decreased size of the effect ratio after breakdown of the junction point out that the high TMS ratios are generated solely by the thermoelectric transport between the Co_2FeAl and the Co-Fe-B across the intact tunnel barrier.

Heating at different distances from the MTJ

Although, the TMS ratios for different heating powers remain unchanged (Fig. 4.10c), moving the laser spot away from the top of the MTJ, i.e., generating an inhomogeneous temperature gradient across the tunnel barrier, affects the generated Seebeck voltages and TMS ratios (Fig. 4.12). A decrease of the Seebeck voltage is observed when the distance between the MTJ is increased. The decline of the Seebeck voltage is directly related to the reduced temperature gradient across the barrier for increased distances. The Seebeck voltage versus magnetic field curves keep the characteristic bow tie shape. Thus, a TMS effect is expected, although the MTJ is not directly illuminated. Fig. 4.12b unveils that the TMS ratio remains at relatively high

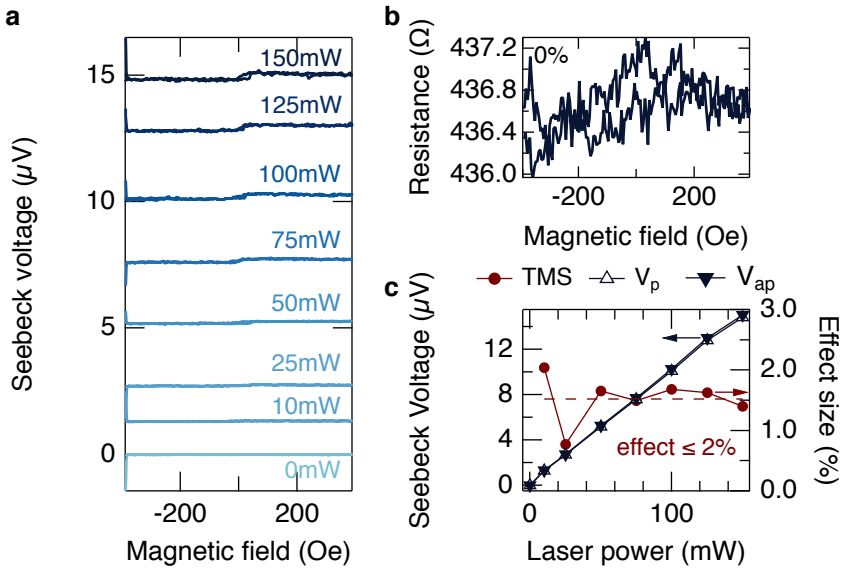

Figure 4.11. Co_2FeAl based MTJs after dielectric breakdown:a Dependence of the Seebeck voltage for different laser powers, and **b** the resistance on the magnetic field. **c** Dependence of the Seebeck voltage in the p and ap state (left axis), and the effect ratio (right axis) on the laser power.

values of above −80 %, even though the distance between the MTJ and the lasers spot exceeds 500 µm. Only for the data recorded with the laser spot positioned at a distance of 1800 µm a significant decrease of the TMS ratio is observed and the bow tie shape of the Seebeck voltage versus magnetic field curves in Fig. 4.12a vanishes.

The detection of a TMS effect in the Co_2FeAl based MTJs, even if the laser is moved relatively far away from the MTJ, can only be explained by a temperature gradient remaining across the MgO barrier. The two major justifications for this assumption are the presence of magnetic material only in the MTJ itself and the vanishing of the bow tie shaped Seebeck voltage versus magnetic field curves after the dielectric breakdown of the MTJ. Taking these two results into account, no other source of the magnetic switching of the voltage can be determined than the MTJ itself. However,

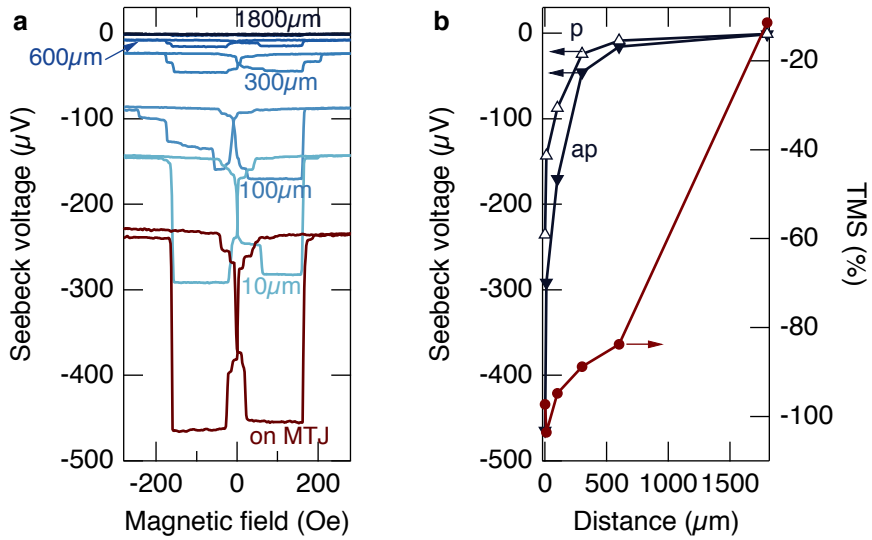

Figure 4.12. Seebeck voltage and TMS effect for different positions of the laser spot: a Switching of the Seebeck voltage when the laser spot is moved away from the top of the MTJ. **b** Seebeck voltage in the p and ap state of the MTJ and corresponding TMS ratio for different distances between the laser spot and the MTJ.

it has to be emphasized, that a reliable determination of the thermoelectric transport in an MTJ is only guaranteed when the MTJ is homogeneously heated across the barrier. For laser experiments this requires an irradiation with a laser spot larger than the MTJ and focused on top of a transducer layer directly above the MTJ. A direct illumination of the functional MTJ layers, e.g., the ferromagnetic electrodes, or an illumination of the leads is not advisable, since it will most likely not probe the correct Seebeck contribution of the MTJ, as revealed by the distance dependence of the Seebeck voltage in Fig. 4.12.

The Seebeck current

Besides the Seebeck voltage, also the Seebeck current of the MTJ is determined. Derived from Eq. 2.6, the current in such a measurement is expressed by

$$I_{\mathrm{p,ap}} = \frac{1}{R_{\mathrm{p,ap}}} S_{\mathrm{p,ap}} \Delta T = \frac{1}{R_{\mathrm{p,ap}}} (-V_{\mathrm{p,ap}}^{\mathrm{Seebeck}}) \tag{4.1}$$

$$\Leftrightarrow R_{\mathrm{p,ap}} = -\frac{\left(V_{\mathrm{p,ap}}^{\mathrm{Seebeck}}\right)}{I_{\mathrm{p,ap}}}. \tag{4.2}$$

This equations reveal that the Seebeck current depends on the change of the Seebeck coefficients $S_{\mathrm{p,ap}}$ and the resistance $R_{\mathrm{p,ap}}$ between the p and ap state of the MTJ. After inserting Eq. 2.7 it resembles Ohm's law (Eq. 4.2). Thus, the resistance of the MTJ is recalculated from the independently recorded Seebeck voltage and Seebeck current data.

Fig. 4.13a depicts the Seebeck current obtained from an elliptical MTJ with diameters of $3\,\mu\mathrm{m} \times 1\,\mu\mathrm{m}$ at 100 mW laser power. The current is switching between 36.6 pA in the p and 39.3 pA in the ap state, resulting in an effect ratio of approximately 7 %. The Seebeck voltage determined at the same MTJ without altering the laser irradiation is displayed in Fig. 4.13b. It changes between $-83\,\mu\mathrm{V}$ in the p state and $-176\,\mu\mathrm{V}$ in the ap state of the MTJ, yielding a TMS ratio of $-112\,\%$. Recalculating the resistance from the Seebeck current and the Seebeck voltage data in Fig. 4.13a and b, results in a curve that almost perfectly fits the measured resistance displayed in Fig. 4.13c.

A similar agreement of the recalculated and measured resistance is also achieved for Seebeck measurements with 150 mW laser power and on a second similarly shaped MTJ with resistances $R_{\mathrm{p}} = 5.4\,\mathrm{M\Omega}$ and $R_{\mathrm{ap}} = 10.8\,\mathrm{M\Omega}$. This MTJ reveals a TMR ratio of 100 % and a TMS ratio of $-97\,\%$.

As the resistance is correctly recalculated from the Seebeck voltage and current, two conclusions are drawn: First, the Seebeck voltage and current detection of the MTJ are very reliable and reproducible. Independent measurements lead to similar results. Second, Eq. 2.6 correctly describes the thermoelectric transport in the Co_2FeAl based MTJs.

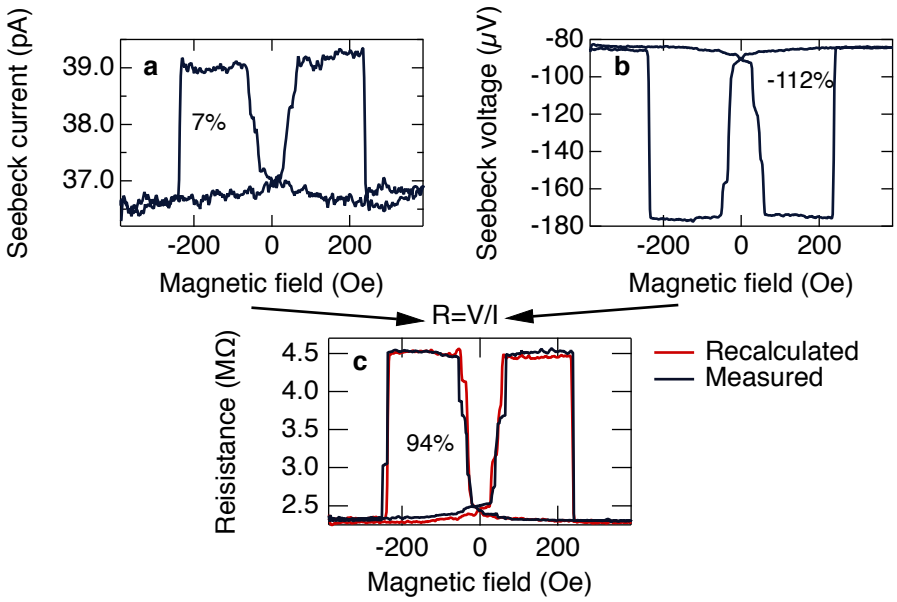

Figure 4.13. Seebeck current of Co_2FeAl based MTJ: a Seebeck current recorded at 150 mW laser power. **b** Seebeck voltage of the same MTJ under unchanged irradiation conditions. **c** Directly measured resistance at 10 mV bias voltage and recalculated resistance from Seebeck data in a and b.

Does Co_2FeAl perform better than Co-Fe-B?

Finally, the initial question, if Co_2FeAl based MTJs are advantageous for high TMS effects can be approached. For this purpose a Co_2FeAl based MTJ is compared to a $Co_{26}Fe_{54}B_{20}$/MgO (1.7 nm)/$Co_{26}Fe_{54}B_{20}$ MTJ. Both MTJs possess an elliptical shape and diameters of $2\,\mu m \times 1\,\mu m$.

For highlighting the advantages and disadvantages of each MTJ, the TMR and TMS effect ratios of the Co-Fe-B based MTJ with resistances of $R_p = 66\,k\Omega$ and $R_{ap} = 211\,k\Omega$ are directly compared to the Co_2FeAl based MTJ with $R_p = 5.45\,M\Omega$ and $R_{ap} = 10.87\,M\Omega$ (cf. Fig. 4.10). Fig. 4.14 clearly reveals that the TMR ratio of the Co-Fe-B based MTJ is nearly twice as high as the TMR ratio of the Co_2FeAl based MTJ. The higher TMR ratio of the Co-

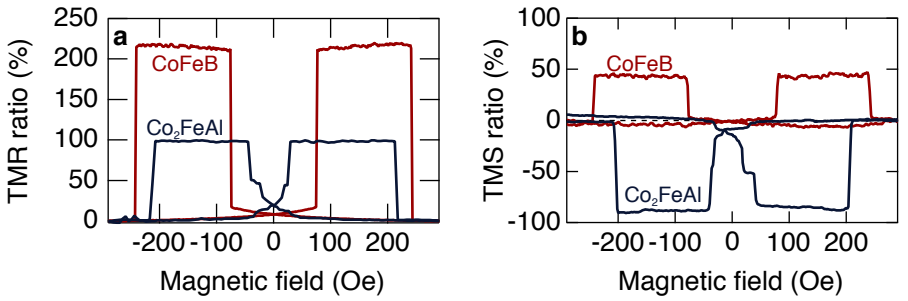

Figure 4.14. Comparison of CoFeB and Co_2FeAl based MTJs: Although, the TMR ratio **a** of CoFeB based MTJs is nearly twice as high as the TMR ratio of Co_2FeAl based MTJs, the TMS ratio **b** of Co_2FeAl is two times the TMS ratio of CoFeB. Furthermore, the TMS ratios have opposing sign.

Fe-B based MTJ has been expected, because currently Co-Fe-B/MgO/Co-Fe-B MTJs set the benchmark for the TMR effect.

Surprisingly, this relation is reversed when the TMS ratio is investigated. The TMS ratio of the Co-Fe-B based MTJ does not exceed 50 % whereas the TMS ratio of the Co_2FeAl based MTJ reaches -90 %. Not only does the absolute value of the TMS ratio nearly double when replacing one Co-Fe-B electrode by Co_2FeAl, but so does the sign of the TMS ratio change. The sign change is explained by considering the sign of the Seebeck voltages determined at both MTJs with 150 mW laser power. For the MTJ containing Co-Fe-B, the Seebeck voltages switch between $V_p = 6.4\,\mu V$ and $V_{ap} = 9.1\,\mu V$, whereas for Co_2FeAl based MTJs the voltages are much higher and possess negative signs, i.e., $V_p = -234\,\mu V$ and $V_{ap} = -450\,\mu V$.

4.4.2. Co_2FeSi based MTJs

The second Heusler compound that promises to provide high TMS effects is Co_2FeSi. $L2_1$ ordered Co_2FeSi and B2 ordered Co_2FeAl have a comparable DOS with respect to the relative position of the chemical potential to the gap in the minority DOS (Sec. 2.4.2). Hence, similar results for the amplitude and sign of the gained Seebeck voltages are expected. Furthermore, also

a high TMS ratio is predicted, because of the nearly half-metallic DOS of the Co_2FeSi. However, before the determined voltage signals can definitely be attributed to the TMS effect, the crystalline structure of the Heusler compound film, the switching behavior of the MTJs, the lead contributions, and the reproducibility of the obtained TMS ratios for different laser powers have to be checked. Therefore, the same investigations as for the Co_2FeAl based MTJs (Sec. 4.4.1) are conducted.

Sample quality

The sample quality has been carefully investigated and optimized by Sterwerf *et al.* [65,75]. In the XRD analysis of the Co_2FeSi layers they find a narrow and well pronounced Heusler (004) peak at $2\theta = 67°$ and the (002) peak at 32°. From these peaks they were able to determine a lattice parameter of 5.64 Å, which is equal to the bulk lattice parameter [104]. From the ratio of the (002) and the (004) peak, as well as from analyzing the (111) peak they can determine, that the Co_2FeSi in these samples mainly crystallizes in the $L2_1$ ordering.

Furthermore, they examined the TMR ratio in dependence on the post annealing temperature. In their investigations the highest TMR ratio of 118 % for the Co_2FeSi based MTJs could be achieved at 325 °C. Accordingly, this is the annealing temperature that is used for the samples prepared for the following investigations (cf. Sec. 3.2.2).

Switching behavior and temporal evolution

The Co_2FeSi MTJs are equipped with an antiferromagnetically pinned top Co-Fe electrode (cf. Sec. 3.2.2). The pinning prevents the Co-Fe electrode from switching at low external magnetic fields. The higher fields needed to reverse the magnetization of the pinned layer exceed the field provided by the electromagnet in the TMS setup. Hence, it is only possible to record minor loops of the MTJs, i.e., reversing the magnetization of the unpinned Co_2FeSi bottom electrode while keeping the magnetization of the CoFe electrode constant, and receive a signal that resembles the hysteresis loop of this layer.

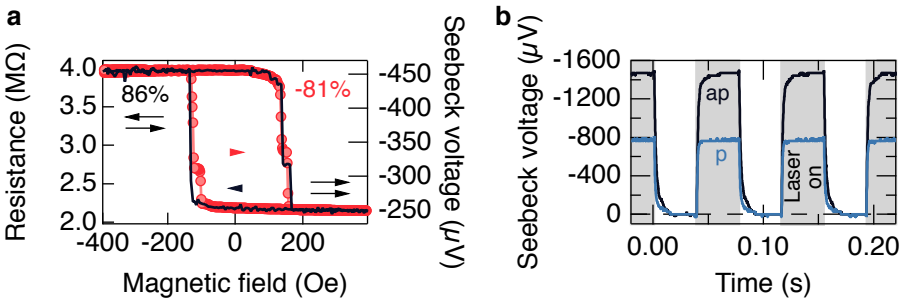

Figure 4.15. Seeebeck voltage of a Co_2FeSi based MTJ: a The resistance (left axis) at 10 mV bias voltage and the Seebeck voltage (right axis) at 150 mW laser irradiation switch at the same magnetic fields, i.e., when the magnetization of the Co_2FeSi layer is reversed. **b** Temporal evolution of the Seebeck voltage at 150 mW laser power between laser on/off at a modulation frequency of 13 Hz.

The TMR and TMS loops of an elliptical 2 µm × 1 µm Co_2FeSi based MTJ with a 2 nm MgO tunnel barrier and a $Co_{70}Fe_{30}$ counter electrode are displayed in Fig. 4.15a. The switching of the resistance between 4.00 MΩ in the ap state and 2.15 MΩ in the p state is clearly visible. The resulting TMR ratio amounts to 86 %. The Seebeck voltage obtained at the same MTJ with 150 mW laser power exhibits a similar switching behavior as the resistance. It changes at the same fields between −664 µV in the ap state and −370 µV in the p state. This change yields a TMS ratio of −80 %. Hence, the ratio is only slightly smaller than the values obtained for the Co_2FeAl based MTJs investigated in Sec. 4.4.1.

Fig. 4.15b features the temporal evolution of the Seebeck signal under 150 mW laser radiation with an on/off modulation at a frequency of 13 Hz. The obtained TMS ratio is −92 %, which is slightly higher than the value obtained by the lock-in measurement. The peak-to-peak voltages of $\hat{V}_p = -1471\,\mu V$ and $\hat{V}_{ap} = -763\,\mu V$ correspond to root-mean-square voltages of the first harmonic detected by the lock-in-amplifier of $V_p = -661\,\mu V$ and $V_{ap} = -343\,\mu V$. These values are in a similar range as the experimentally obtained lock-in data. Furthermore, the temporal evolution of the Seebeck voltage obtained at the Co_2FeSi based MTJs reveals that the modulation

Table 4.1. Overview of Co_2FeSi based MTJs: The MTJ with the higher resistance-area product exhibits higher TMR and TMS ratios. The resistance is determined at a bias voltage of 10 mV. The Seebeck voltages are recorded with 150 mW laser power and a spot diameter of $\approx 10\,\mu m$. The TMS ratios are averaged over Seebeck measurements with laser powers between 10 mW to 150 mW.

MTJ	size ($\mu m \times \mu m$)	R_pA ($M\Omega\,\mu m^2$)	$R_{ap}A$ ($M\Omega\,\mu m^2$)	**TMR**	V_p (μV)	V_{ap} (μV)	**TMS**
a	2×1	3.36	6.28	86 %	−370	−664	−83 %
b	3×1	3.93	7.94	102 %	−263	−503	−95 %

frequency of 13 Hz is slow enough for the Seebeck voltage to reach saturation after the laser is switched on or off. In the p state the increase and decrease of the signal is faster ($\tau^{p}_{1/2} \approx 0.6\,ms$[1]) than in the ap state ($\tau^{ap}_{1/2} \approx 1.1\,ms$) of the MTJ, due to the decreased resistance of the MTJ in the p state.

A similar switching of the Seebeck voltage under varying magnetic field is found for a second elliptical MTJ with a size of $3\,\mu m \times 1\,\mu m$ (see Appendix D.2). For this MTJ (MTJ b) the TMS ratio reaches an average of −95 %, which is higher than for the previously described MTJ (MTJ a), where the ratio only yields an average of −83 % (Tab. 4.1). A difference is also spotted, if the TMR ratios of the two MTJs are compared. MTJ b has a TMR ratio of 102 % whereas MTJ a only produces a TMR ratio of 86 %. This observation suggests, that the difference of the TMS ratios is purely based on the less pronounced change of the transport coefficients, i.e., the conductance and the Seebeck coefficient, in MTJ a. Such a behavior is usually evoked by a local variation of the quality of the tunnel barrier. This assumption is supported by the fact that the resistance-area product is decreased for the MTJ with the lower TMR and TMS ratios, indicating the poorer quality of the MgO barrier in MTJ a.

The Seebeck coefficients for MTJ a (cf. Fig. 4.15 and Tab. 4.1) are $S_p = 948\,\mu V\,K^{-1}$ and $S_{ap} = 1703\,\mu V\,K^{-1}$. For MTJ b the values still reach up to

[1] 0 % to 50 % rise time of the signal when the heating is switched on. The 0 % to 90 % rise times are $\tau^{p}_{90\,\%} \approx 1.6\,ms$ and $\tau^{ap}_{90\,\%} \approx 3.6\,ms$

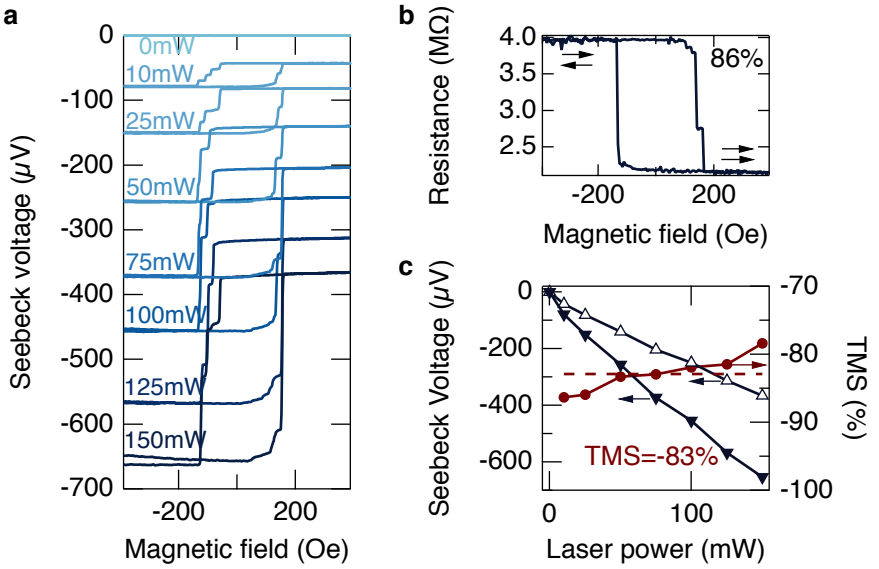

Figure 4.16. Tunnel magneto-Seebeck effect of Co_2FeSi based MTJs: The MTJ has a size of $2\,\mu m \times 1\,\mu m$. **a** Dependence of the Seebeck voltage on the magnetic field. **b** Tunnel magnetoresistance. The arrows indicate the magnetic orientation of the ferromagnetic layers. **c** Dependence of the voltage in the p and ap state, and TMS ratio derived from these voltages.

$S_p = 674\,\mu V\,K^{-1}$ and $S_{ap} = 1290\,\mu V\,K^{-1}$. These values are even higher than for the Co_2FeAl based MTJs.

Power dependence of the tunnel magneto-Seebeck effect

Since it is ensured that the switching of the Seebeck voltage is fully attributed to the change of the magnetic orientation of the ferromagnetic layers, the stability of the switching and the TMS ratios for various laser powers is studied. For this investigation data obtained from MTJ a are used.

Fig. 4.16a indeed exhibits a switching of the Seebeck voltage for all laser powers between 10 mW to 150 mW with an average TMS ratio of −83 %. The curves of the Seebeck voltage resemble the switching of the resistance

in Fig. 4.16b, as already seen in Fig. 4.15. For 0 mW laser power, i.e., the heating switched off, a Seebeck signal is not detected, since no temperature gradient exists across the barrier. The absolute Seebeck voltages increase linearly with rising laser power (Fig. 4.16c). However, the TMS ratio is not constant, but the absolute value decreases slightly for higher laser powers from nearly −90 % at 10 mW to −79 % for 150 mW. A similar decrease is found in a second MTJ (see Appendix D.2).

Most likely, this decrease is a first indication of the temperature dependence of the Seebeck coefficients. When the laser power is increased not only the temperature gradient across the barrier, but also the base temperature of the MTJ rises. Both changes influence the thermoelectric transport across the tunnel barrier. However, in the available setup it is not possible to externally control the base temperature of the MTJ, and, hence, a more systematic investigation of the temperature dependence of the TMS effect is pending.

Contributions from the leads: MTJ after dielectric breakdown

To further ensure that the detected switching of the Seebeck voltage is only generated by the MTJ and not by other parts of the sample, e.g., the ferromagnetic bottom lead, the barrier of the MTJ is forced into a dielectric breakdown. In the broken MTJ, the spin-polarized tunnelling between the ferromagnetic electrodes is impossible, and the remaining signal has to be generated by a different mechanism, e.g., by a Seebeck effect in the leads. This is the most probable origin of the small voltages displayed in Fig. 4.17a.

The low resistance of the MTJ after breakdown (Fig. 4.17b) clearly exhibits that the tunnel barrier has been destroyed. A response of the resistance to the reversal of the magnetization of the ferromagnetic electrodes is no longer visible.

A similar behavior is found for the Seebeck voltage that exhibits almost no response to the external magnetic field. Only for higher laser powers, i.e., higher Seebeck voltages, a hysteresis loop is distinguished from the noise. The origin of the remaining switching might be due to magneto transport phenomena in the ferromagnetic Co_2FeSi bottom lead. The barely visible change of the detected voltage generates an averaged effect of −1 % and, hence, is much smaller compared to the intact MTJ (cf. Fig. 4.16).

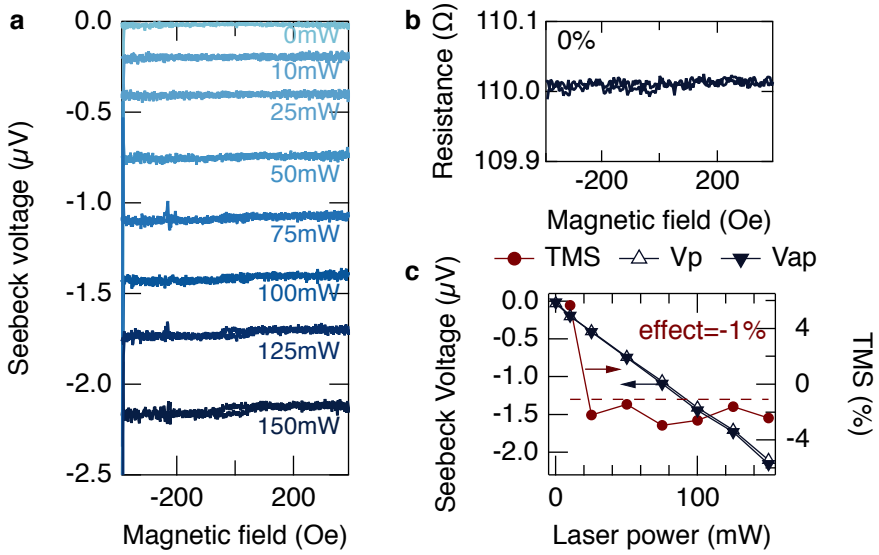

Figure 4.17. Co_2FeSi based MTJs after dielectric breakdown: a Dependence of the Seebeck voltage for different laser powers, and **b** the resistance on the magnetic field. **c** Dependence of the Seebeck voltage in the p and ap state (left axis), and the effect ratio (right axis) on the laser power.

Since the MTJ reveals nearly no switching after the tunnel barrier is forced into a dielectric breakdown, it is guaranteed that the leads do not significantly contribute to the high TMS ratio obtained from the intact MTJ. The high Seebeck voltages and TMS ratios are only generated due to the temperature difference across the MgO barrier.

Heating at different distances from the MTJ

In the last section it has already been found that the high Seebeck voltage is generated by the MTJ and not by the leads or any other material surrounding it. Accordingly, the voltage should decrease when the distance between the MTJ and the laser spot is increased. Fig. 4.18 exactly reveals this behavior. However, for a distance of 300 µm, which is 30 times the laser spot diameter,

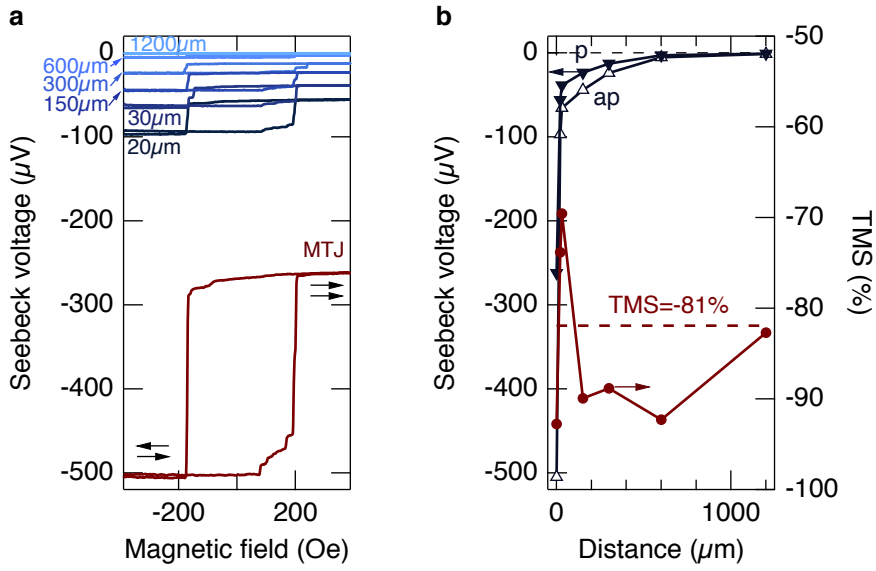

Figure 4.18. TMS effect of a Co_2FeSi based MTJ for different positions of the laser spot: a Switching of the Seebeck voltage when the laser spot is moved away from the top of the MTJ. **b** Seebeck voltages in the p and ap state of the MTJ and corresponding TMS ratios for different distances between the laser spot and the MTJ.

the detected voltage still reaches more than −20 µV. Furthermore, the switching of the MTJ remains visible and the TMS ratio, even for a distance of 1200 µm, remains at a high value of more than −80 %.

These experiments show the same characteristics as found in Co_2FeAl based MTJs (Sec. 4.4.1), and thus confirm the previous results; First, a reliable measurement of the Seebeck voltage is only obtained, when the MTJ is fully irradiated from the top. Second, even if the laser spot is moved away from a centered position on top of the MTJ, a temperature gradient across the tunnel barrier remains. This gradient is much smaller, as seen from the decreased Seebeck voltages, but yet large enough to generate a detectable TMS effect.

In conclusion of these findings, the temperature gradient across the tunnel barrier is by far the most probable origin of the detected voltages, even at

larger distances. The reasons, why other effects are most unlikely, are the decrease of the Seebeck voltage when the laser is moved away from the MTJ, and the disappearance of any switching when the MTJ is destroyed. However, since these Co_2FeSi based MTJs contain a ferromagnetic bottom lead, other magneto-transport effects cannot be fully excluded as this has been the case for the Co_2FeAl based MTJs that had non-magnetic leads.

The Seebeck current

Similar to the experiments performed with Co_2FeAl based MTJs in Sec. 4.4.1, the Seebeck current of the MTJ is determined and the resistance is recalculated by dividing the Seebeck current by the Seebeck voltage. These values are obtained from independent measurements at the same MTJ under unchanged irradiation conditions.

Fig. 4.19a displays the switching of the Seebeck current of MTJ a in Tab. 4.1 (elliptical shape of $2\,\mu m \times 1\,\mu m$). The current resembles the same switching behavior as the resistance and the Seebeck voltage (Fig. 4.19b). However, the effect ratio only yields 1 %. This is attributed to the similar sizes of the TMR and TMS ratios. According to $I = S/R \cdot \Delta T$ (cf. Eq. 2.7), the switching of the Seebeck coefficient S and the resistance R cancel out when the two effects are of similar magnitudes.

Fig. 4.19c displays the resistance of the MTJ under varying magnetic field. As before, the difference between the p and ap state of the MTJ is clearly recognizable. Furthermore, the curve of the recalculated resistance from the Seebeck data lies on top of the directly measured resistance, except of a small offset. Since both approaches, directly measuring the resistance and recalculating the resistance from the Seebeck data, lead to similar results, this proves that the linearized Landauer-Büttiker formalism (Eq. 2.7) also correctly describes the transport through the Co_2FeSi based MTJs.

Does Co_2FeSi perform better than Co-Fe-B?

In the course of this section it was already seen that the Co_2FeSi based MTJs exhibit high Seebeck voltages and high TMS ratios. Still it has to be proven that these MTJs perform better than the wide spread and commonly used

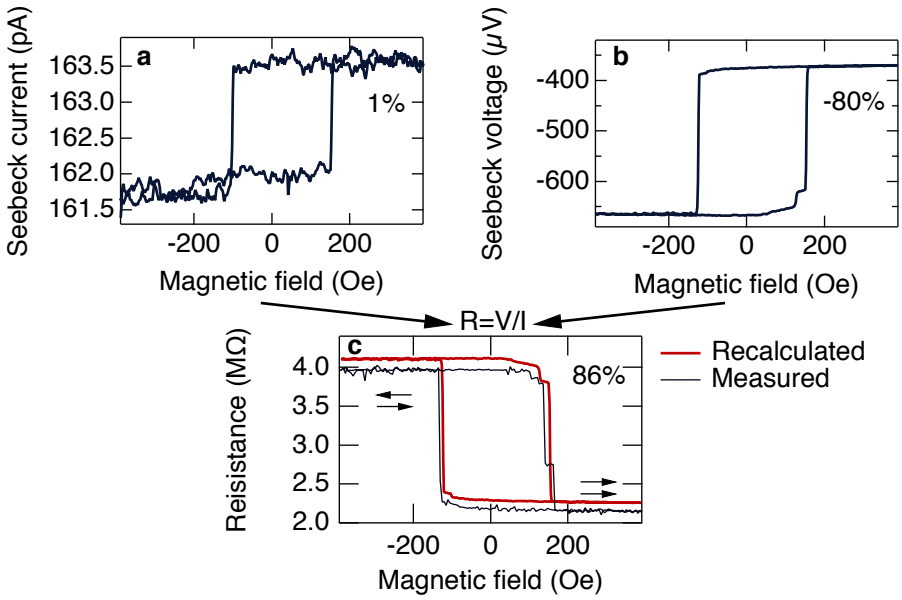

Figure 4.19. Seebeck current of Co_2FeAl base MTJ: a Seebeck current recorded at 150 mW. **b** Seebeck voltage of the same MTJ under unchanged irradiation conditions. **c** Directly measured resistance at 10 mV bias voltage and recalculated resistance from Seebeck data in a and b.

Co-Fe-B/MgO/Co-Fe-B MTJs. For obtaining direct comparison, the TMR and TMS effects are evaluated in an antiferromagnetically pinned Co-Fe-B and a Co_2FeAl based MTJ with a similar TMR ratio of about 80 % (Fig. 4.20a). The exact layer stack of the Co-Fe-B based MTJ is Ta 5/Ru 30/Ta 10/MnIr 12/CoFe 23/Ru 0.9/$Co_{40}Fe_{40}B_{20}$ 3/MgO 1.5/$Co_{40}Fe_{40}B_{20}$ 3/NiFe 6/Ta 3/Ru 3/Ta 3 (numbers are thickness in nm). The stack is *ex-situ* annealed at 350 °C for 1 h and field-cooled in an external magnetic field of 7 kOe. Afterwards, it is patterned into MTJs of elliptical shape with diameters of 6 µm × 4 µm and insulated by Ta_2O_5. For optical and electric access the MTJs are equipped with Ta 5/Au 60 contact pads. The Co-Fe-B based MTJ used to obtain the data in Fig. 4.20 has resistances of $R_p = 860\,\Omega$ and $R_{ap} = 1570\,\Omega$.

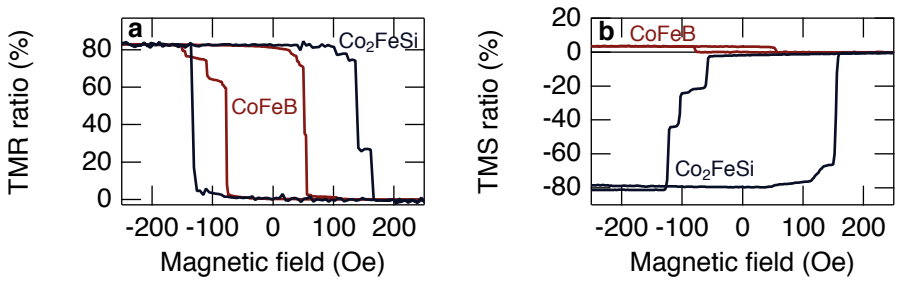

Figure 4.20. Comparison of Co_2FeSi and $Co_{40}Fe_{40}B_{20}$ based MTJs: a A pinned Co-Fe-B and Co_2FeSi MTJ with similar TMR ratios. **b** The TMS ratios of the same MTJs differ by a factor of ≈ 20 and have opposite sign.

Although the MTJs have similar TMR ratios, the TMS ratio of the Co_2FeSi based MTJ is more than 20 times larger than the TMS ratio of the Co-Fe-B based MTJ. Furthermore, the TMS ratios have opposing signs. The Seebeck voltages for the Co-Fe-B MTJs are approximately 10 µV at 150 mW, whereas for the Co_2FeSi the Seebeck voltages exceed -500 µV at the same laser power (cf. Tab. 4.1). This equals a factor of 50 between these two sample types or, in other words, an improvement of the signal level by 34 dB.

This outcome clearly reveals that the TMR and TMS effects are based on different transport mechanisms. In addition to that it exposes the capabilities of the Co_2FeSi based MTJs to generate high TMS effects and high Seebeck voltages. It also shows the benefits of using electrode materials for the TMS effect that contain a pseudo-gap in the DOS close to the chemical potential, like Co_2FeSi.

4.4.3. Comparison of Heusler compounds to Co-Fe-B MTJs

For a final comparison of the Heusler based MTJs to Co-Fe-B based MTJs with MgO barriers, it is useful to investigate the TMS and TMR effects of several devices. An overview of these effects for MTJs containing Co_2FeAl, Co_2FeSi, and two different $Co_xFe_{1-x}B_{20}$ composition investigated in this thesis is displayed in Fig. 4.21. For the Heusler compound MTJs TMR ratios of

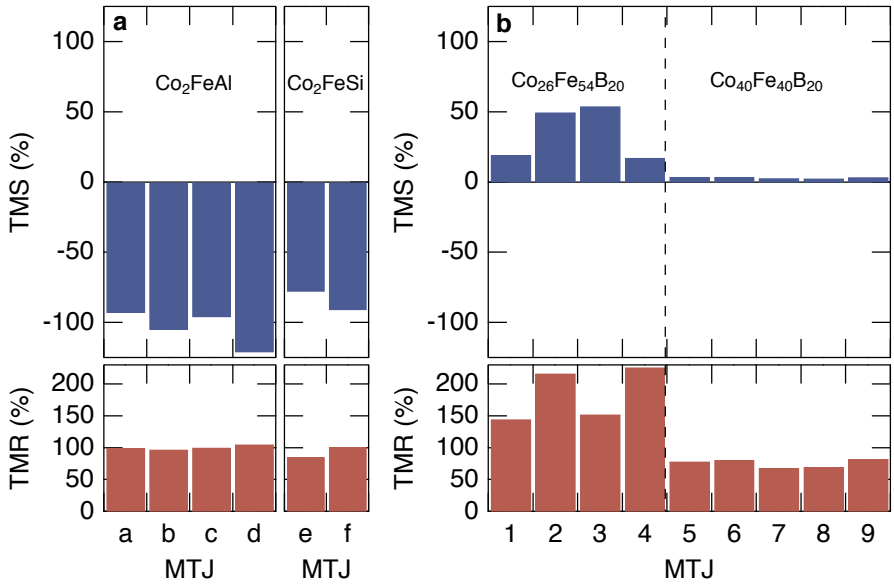

Figure 4.21. Comparison of TMR and TMS effect in Heusler compound and Co-Fe-B MTJs: a The TMS effect of Heusler compound MTJs ranges between −80 % and −120 %, whereas the TMR only reaches 100 %. **b** In $Co_{26}Fe_{54}B_{20}$ the TMS ratio does not exceed 50 %, although the TMR ratio reaches more than 200 %. MTJs with $Co_{40}Fe_{40}B_{20}$ electrodes exhibit TMR ratios comparable to Heusler based MTJs. The TMS ratios however only amount to a few percent.

nearly 100 % with very little deviations (Fig. 4.21a) are found, indicating the homogeneous properties among all MTJs. The TMS ratios range between −80 % to −120 %. A significant difference between the Co_2FeAl and Co_2FeSi based MTJs is not found. This is probably attributed to the comparable DOS of B2 ordered Co_2FeAl and $L2_1$ ordered Co_2FeSi.

For the Co-Fe-B based MTJs the picture is less homogeneous (Fig. 4.21b). MTJs containing two $Co_{26}Fe_{54}B_{20}$ electrodes show a high TMR ratio of up to 200 %, but only TMS ratios of maximum 50 %. For MTJs consisting of $Co_{40}Fe_{40}B_{20}$ electrodes the TMR effect only reaches up to 80 % with TMS ratios not exceeding 4 %.

For putting this into perspective the TMR effect sizes observed in this thesis are compared to values reported in literature. The maximum TMR ratios that have been reported for Heusler compound based MTJs were achieved with Co_2MnSi by Liu *et al.* [105] and reach up to nearly 2000 % at a temperature of 4.2 K. They still achieve 350 % at room temperature. A similar value of 330 % is observed by Wang *et al.* [38] for B2 ordered Co_2FeAl when the layer stacks are post annealed at high temperatures of 450 °C. This value reduces to 110 % when the samples are annealed at 300 °C, which is comparable to the results obtained in this thesis (Fig. 4.21a). For Co_2FeSi based MTJs maximum TMR effects of 170 % at 14 K and 118 % at room temperature have been observed by Sterwerf *et al.* [75], which is comparable to the values in this thesis. For $Co_{20}Fe_{60}B_{20}$ based MTJs Ikeda *et al.* [106] report a TMR ratio of 604 % at room temperature. These high values could not be reproduced in this work. A possible reasons for this might the use of MgO substrate instead of thermally oxidized Si substrate. MgO substrate has a slightly higher surface roughness than thermally oxidized Si substrate. Thus, MTJs prepared on MgO substrates probably possess a slightly reduced barrier quality than MTJs prepared on thermally oxidized Si. However, thermally oxidized Si is inappropriate for the observation of the TMS effect, since it causes a variety of parasitic effects that falsify the detection of the Seebeck voltages (cf. 4.1).

The comparison of the effect sizes in Fig. 4.21 already reveals the beneficial properties of Heusler based MTJs for the TMS effect. This advantageous behavior is even enforced, when looking at the Seebeck voltages (Tab. 4.2). For Co_2FeSi and Co_2FeAl based MTJs the values exceed at least $-200\,\mu V$ and reach up to more than $-600\,\mu V$. These are root-mean-square values obtained from the first harmonic of the lock-in amplifier at 150 mW laser power. Consequently, with a comparable DC heating source, the values are nearly twice as high and reach up to some mV.

Compared to these values, the Seebeck voltages of less than $10\,\mu V$ in $Co_{26}Fe_{54}B_{20}$ based MTJs appear extremely small. Although they exhibit maximum TMS ratios of slightly over 50 %, the proper detection of the signal for these small voltages is much more complicated than for the high signals generated by Heusler compound based MTJs.

Table 4.2. Comparison of MTJs with different materials: The elliptical MTJs have different sizes (a= 2 µm × 1 µm, b= 3 µm × 1 µm, c= 4 µm × 2 µm). The resistance is determined under a bias voltage of 10 mV and the Seebeck voltages are obtained by 150 mW laser heating with a spot diameter of ≈ 10 µm.

Materials	Size	R_p(kΩ)	R_{ap}(kΩ)	**TMR**	V_p(µV)	V_{ap}(µV)	**TMS**
$Co_{40}Fe_{40}B_{20}$ [1]	a	16.7	28.1	68 %	90.6	93.2	2.8 %
	c	0.84	1.51	79 %	35.7	37.0	3.7 %
$Co_{26}Fe_{54}B_{20}$ [2]	a	66.8	211.7	217 %	6.0	9.0	50 %
	a	61.4	200.7	227 %	8.4	9.9	18 %
Co_2FeAl [3]	a	5500	11000	100 %	−227	−442	−94 %
	b	5408	10850	93 %	−216	−434	−101 %
	b	2297	4536	97 %	−124	−258	−108 %
Co_2FeSi [4]	a	2151	3993	86 %	−366	−654	−78 %
	b	1673	3372	101 %	−263	−503	−91 %

[1] $Co_{40}Fe_{40}B_{20}$/MgO 1.5 nm/$Co_{40}Fe_{40}B_{20}$
[2] $Co_{26}Fe_{54}B_{20}$/MgO 1.7 nm/$Co_{26}Fe_{54}B_{20}$
[3] Co_2FeAl/MgO 2.0 nm/$Co_{40}Fe_{40}B_{20}$
[4] Co_2FeSi/MgO 2.0 nm/$Co_{70}Fe_{30}$

For the $Co_{40}Fe_{40}B_{20}$ based MTJs the Seebeck voltages at 150 mW laser power are slightly higher than for the $Co_{26}Fe_{54}B_{20}$ based MTJs, but still do not reach 100 µV. The drawback of the $Co_{40}Fe_{40}B_{20}$ composition is a strongly reduced TMS effect of less than 4 %. The low effect ratio makes these MTJs irrelevant for any use as memory devices based on the TMS effect.

The strong influence of the composition of the Co-Fe-B electrodes on the detected TMS values might be surprising. Yet, these results are in accordance with predictions of the TMS effect for different Fe_xCo_{1-x} compositions by Heiliger *et al.* [19]. For $Fe_{0.5}Co_{0.5}$ ($Co_{40}Fe_{40}B_{20}$) they predict high Seebeck coefficients of $\approx -30\,\mu V\,K^{-1}$and a low TMS effect ratio of a few percent. For a composition of $Fe_{0.68}Co_{0.32}$ ($Co_{26}Fe_{54}B_{20}$) they predict decreased Seebeck coefficients of $\approx -7\,\mu V\,K^{-1}$ but an enhanced TMS ratio of several hundred percent.

Chapter 5

Conclusion & Outlook

The major scope of this work is a deeper and more profound understanding of spin caloritronic effects in MTJs. More precisely, it aims at exposing the properties that are necessary to obtain high TMS effects. Therefore, in the first part of this thesis (Chapter 2) a theoretical model is elaborated that allows predictions of these properties. In the second part, these predictions are verified by experiments (Chapters 3 and 4).

For the implementation of the TMS effect into logic devices, large Seebeck coefficients and high TMS effect ratios are necessary. From the theoretical description of the TMS effect within the Landauer-Büttiker formalism, two basic ideas evolve for reaching these goals. First, the chemical potentials in the ferromagnetic electrodes of the MTJs can be shifted to a position with a highly asymmetric DOS by an external bias voltage. Second, the materials of the ferromagnetic electrodes can be replaced by materials that intrinsically provide an asymmetric DOS, e.g., an asymmetrically positioned gap, with respect to the chemical potential. The former method allows a quick scanning of the DOS in each electrode for asymmetries, and promises a deeper insight into the electric and thermal transport phenomena in MTJs. The latter approach is paving the path toward new improved devices for potential new spin caloritronic applications.

The linearized Landauer-Büttiker formalism (Sec. 2.3.3) is of great avail for connecting the DOS to the Seebeck coefficients. With the support of

this model, an effective method for predicting material combinations in MTJs with possibly high TMS effects, simply by considering their DOSs, is developed. This facilitates the use of material property repositories, such as AFLOW[52], that give access to a vast number of DOSs from density functional theory. The more sophisticated *ab initio* calculations of the transmissions of the MTJs remain only necessary for a precise prediction of the transport coefficients, such as the Seebeck coefficient and the conductance, for the selected materials of interest. Hence, the simplified approach, developed within this thesis, supports high throughput screening of materials that might be suitable for high TMS effects. These theoretical studies unveil that the electrode material of choice for high TMS effects has to possess a highly asymmetric DOS in the vicinity of the chemical potentials for one spin species, whereas, the other type of spins experiences a relatively flat DOS. Thus, half-metallic ferromagnets are identified as the ideal candidates for high TMS effects.

These remarkable predictions from the theoretical elaborations urge for an experimental examination. Therefore, a specifically designed laser heating setup that allows the investigation of magneto transport phenomena is used (Chapter 3). The laser setup and measurement electronics are optimized concerning the signal to noise ratio, the sharp on/off switching of the heating, and the exact positioning of the laser spot on top of the MTJ (Sec. 4.1). These improvements are crucial in obtaining reliable and reproducible results. Furthermore, it is proven that the time resolution of the heating and the measurement electronics is sufficient to detect parasitic effects that do not occur from Seebeck effects in the MTJs. In particular, semiconducting substrates are determined as the origin of the most severe parasitic influences. Hence, in this work MTJs on insulating MgO substrates are used exclusively for all TMS experiments.

With this reliable method high TMS effects of over $-100\,\%$ are obtained at the nearly half-metallic Heusler compounds Co_2FeAl (Sec. 4.4.1) and Co_2FeSi (Sec. 4.4.2). This material class is predicted to be ideal for high spin caloritronic effects based on their DOS (Sec. 2.4.2). Tab. 5.1 gives an overview of the most important results for the Heusler based MTJs in comparison to Co-Fe-B based MTJs. It clearly reveals that the Heusler based MTJs possess a significantly higher TMS effect ratio than their Co-Fe-B based

Table 5.1. Seebeck coefficients of MTJs with different materials: The elliptical MTJs have diameters of $2\,\mu m \times 1\,\mu m$. The Seebeck voltages are obtained at 150 mW laser heating.

Materials	$V_p\,(\mu V)$	$V_{ap}\,(\mu V)$	$S_p\,(\mu V\,K^{-1})$	$S_{ap}\,(\mu V\,K^{-1})$	**TMS**
$Co_{40}Fe_{40}B_{20}$ [1]	90.6	93.2	−750	−770	2.8 %
$Co_{26}F_{54}B_{20}$ [2]	6.0	9.0	−545	−818	50 %
Co_2FeAl [3]	−227	−442	582	1133	−95 %
Co_2FeSi [4]	−370	−664	948	1703	−80 %

[1] $Co_{40}Fe_{40}B_{20}$/MgO 1.5 nm/$Co_{40}Fe_{40}B_{20}$
[2] $Co_{26}Fe_{54}B_{20}$/MgO 1.7 nm/$Co_{26}Fe_{54}B_{20}$
[3] Co_2FeAl/MgO 2.0 nm/$Co_{40}Fe_{40}B_{20}$
[4] Co_2FeSi/MgO 2.0 nm/$Co_{70}Fe_{30}$

counterparts. Additionally, the Heusler based MTJs exhibit larger Seebeck voltages. To obtain a more comparable parameter, the temperature profile of each sample type is simulated (Sec. 3.4), and the Seebeck coefficient $S = -V/\Delta T$ is calculated from the Seebeck voltage and the temperature difference between the electrodes. Again, a higher value of the Seebeck coefficient is found for the Heusler compound based MTJs. Furthermore, the sign of the Seebeck voltage and coefficient are reversed, when replacing Co-Fe-B by a Heusler compound.

Both results support the introduced theoretical model that predicts a strong influence of the DOS not only on the size, but also on the sign of the obtained Seebeck coefficients (Secs. 2.2.2 and 2.4.2). When comparing Co_2FeSi and Co_2FeAl based MTJs, a higher Seebeck coefficient is found for the Co_2FeSi based MTJs. This difference is most likely generated by the more pronounced gap in the Co_2FeSi Heusler compound, compared to the quasi gap in the B2 ordered Co_2FeAl (Sec. 2.4.2). Nevertheless, both Heusler compounds are superior to Co-Fe-B showing higher TMS effects (Sec. 4.4.3).

This already emphasizes the extraordinariness of the results, which are concluded in two main aspects: First, these experiments introduce a new material class to the TMS effect that substantially improves the Seebeck voltage and effect ratio. The high TMS effects in Heusler compound based MTJs uncover a new and interesting feature of this versatile material class. In

spintronic applications, Heusler compound based MTJs have not been able to overtake their Co-Fe-B based counterparts. However, the opposite seems to be true for spin caloritronic applications, in which Heusler compound based devices exhibit higher signals and larger effect ratios. These remarkable benefits have been discovered and proven by the presented investigations. The robustness of these properties opens a new playground for further discoveries in the field of spin caloritronics that have remained concealed up to now. Second, and probably even more fundamental, the experimental results are a clear demonstration of the applicability of the simplified model that is elaborated in Sec. 2.4. The theoretical model in combination with experiments clearly reveals the important features in the DOS that are necessary to generate a high spin caloritronic effect. The thorough investigation and comparison of the TMR and TMS effects in different materials lead to a much deeper understanding of the fundamental contributions to these effects, and allow an efficient screening for improved spin caloritronic materials.

Another main aspect of this thesis, is the investigation of the TMS effect under an applied bias voltage. The nonlinearized Landauer-Büttiker formalism is presented as a suitable framework for investigating the thermoelectric transport in the MTJs when a temperature difference ΔT and a bias voltage V are applied across the tunnel barrier simultaneously (Sec. 2.4.1). This model allows to separate the different contributions to the tunneling current generated in the MTJs. This is crucial, because the AC heating of the MTJs does not only modulate ΔT, but additionally changes the base temperature $\overline{T}$ at the same frequency. Under an applied DC bias voltage both effects contribute to a change of the tunnel current ΔI between heating on/off. Hence, the experimental separation of the Seebeck contribution from the total signal is impossible. In simulations of the current, however, it is feasible to study a rise of $\overline{T}$ independently from the generation of a temperature difference ΔT. Within this theoretical framework the different contributions in Co-Fe-B/MgO/Co-Fe-B MTJs are easily distinguishable by their symmetry. Only by developing this description of the tunnel current in the Landauer-Büttiker formalism, two interesting new methods are developed: the bias-enhanced tunnel magneto-Seebeck (bTMS) effect drastically increases the magnetic readout contrast. Furthermore, a new technique to determine the Seebeck

voltages under an applied bias voltage by applying a linear model to the experimental data is introduced.

The bTMS effect combines two effective gradients across the tunnel barrier: a temperature gradient and a voltage. Both gradients drive charge currents that depend on different parameters. The bias voltage creates a current that mainly depends on the resistance. The temperature gradient generates a current that is additionally influenced by the Seebeck coefficient of the MTJ. Both parameters change differently when the magnetizations of the ferromagnets are reversed, which causes an on/off behavior of the bTMS signal at specific bias voltages (Sec. 4.3). Hence, the effect ratio diverges, which allows a much better readout contrast than the commonly used TMR effect. Experimentally, values of nearly $-3000\,\%$ are observed.

To cast light on the influence of the direct tuning of the chemical potentials on the TMS effect, a combination of the bTMS setup and the Landauer-Büttiker formalism is used (Sec. 4.3). An external bias voltage is applied to the MTJ to alter the relative position of the chemical potentials of the two ferromagnetic electrodes. The experimentally determined dependence of the Seebeck contribution to the overall current is comparable to the results of the simulations gained from the nonlinearized Landauer-Büttiker formalism (Sec. 2.4.1). For a small voltage range, which allows the use of the linearized Landauer-Büttiker formalism, even the bias voltage dependence of the Seebeck coefficients is obtained.

Both techniques – the tuning of the chemical potentials and the bTMS provide a large contrast of a physical property in the two magnetization states. This result makes them notably attractive for future applications in logic devices and memories.

Due to the novelty of the TMS effect, a lot of questions are still unanswered. Even more questions and ideas evolved during the experiments that are presented in this thesis. In the following paragraphs the most promising ideas and first concepts for their realization are presented.

An important aspect for future investigations will surely be the temperature dependence of the TMS effect. The influence of the base temperature on the TMS effect ratio is already visible in the Co_2FeSi based MTJs (Sec.4.4.2). This effect has to be studied in detail in a cryogenic environment. Therefore, the most accessible method is patterning a heater line on top of the MTJs, as

already demonstrated by Liebing *et al.* [5]. The results of low temperature experiments will provide a more fundamental understanding of the tunneling transport, and, hence, they can contribute to an improved material choice for the electrodes.

Not only the electrode materials, but also the barrier material influences the transport in an MTJ. Besides the known barrier materials Al_2O_3 and MgO, $MgAl_2O_4$ has recently received large interest, because it provides coherent tunneling and additionally posseses a decreased lattice mismatch to Co-Fe-B electrodes [39,40,107]. TMS data of Co-Fe-B/$MgAl_2O_4$ 1.8 nm/Co-Fe-B with a TMR effect of 34 % and a TMS ratio of 3.3 % have already been recorded [108], but lack the desired improvements. More detailed investigations of different barrier thicknesses and improved off-stoichiometric Mg-Al-O are a subject of ongoing experiments, and might reveal higher effect ratios.

An important task that could not be solved since the discovery of the TMS effect in 2011 is the exact determination of the temperature difference across the tunnel barrier. The group of Cahill has shown that time domain thermal reflectance (TDTR) [109] and time-resolved magneto optical Kerr effect (TR-MOKE) measurements [110] can reveal information on the temperature of a material. In a more recent work, they have shown that they can optically pump and probe the sample from different sides [110,111] and still obtain a reliable time dependent demagnetization signal in TR-MOKE experiments. For determining the temperature gradient across the thin MgO barrier in the earlier presented samples, their setup is modified allowing a combination of both temperature sensitive detection techniques. Therefore, layer stacks of $Co_{40}Fe_{40}B_{20}$ 1 nm / MgO 2 nm / Ru 100 nm are sputter deposited on double sided polished MgO substrate. The samples are *ex-situ* annealed at 300 °C for 1 h to crystallize the MgO film. For the generation of a temperature gradient, the pump pulse is applied to the thick Ru layer (Fig. 5.1). The Ru film serves as a transducer layer and prevents the laser light being transmitted to the MgO and Co-Fe-B layers. Since, the samples possess a ferromagnetic and a non-ferromagnetic layer adjacent to the MgO film, the TDTR technique is applied to probe the temperature in the non-ferromagnetic Ru layer and the TR-MOKE signal probes the ferromagnetic Co-Fe-B through the transparent MgO substrate.

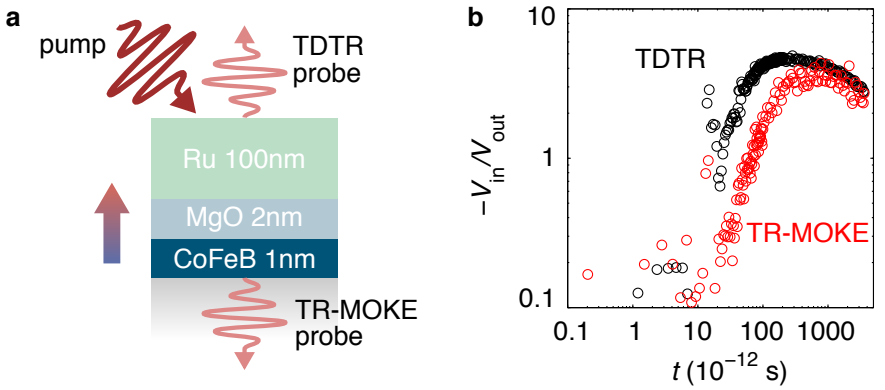

Figure 5.1. Temperature difference across a thin MgO layer: a Schematics of the sample and the pump-probe experiment. **b** Temporal evolution of the two probe methods.

The first results in Fig. 5.1b clearly reveal a different response of the detected signals. The TDTR signal, i.e., the temperature of the Ru layer, that is pumped by the laser, is rising earlier than the TR-MOKE signal from the back of the sample. This is a first sign of a heat propagation through the 2 nm thick MgO barrier and the generation of a temperature difference. For obtaining the temperature gradient from the in-phase V_{in} and out-of-phase V_{out} signals of the TDTR and TR-MOKE signals, a model for the thermal transport across the layers is pending. Nonetheless, the present results are promising for realizing a temperature measurement at both sides of the thin MgO layer. Thus, this technique is promising for obtaining more precise values of the temperatures and the thermal conductivity in the sample than the current COMSOL simulations.

In addition, the pump-probe technique allows the observation of thermal spin-transfer torques[111] in ferromagnet/Cu/ferromagnet spin valves. A comparable study of this important mechanism for the switching of the MTJs by applying a temperature gradient is still lacking.

Pump-probe experiments may also uncover the role of different relaxation mechanisms in the tunneling process. Exciting the electrons in the ferromagnetic electrodes with a short intense laser pulse might enable a tunneling

of hot electrons over the barrier before they relax with the lattice [112]. This decoupling of the electron and lattice temperatures can only be observed at short time scales. Hence, further investigations with the existing pump-probe setup are planned.

Of course, magneto Seebeck effects cannot only occur in magnetic tunnel junctions, but in any magnetoresistive device. One class of materials that is highly adabtable to a variety of demands, are organic semiconductors [113,114]. In particular their use in lateral organic spin valves is beneficial, since it allows the combination of field effects and magnetoresistance. Field effect modulated spin valves [115] and field effect modulated Seebeck coefficients [116] have already been investigated. However, a combination of these two effects, i.e., a field effect controlled magneto-Seebeck effect in an organic spin valve, is still lacking. For the investigation of Seebeck effects in these devices, it is desirable to use high magnetic fields, a stable sample environment and a well controlled temperature difference ΔT. Hence, a cryostat insert that fulfills these demands has been designed. A detailed description of this setup is found in Appendix E. First experiments at organic spin valve are pending, because prior to these investigations a calibration of the setup is needed. Nevertheless, first measurements of charge Seebeck and Nernst effects give reliable and reproducible results (Appendix E). Thus, further experiments with organic spin caloritronic devices are planned in the near future.

As a final conclusion, the theoretical and experimental elaborations in this thesis contribute fundamentally to the understanding of the TMS effects in MTJs. By using the linearized Landauer-Büttiker formalism to describe the thermoelectric transport in MTJs, a simplified, yet suitable model for the prediction of TMS effects from the DOSs of the ferromagnetic leads is established. Based on this, half-metallic Heusler compounds are revealed as the ideal electrode materials for MTJs with high TMS effects not only by theory, but also by experiments. This proves the applicability of the proposed model, and unveils a phenomenal new property of the versatile class of Heusler compounds. Further impressive insight into the electronic transport has been achieved by describing the current across an MTJ, which experiences an applied bias voltage and simultaneous temperature difference, in the nonlinearized Landauer-Büttiker formalism. This description leads to the

discovery of a significant new effect, the bias-enhanced TMS (bTMS) effect. The bTMS effect constitutes the first realization of on/off characteristics of the current through an MTJ under magnetization reversal. Furthermore, the nonlinearized formalism permits the investigation of Seebeck coefficients of an MTJ when the chemical potentials in the electrodes are shifted externally. This characteristics had been concealed up to now. Hence, these careful and profound investigations represent a vital contribution to the thriving fields of spin caloritronics and spintronics. The newly gained knowledge will hopefully support the discovery of innovative devices, e.g., power saving memories, as well as unknown fundamental physics.

Appendix

Appendix A

Linearization of the Landauer formula

For infinitesimally small differences in the chemical potential $\Delta\mu = \mu_\mathrm{L} - \mu_\mathrm{R}$ and temperatures $\Delta T = T_\mathrm{L} - T_\mathrm{R}$ the Landauer-Büttiker formalism (Eq. 2.3.3) is linearized to determine the conductance G and the Seebeck coefficient S. In the following a brief overview of the derivation of the linearized equations is presented. The starting point for the derivation is the Landauer transport equation (cf. Eq. 2.6):

$$I = \frac{e}{h} \int dE \left[f_\mathrm{L}^{\mu_\mathrm{L}, T_\mathrm{L}}(E) - f_\mathrm{R}^{\mu_\mathrm{R}, T_\mathrm{R}}(E) \right] \mathscr{T}(E) \tag{A.1}$$

The parameters at the Fermi-Dirac functions $f^{\mu,T}(E)$ indicate that these energy dependent functions also depend on the chemical potentials μ and the temperatures T of the corresponding reservoirs.

A.1. Conductance

First an expression for the answer of the system to a relative shift of the chemical potentials in the two reservoirs at zero temperature difference needs to be found. This resembles the situation of an ideal current measurement

under an infinitesimally small applied voltage. Since the difference $\mu_L - \mu_R$ is infinitesimally small $f_L(E) - f_R(E)$ is rewritten:

$$\frac{f_L(E) - f_R(E)}{\mu_L - \mu_R} \cong \frac{\partial f}{\partial \mu} \tag{A.2}$$

Hence, in this linear regime, Eq. A.1 is rewritten:

$$I = \frac{e}{h} \int dE \left(\frac{\partial f}{\partial \mu} \right) (\mu_L - \mu_R) \mathscr{T}(E) \tag{A.3}$$

The partial derivative is calculated using the Fermi function

$$\frac{1}{1 + \exp\left(\frac{E-\mu}{k_B T}\right)} = \frac{1}{1 + \exp(x)}, \text{ with } x = \frac{E - \mu}{k_B T} \tag{A.4}$$

Accordingly, the derivative is rewritten and it is obtained that

$$\frac{\partial f}{\partial \mu} = \frac{\partial f}{\partial x} \frac{\partial x}{\partial \mu} = \left(-\frac{1}{k_B T} \right) \cdot \frac{\partial f}{\partial x}. \tag{A.5}$$

Also the partial derivative of f with respect to the energy is calculated:

$$\frac{\partial f}{\partial E} = \frac{\partial f}{\partial x} \frac{\partial x}{\partial E} = \left(\frac{1}{k_B T} \right) \cdot \frac{\partial f}{\partial x} \tag{A.6}$$

The last two equations allow expressing the derivative of f with respect to the chemical potential through the derivative with respect to the energy:

$$\frac{\partial f}{\partial \mu} = -\frac{\partial f}{\partial E} \tag{A.7}$$

Now this is inserted into Eq. A.3 and the difference in chemical potential is replaced by a voltage $(\mu_L - \mu_R) = e \cdot V$:

$$I = \frac{e^2}{h} \int dE \left(-\frac{\partial f}{\partial E} \right) V \mathscr{T}(E) \tag{A.8}$$

The linear response of the conductor to an applied voltage or to a current are now expressed in terms of the conductance $G = I/V$:

$$\boxed{G = -\frac{e^2}{h} \int dE \left(\frac{\partial f}{\partial E} \right) \mathscr{T}(E)} \tag{A.9}$$

A.2. Seebeck coefficient

For the calculation of the Seebeck coefficient Eq. A.1 is linearized with respect to the temperature difference $\Delta T = (T_\mathrm{L} - T_\mathrm{R})$:

$$\frac{f_\mathrm{L}(E) - f_\mathrm{R}(E)}{T_\mathrm{L} - T_\mathrm{R}} \cong \frac{\partial f}{\partial T} \tag{A.10}$$

This replacement yields a thermocurrent in the linear regime:

$$I = \frac{e}{h} \int dE \left(\frac{\partial f}{\partial T} \right) \underbrace{(T_\mathrm{L} - T_\mathrm{R})}_{\Delta T} \mathscr{T}(E) \tag{A.11}$$

Next, the partial derivative of the Fermi function with respect to the temperature is calculated:

$$\frac{\partial f}{\partial T} = \frac{\partial f}{\partial x} \frac{\partial x}{\partial T} = \left(-\frac{E - \mu}{k_\mathrm{B} T^2} \right) \frac{\partial f}{\partial x} \tag{A.12}$$

Comparing this to equation A.6 results in:

$$\frac{\partial f}{\partial T} = \frac{\partial f}{\partial E} \left(-\frac{E - \mu}{T} \right) \tag{A.13}$$

The Seebeck coefficient is defined as $V = -S\Delta T$. With the conductance $G = I/V$ this is rewritten to $S = -I/(G\Delta T)$ and with equations A.9, A.11, and A.13 the Seebeck coefficient in the linear regime is gained:

$$\boxed{S = -\frac{1}{eT} \frac{\int dE \left(\frac{\partial f}{\partial E} \right) (E - \mu) \mathscr{T}(E)}{\int dE \left(\frac{\partial f}{\partial E} \right) \mathscr{T}(E)}} \tag{A.14}$$

Appendix B

Leakage current through the voltage amplifier

Leakage currents present in non-ideal voltmeters can cause parasitic contributions to the measured voltage. These undesired effects are enhanced, if the tested device and the voltmeter own similar resistances. Moreover, a change in the resistance of the measured device, such as in an MTJ, influences the voltage determined with a non-ideal voltmeter. This undesired change can lead to artificial TMS effects that are not related to the change of the Seebeck coefficients of the MTJ.

For the Seebeck voltage measurements a high impedance voltage amplifier with an input impedance of 1 TΩ is used as a voltmeter. It is directly connected to the bottom and top contacts of the MTJs with base resistances ranging from a few kΩ to several MΩ. The finite resistance of the amplifier allows a leakage current to travel through the circuit in Fig. B.1a. The leakage current I_{leak} can be calculated from the Seebeck voltage V_{Seebeck} and the total resistance of the circuit $R_{\mathrm{tot}} = R_{\mathrm{amp}} + R_{\mathrm{MTJ}}$, containing the series resistances of the amplifier and the MTJ:

$$I_{\mathrm{leak}} = \frac{V_{\mathrm{Seebeck}}}{R_{\mathrm{amp}} + R_{\mathrm{MTJ}}} \tag{B.1}$$

From this equation it is recognized that the leakage current changes with the resistance of the MTJ. If the resistance of the MTJ is much smaller than

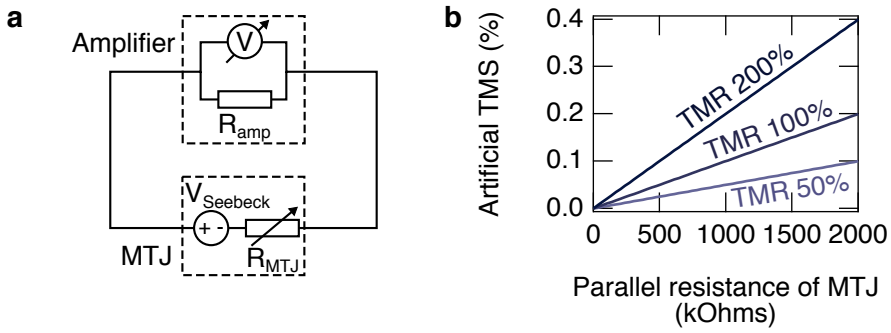

Figure B.1. Origin of artificial TMS effect: a Model circuit **b** Artificially generated TMS effect for MTJs with different parallel resistance R_p and different TMR ratios.

the input impedance of the amplifier, this contribution can be neglected, but for MTJs with resistances in the range of several MΩ it should checked whether the change of the resistance between the p and the ap state can lead to a similar change of the measured voltage as the expected TMS effect. For this purpose the voltage determined by the amplifier in the model circuit displayed in Fig. B.1a is calculated. The Seebeck voltage generated in the MTJ is kept constant, neglecting any dependence of the Seebeck coefficients on the magnetic orientation of the MTJ, but the resistance of the MTJ changes according to the TMR ratio (see Eq. 2.1):

$$R_\mathrm{MTJ}^\mathrm{ap} = R_\mathrm{MTJ}^\mathrm{p} \cdot (1 + \mathrm{TMR}) \tag{B.2}$$

The amplifier is modeled by an equivalent circuit consisting of an ideal voltmeter ($R \to \infty$) and the input resistance of the amplifier $R_\mathrm{amp} = 1\,\mathrm{M\Omega}$ connected in parallel. The voltage drop across the amplifier is determined by the input resistance and the leakage current:

$$V_\mathrm{amp}^\mathrm{p,ap} = R_\mathrm{amp} \cdot I_\mathrm{leak} = \frac{R_\mathrm{amp}}{R_\mathrm{amp} + R_\mathrm{MTJ}^\mathrm{p,ap}} \cdot V_\mathrm{Seebeck} \tag{B.3}$$

Inserting the voltages $V_{\mathrm{amp}}^{\mathrm{p}}$ and $V_{\mathrm{amp}}^{\mathrm{ap}}$ into the equation of the TMS ratio (Eq. 2.5) and using Eq. B.2, the ratio of the artificially generated TMS effect is calculated:

$$\mathrm{TMS}_{\mathrm{artifical}} = \frac{V_{\mathrm{amp}}^{\mathrm{p}}}{V_{\mathrm{amp}}^{\mathrm{ap}}} - 1 = \frac{R_{\mathrm{MTJ}}^{\mathrm{p}}}{R_{\mathrm{amp}} + R_{\mathrm{MTJ}}^{\mathrm{p}}} \cdot \mathrm{TMR} \tag{B.4}$$

For the ideal voltage amplifier ($R_{\mathrm{amp}} \to \infty$) the fraction of the resistances yields zero and the artificial TMS effect vanishes. For the non-ideal amplifier with $R_{\mathrm{amp}} = 1\,\mathrm{M\Omega}$ the size of the fraction depends on the difference between the resistance of the MTJ and the amplifier. This prefactor defines how much the TMR effect, i.e, the relative change of the resistance between the p and the ap state of the MTJ, contributes to the artificial TMS ratio. Fig. B.1b displays the size of the artificial TMS effect in dependence on the resistances of the MTJ in the p state. Even for an MTJ with a high resistance of $Rp = 2\,\mathrm{M\Omega}$ and a large TMR effect of 200 % the artificially generate TMS effect, due to the non-ideal voltage measurement, is below 0.5 %. Accordingly, any voltage change larger than this is not attributed to the finite resistance of the voltage amplifier and the TMR effect of the MTJ.

Appendix C

Tunnel magneto-Seebeck effect under bias voltage

This section represents an extension to the investigations of the TMS effect under applied bias voltage. It contains details on the measurement technique and additional experimental results that support the findings in Sec. 4.3. The information in this section has been published as supplementary information to Ref. [18] that directly evolved from the work performed for this thesis.

C.1. Direct and indirect determination of the Seebeck voltages

A direct measurement of the Seebeck voltage $S\Delta T$ is only possible when no external bias voltage is applied to the MTJ, but $S\Delta T$ can also be determined indirectly from the current and the resistance measurements (Eq. 2.22) [17,23]. Accordingly, both techniques are compared when no bias voltage is applied to the MTJ. For zero bias voltage ($V = 0\,\mathrm{mV}$) Eq. 2.22 gives $S\Delta T = 1/G \cdot \Delta I = R \cdot \Delta I$. Fig. C.1a shows a comparison of the directly and indirectly determined $S\Delta T$. The spikes in the curve of the indirect determination occur because of slight differences in the switching field for the bTMS (current) and TMR effect measurements (Fig. C.1b & c). The measured and indirectly determined

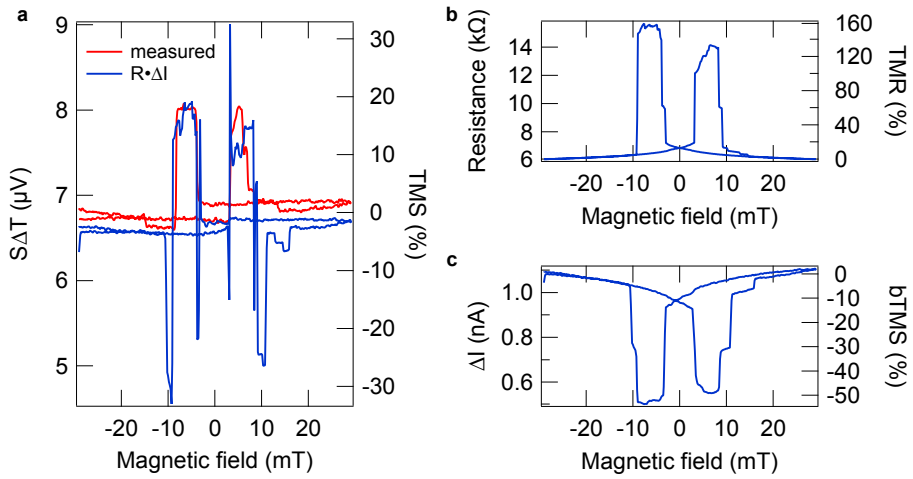

Figure C.1. Directly and indirectly determined Seebeck voltages without bias: **a** The directly measured Seebeck voltage ($S\Delta T$), and the indirectly obtained $S\Delta T$, recalculated from the current and resistance measurements, show the same switching fields and the same height. The corresponding TMS ratio is given on the right. **b** Dependence of the resistance R on the applied magnetic field and corresponding TMR ratio. The measurements are performed with a bias voltage of 10 mV. **c** Dependence of the Seebeck current ΔI on the applied magnetic field without bias voltage and corresponding bTMS ratio. Accordingly, the measured current $\Delta I = (1/R_{\mathrm{on}}) \cdot S\Delta T$ is proportional to the Seebeck coefficient and the inverse of the resistance (S/R). Hence, the measurements of b and c can be used to determine the blue curve in a.

Seebeck voltages have nearly the same height. Hence, a determination of the $S\Delta T$ from the current with this method (based on Eq. 2.22) leads to the correct deduction of the Seebeck coefficients and their dependence on the bias voltage.

C.2. Peltier and Thomson effects

For the correct interpretation of the results it is essential to calculate the heat current created by the DC charge current I_{DC} driven through the MTJ by the bias voltage (Peltier effect). The amount of heat generated

$$\dot{Q} = \Pi \cdot I_{\mathrm{DC}}, \qquad \Pi = ST \tag{C.1}$$

is directly proportional to the Peltier coefficient Π and, therefore, to the Seebeck coefficient S of the MTJ. At temperatures of $T \approx 400\,\mathrm{K}$ the measured Seebeck coefficients for Co-Fe-B/MgO MTJs are in the range of $100\,\mu\mathrm{V\,K^{-1}}$ to $770\,\mu\mathrm{V\,K^{-1}}$ [4,17,20]. For a minimal measured resistance of $6\,\mathrm{k\Omega}$ and a maximal applied bias voltage of 300 mV, this yields a maximum heat current of $Q_{\mathrm{max}} \approx 16\,\mu\mathrm{W}$. Thus, the heat generated by Peltier effects is neglected, as a laser with a power of up to 150 mW is focused on top of the MTJ, creating a much larger temperature difference across the barrier than the Peltier effect. Furthermore, a Thomson heat is generated by the temperature gradient and the current density j caused by the bias voltage and the Seebeck voltages across the MTJ. This effect is described by the heat production rate per unit volume as

$$\dot{q} = -Kj\nabla T, \qquad K = T \cdot \frac{dS}{dT} \tag{C.2}$$

when Joule heating and thermal conductivity are not included. K is the Thomson coefficient that is non-zero for Seebeck coefficients which depend on the temperature. For MTJs, the temperature dependence of the Seebeck coefficients has not been experimentally determined. *Ab initio* calculations [19] show that between 300 K and 400 K the Seebeck coefficients remain nearly constant for most Co-Fe compositions. This yields $dS/dT \approx 0$ and therefore Thomson effects vanish.

C.3. Bias enhanced TMS effect at a second MTJ

The bias enhanced tunnel-magneto Seebeck effect is measured for different laser powers at a second similar sample. The data presented in Fig. C.2

show the measured currents ΔI for different laser powers. Fig. C.2a displays the dependence of the measured currents ΔI on the applied bias voltage for different laser powers. The absolute value of ΔI is always larger in the ap state of the MTJ than in the p state. At this sample, a zero-crossing of the current in one magnetic state is found at bias voltages of approximately $-10\,\mathrm{mV}$ and $-2\,\mathrm{mV}$ ($\Delta I_{\mathrm{ap}}(-10\,\mathrm{mV}) \approx 0\,\mathrm{nA}$, $\Delta I_{\mathrm{ap}}(-2\,\mathrm{mV}) \approx 0\,\mathrm{nA}$). This on/off characteristics leads to high (theoretically diverging) bTMS ratios at these values of the bias voltage (Fig. C.2b). The zero-crossing of the current and the high bTMS effect ratios originate from a compensation of the thermal current and the current created by the bias voltage.

Fig. C.2c shows that the absolute current at a bias voltage of $-10\,\mathrm{mV}$ increases with rising laser power. The current in the p state is much smaller than in the ap state and has an opposite sign. The increase in both states can be explained by the larger base temperature and temperature gradient that is created when the laser power is raised. The larger temperatures lead to an increased ΔI according to Eq. 2.22, because the Seebeck contribution $S\Delta T$ and the difference of the resistance ΔR are increased. The current in the p state is set to a value close to zero by applying a bias voltage of $-10\,\mathrm{mV}$. The increase of this current exhibits that the Seebeck contribution to the overall current is rising with increasing laser power and cannot be compensated by the bias voltage contribution anymore. The current in the p state rises by a factor of 2 while the current in the ap state increases by a factor of 4.6, which leads to the observation of the highest bTMS ratio at a laser power of 150 mW and a bias voltage of $-10\,\mathrm{mV}$.

C.4. Contributions from the bias voltage and Seebeck voltage

In the experiment a zero current signal is found in the p state at a bias voltage of $-10\,\mathrm{mV}$ ($\Delta I_{\mathrm{ap}}(-10\,\mathrm{mV}) \approx 0\,\mathrm{nA}$). The corresponding Seebeck voltage $S_{\mathrm{p}}\Delta T$ that is compensated by the bias voltage of $-10\,\mathrm{mV}$ is calculated using Eq. 2.22. Further the measured conductances are needed for the MTJ in the

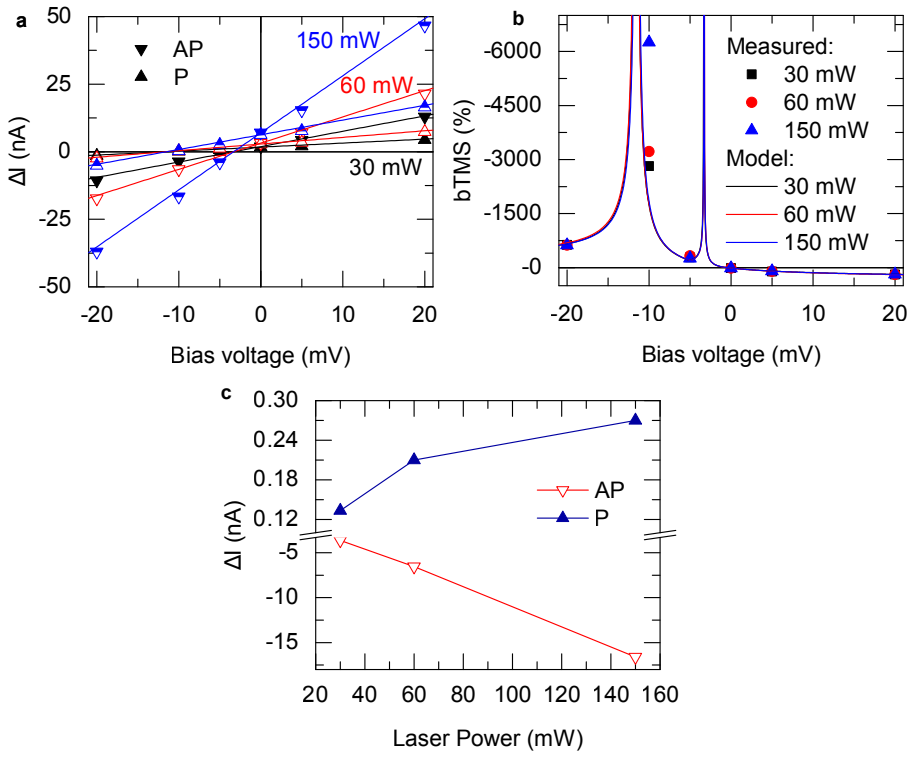

Figure C.2. Laser power dependence of the bias enhanced TMS effect: **a** Dependence of the current ΔI on the bias voltage for different laser powers. A zero-crossing of the current for one magnetic state can be observed at approximately $-10\,\mathrm{mV}$ and $-2\,\mathrm{mV}$. The absolute current rises with increasing laser power. **b** bTMS ratio determined from the measurements in a. The highest effect of more than $-6000\,\%$ is observed for a laser power of 150 mW. **c** Current measurements at an applied bias voltage of $-10\,\mathrm{mV}$. At this value of the bias voltage the current in the p state is close to zero, whereas, the current in the ap state is two orders of magnitude larger. The increase of the current in the p state shows that the Seebeck and the voltage contribution compensate better for smaller laser powers.

p state $G_{\mathrm{on}} \approx 194.97\,\mu\mathrm{S}$ and $G_{\mathrm{off}} \approx 194.70\,\mu\mathrm{S}$ when the laser is switched on or off, i.e., the MTJ is heated or at room temperature.

$$\frac{\Delta I}{G_{\mathrm{on}}} - \frac{G_{\mathrm{on}} - G_{\mathrm{off}}}{G_{\mathrm{on}}} = S\Delta T \tag{C.3}$$

$$S_{\mathrm{p}}\Delta T \approx -\frac{0.27\,\mu\mathrm{S}}{194.97\,\mu\mathrm{S}} \cdot (-10\,\mathrm{mV}) \approx 13.85\,\mu\mathrm{V} \tag{C.4}$$

The same calculation can be done for the ap state of the MTJ where a bias voltage of $-2\,\mathrm{mV}$ is needed to compensate the current signal $\Delta I_{\mathrm{ap}}(-2\,\mathrm{mV}) \approx 0\,\mathrm{nA}$. The conductances for the ap sate are $G_{\mathrm{on}} \approx 81.02\,\mu\mathrm{S}$ and $G_{\mathrm{off}} \approx 80.18\,\mu\mathrm{S}$.

$$S_{\mathrm{ap}}\Delta T \approx -\frac{0.84\,\mu\mathrm{S}}{81.02\,\mu\mathrm{S}} \cdot (-2\,\mathrm{mV}) \approx 20.8\,\mu\mathrm{V} \tag{C.5}$$

Because of the small factors $G_{\mathrm{on}} - G_{\mathrm{off}}/G_{\mathrm{on}}$ relatively high voltages in the millivolt regime are needed to compensate the contribution of the Seebeck voltages in the microvolt range to the measured currents ΔT. Seebeck voltages of some microvolts are measured at the investigated junctions when no bias voltage is applied (Fig. C.1a).

Appendix D

Further TMS data of Heusler based MTJs

D.1. Co_2FeAl based MTJs

In Sec. 4.4.1, it has already been discussed that the Co_2FeAl based MTJs exhibit high Seebeck voltages and high TMS ratios that are very reproducible among different MTJs. Here, the data of the elliptical MTJ (diameters $3\,\mu m \times 1\,\mu m$) investigated in Fig. 4.9 is studied in more detail. Fig. D.1a displays the Seebeck voltage under changing external magnetic field for different laser powers. These curves are recorded with a laser spot diameter of $10\,\mu m$. Similar to the data presented in Sec. 4.4.1, an abrupt switching of the Seebeck voltage between the p and ap state of the MTJ is observed. The switching fields are consistent with the switching of the resistance in the TMR measurement at the same MTJ (Fig. D.1b). The voltage in each state rises linearly with the applied power, i.e., with increasing temperature gradient across the barrier. The highest voltages have been obtained at 150 mW and amount to $V_p = -218\,\mu V$ and $V_{ap} = -429\,\mu V$. This difference yields a TMS ratio of approximately 96 %. The ratio is nearly constant with varying laser power, which is in good agreement with the observations discussed in Sec. 4.4.1. With a temperature difference of 390 mK across the barrier (cf. Sec. 4.2.1), the Seebeck coefficients yield $S_p = 559\,\mu V\,K^{-1}$

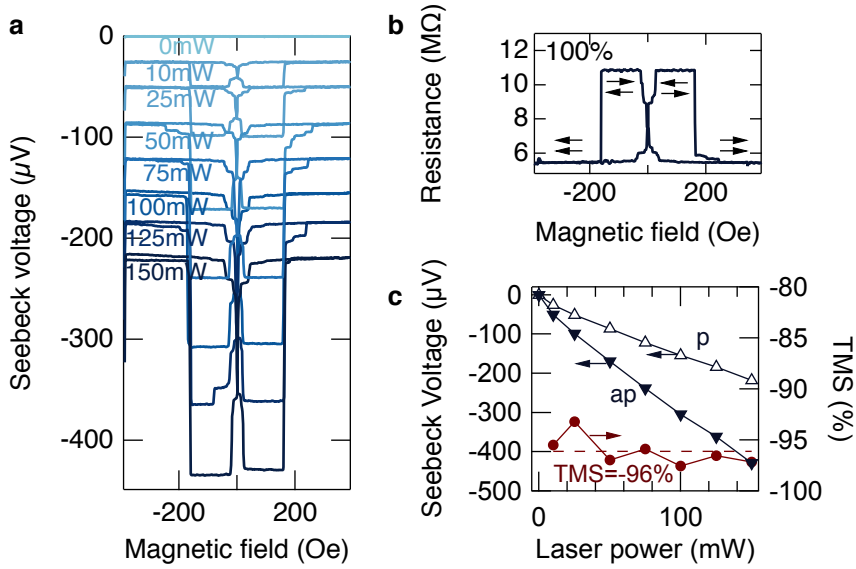

Figure D.1. Tunnel magneto-Seebeck effect of a Co_2FeAl based MTJ. a Dependence of the Seebeck voltage on the magnetic field. **b** Tunnel magneto resistance. **c** Evolution of the voltage in the p and ap state, and the TMS ratio derived from these voltages with rising laser power. The MTJ has a size of $3\,\mu m \times 1\,\mu m$

and $S_{ap} = 1100\,\mu V\,K^{-1}$, which are even slightly higher than for the data presented in Fig.4.10.

D.2. Co_2FeSi based MTJs

In Sec. 4.4.2, it has already been revealed that the Seebeck voltage nicely follows the switching behavior of the resistance in Co_2FeSi based MTJs. Furthermore, a slight decrease of the TMS ratio is observed when the laser power is increased. A similar dependence is observed for a second, marginally larger, MTJ of $3\,\mu m \times 1\,\mu m$. The Seebeck voltage in this MTJ reaches $-500\,\mu V$ in the ap state at 150 mW. This value is a little smaller than for the $2\,\mu m \times 1\,\mu m$ sized MTJ described in Fig. 4.16. On the other hand, the averaged TMS ratio of the larger MTJ is $-95\,\%$, which is 10 % larger than

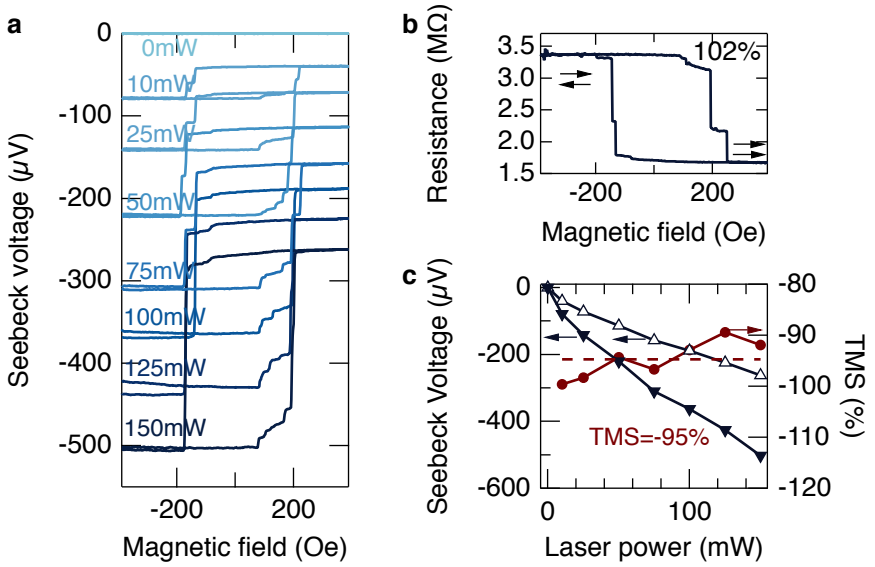

Figure D.2. Tunnel magneto-Seebeck effect of a Co_2FeSi based MTJ. a Dependence of the Seebeck voltage on the magnetic field. **b** Tunnel magneto resistance. **c** Evolution of the voltage in the p and ap state, and the TMS ratio derived from these voltages with rising laser power. The MTJ has a size of $3\,\mu m \times 1\,\mu m$

for the smaller MTJ. A comparable difference is also found for the TMR ratio, which amounts to 102 % in the larger MTJ (Fig. D.2b) and 86 % in the smaller MTJ (Fig. 4.16). Accordingly, the decreased of TMS ratio of the smaller MTJ is attributed to the less pronounced change of the transport coefficient between the p and the ap state. The most probable origin for this difference between the MTJs is the locally reduced barrier quality, e.g., because of pin holes, in the smaller MTJ. This assumption is supported by the reduced resistance-area product of the smaller MTJ (see Tab. 4.1).

Appendix E

Cryostat insert for Seebeck and Nernst experiments

The topic of this thesis is the investigation of magneto-Seebeck effects in MTJs. However, other devices based on various materials also show interesting magneto-Seebeck effects. One material class that particularly caught my interest are organic semiconductors[114,117,118]. This material class is a promising canditate for the combination of field effects[119], magnetoresistance[115], and Seebeck effects[116]. For the experimental investigation of these effects two ingredients are needed. The first ingredient is a device that combines an organic field effect transistor[119] with a lateral spin valve[114]. The realization of such a device has been presented by Dediu *et al.*[120]. The second ingredient is a well controlled sample environment that allows the application of a stable temperature difference to the lateral spin valves. This temperature difference is necessary for the generation of a Seebeck effect. An appropriate experimental setup has been designed during the work related to this thesis.

First, the organic field effect is investigated. The setup used for these investigations has been designed by Kai Bagschik during his diploma thesis[121]. Tests of copper phthalocyanine (CuPc) organic field effect transistors (OFET) with gold source and drain contacts prove that it is possible to reproduce the field effect in samples prepared in this setup. Therefore, the contacts

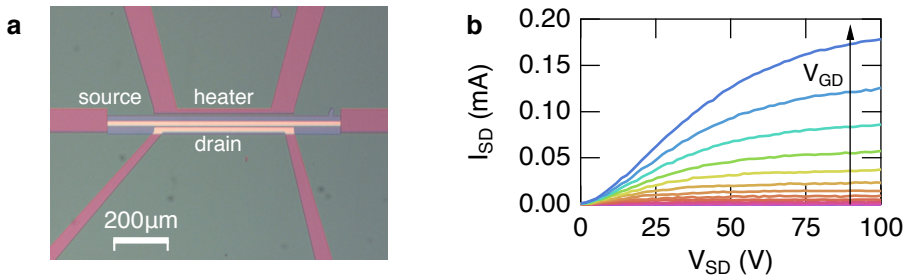

Figure E.1. Organic field effect transistor: a Top view of the contacts of a field effect transistor with a channel length of 500 µm and a channel width of 5 µm. **b** Characteristic source-drain current versus voltage curves under gate-drain voltages between 0 V to 106 V in steps of 6.6 V.

for the source and drain of the transistor are patterned on a Si/SiO_2 500 nm substrates. The channel width of the OFET is 5 µm and the channel length is 500 µm. For future Seebeck experiments an additional insulated heater line is patterned close to the channel of the OFET. For gating the OFET a voltage is applied to the back side of the silicon substrate that is insulated from the channel by 500 nm of SiO_2. A microscopy image of the patterned sample is shown in Fig. E.1a. For finishing the OFET, a layer of CuPc is evaporated on top of the source and drain contacts in a vacuum chamber. The microscopy image shows that only the source and drain contacts are accessible for the CuPc, while all leads and the heater are covered by an insulator. Experimentally determined source-drain currents I_{SD} in dependence of the source-drain voltage V_{SD} for different gate-drain voltages V_{GD} are shown in Fig. E.1b. The results reveal the characteristic shapes of these curves, as expected for a field effect transistor.

For the investigations of Seebeck coefficients a precise control of the sample temperature under an applied temperature difference is crucial. To realize this task, a cryostat insert has been designed that allows experiments between 77 K and 400 K, either in vacuum, or in a gas atmosphere, e.g., N_2 or Ar. The whole cryostat setup is placed inside the bore of a 5 T cryomagnet to allow magneto transport experiments.

Two different mounts exist for the sample. In the first sample mount (Fig. E.2), the temperature difference is applied in the in-plane direction of the sample by a heater attached to only one side of the sample mount. The temperatures and the temperature difference are controlled by two Cernox™ temperature senors placed on top of the sample close to the device under test. For providing a constant base temperature, a second heater is attached to the sample mount that allows a homogeneous heating. This heater is controlled by a temperature control feedback loop that takes the temperature of the Cernox™ as an input parameter and accordingly sets the power of the heater. For electrical contact to the sample wire bonding is used. Since the sample mount can be rotated, the magnetic field can be rotated from the in-plane axis of the sample to the out-of-plane direction.

The second sample mount allows the application of a temperature difference along the out-of-plane direction of the sample. Here, the temperature difference is generated via two Peltier cells. One of them cools the sample, the other one is functioning as a heater. In this case not only the temperature difference, but also the thermal flux thorough the sample can be monitored by two passive Peltier cells that act as heat flux sensors. With this setup the direction of the magnetic field can be rotated in the plane of the sample. This, for example, allows to investigate the anisotropy of thermoelectric effects.

First experiments in organic based spin valves are still pending, since their testing is not yet completed. Before reliable Seebeck effect measurements can be obtained the samples have to be tested concerning the magnetoresistance and field effects. Finding the right materials for the electrodes and the channel is not easy. This is particularly delicate, because the electronic levels of the organic semiconductors do not match the electronic structure of the ferromagnetic, metallic electrodes[115]. Accordingly, at the current status an implementation of MgO tunnel barriers to obtain a better spin injection into the channel of the OFET is tried. Once a high quality tunnel barrier is grown on the source and drain contacts, these devices will be tested considering their magnetoresistive properties.

However, besides the investigation of Seebeck effects in gated organic spin valves, the cryogenic setup can be used to investigate other magneto transport and magneto thermal effects. The probably most prominent megneto

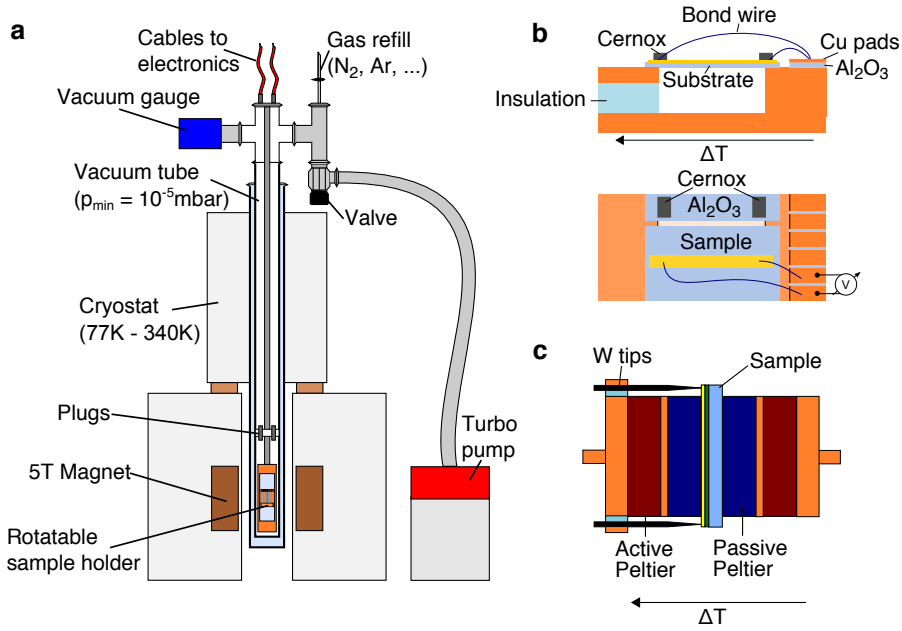

Figure E.2. Cryostat setup for Seebeck and Nernst experiments: a Overview of the setup with sample environment and connections to the outside. **b** Sample mount for experiments with in-plane ΔT. The magnetic field can be rotated from in-plane to out-of-plane. **c** Sample mount for experiments with out-of-plane ΔT. The magnetic field can be rotated in the sample plane.

transport effect is the Hall effect[122]. If a current J_x is passed through a conductor that experiences a perpendicular magnetic field B_z, a transverse electrical field E_y is generated[28]. The generation of the electric field is attributed to the Lorentz-force that acts on the electrons forming the current. In a general form the ordinary Hall effect is expressed as

$$\vec{E} = -\mu_0 R_H \vec{J} \times \vec{H}, \tag{E.1}$$

where $\vec{H}$ is the magnetic field, μ_0 is the magnetic permeability and R_H is the Hall coefficient[123]. In a ferromagnetic conductor, the Hall effect is not only generated by an external magnetic field, but also by the magnetization $\vec{M}$

of the ferromagnet. This effect is called the anomalous Hall effect (AHE), which generates an electric field dependent on the magnetization

$$\vec{E} = R_{\mathrm{AHE}} \vec{J} \times \vec{M}, \tag{E.2}$$

with the anomalous Hall coefficient R_{AHE}. In experiments usually the Hall resistivity

$$\rho_{xy} = \frac{E_y}{J_x} \tag{E.3}$$

is given as a function of the externally applied field. Hence, for ferromagnets usually a hysteresis loop is received, when ρ_{xy} is studied under sufficiently large varying external magnetic fields.

The thermoelectric counterpart to the Hall effect is the Nernst effect [124]. Instead of a voltage driven this effect uses a thermally driven charge current that arises from a Seebeck effect. Thus, the current $\vec{J}$ is replaced by a temperature gradient ∇T [123]. This yields

$$\vec{E} = \mu_0 N_{\mathrm{NE}} \nabla T \times \vec{H}, \qquad \vec{E} = N_{\mathrm{ANE}} \nabla T \times \vec{M} \tag{E.4}$$

for the ordinary and the anomalous Nernst effects (ANE), respectively. For the presentation of experimental data it is convenient to define a transverse Seebeck coefficient

$$S_{xy} = \frac{E_y}{(\nabla T)_x}. \tag{E.5}$$

Both, the Hall effect and the Nernst effect show a similar response to the external magnetic field and the magnetization.

With the sample mount that can provide an in-plane temperature gradient, it is possible to determine the temperature dependence of the Hall and Nernst effects in Mn_2Ru_xGa. This material is of particular interest, because, by alloying Ru into Mn_2Ga it is possible to prepare a zero-moment ferrimagnet with high spin polarization [125]. The zero net-magnetization is created by a compensation of the magnetization of two antiferromagnetically coupled Mn sublattices. Hence, the material is a ferrimagnet for most temperatures, and the loss of the overall magnetization is only reached at

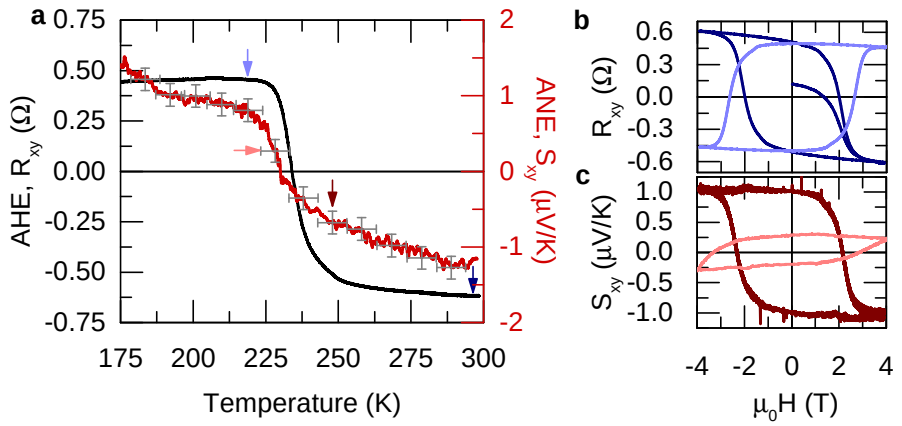

Figure E.3. Hall and Nernst effects of a Mn_2Ru_xGa film: **a** Temperature dependence of the Hall and Nernst voltage without external field. **b** Hall effect measurements before and after the compensation point. **c** Corresponding Nernst effect measurements. The corresponding data points of the curves in b and c are marked by arrows in a.

a distinct compensation temperature. Before and after this compensation point the Hall coefficients have opposing signs. This can be observed by performing anomalous Hall effect measurements with varying base temperature. In Fig. E.3a we can clearly see that the anomalous Hall signal recorded at an external field of 4 T decreases with rising temperature. It vanishes at a temperature of approximately 235 K and then increases again, but with opposite sign. The origin of this reverse is a different temperature dependence of the magnetization on the two Mn sublattices as explained in detail by Kurt *et al.* [125] and Thiyagarajah *et al.* [126].

The reversal of the anomalous Hall effect is seen even more clearly when we consider two individual Hall effect measurements, as presented in Fig. E.3b. These curves are recorded after the Mn sublattices already recovered their magnetization on both sides of the compensation points. It can be seen that the contribution from the anomalous Hall effect that forms a hysteresis loop changes sign.

A similar behavior is also found for the Nernst effect. The temperature dependent data are displayed as the red curve in Fig. E.3a. The amplitude of the signal decreases until it reaches the compensation point, where it vanishes. For higher temperatures it increases again but with opposite sign. This also indicates the reversal of the magnetization as already observed by the Hall effect. Fig. E.3c reveals this result more clearly. The two hysteresis loops, originating from the anomalous Nernst effect are recorded at different temperatures above and below the compensation point. For the solid line, the temperature is well above the compensation point, at which the magnetization of the sublattices is already recovered, resulting in a clear hysteresis loop. For the dashed line, the temperature is only slightly above the compensation point, leading to a decreased overall magnetization and, hence, a smaller hysteresis loop. However, the reversal of the signal, due to the reversed magnetization, is still visible. The data obtained from hysteresis loops at different temperatures are indicated by the grey markers on top of the red temperature dependent data.

These data of the Hall and Nernst effects in Mn-Ru-Ga are an impressive demonstration of the versatility of the designed cryostat setup. Not only does it allow the investigation of Seebeck effects in nano patterned devices, but it also offers a powerful tool for the insight into more fundamental physical effects that only occur under an applied temperature gradient. The specialties of this setup are its precise temperature control and high external magnetic fields.

Publications

A. Boehnke, M. Walter, N. Roschewsky, T. Eggebrecht, V. Drewello, K. Rott, M. Münzenberg, A. Thomas, and G. Reiss, 'Time-resolved measurement of the tunnel magneto-Seebeck effect in a single magnetic tunnel junction', *Review of Scientific Instruments* **84,** 063905 (2013).

C. Klewe, M. Meinert, A. Boehnke, K. Kuepper, E. Arenholz, A. Gupta, J.M. Schmalhorst, T. Kuschel, and G. Reiss, 'Physical characteristics and cation distribution of $NiFe_2O_4$ thin films with high resistivity prepared by reactive co-sputtering', *Journal of Applied Physics* **115,** 123903 (2014).

N. Teichert, A. Boehnke, A. Behler, B. Weise, A. Waske, and A. Hütten, 'Exchange bias effect in martensitic epitaxial Ni-Mn-Sn thin films applied to pin CoFeB/MgO/CoFeB magnetic tunnel junctions', *Applied Physics Letters* **106,** 192401 (2015).

A. Boehnke, M. Milnikel, M. von der Ehe, C. Franz, V. Zbarsky, M. Czerner, K. Rott, A. Thomas, C. Heiliger, G. Reiss, and M. Münzenberg, 'On/off switching of bit readout in bias-enhanced tunnel magneto-Seebeck effect', *Scientific Reports* **5,** 8945 (2015).

N. Teichert, D. Kucza, O. Yildirim, E. Yuzuak, I. Dincer, A. Behler, B. Weise, L. Helmich, A. Boehnke, S. Klimova, A. Waske, Y. Elerman, and A. Hütten, 'Structure and giant inverse magnetocaloric effect of epitaxial Ni-Co-Mn-Al films', *Physical Review B* **91,** 184405 (2015).

T. Huebner, A. Boehnke, U. Martens, A. Thomas, J.-M. Schmalhorst, G. Reiss, M. Münzenberg, and T. Kuschel, 'Comparison of laser induced and intrinsic tunnel magneto-Seebeck effect in CoFeB/$MgAl_2O_4$ and CoFeB/MgO magnetic tunnel junctions', *Physical Review B* **93,** 224433 (2016).

Conferences & Talks

03/2013 Talk at the **77th Deutsche Physikalische Gesellschaft (DPG) spring meeting,** Regensburg, Germany

10/2013 Talk at the **SpinCaT PhD workshop,** Dresden, Germany

11/2013 Talk at the **58th Annual Magnetism and Magnetic Materials (MMM) conference,** Denver (CO), USA

11/2013 Talk at the **Department of Physics and Astronomy, University of Denver,** Denver (CO), USA

01/2014 Talk and poster at the **550. WE-Heraeus Seminar on "Spin transport beyond Boltzmann",** Bad Honnef, Germany

03/2014 Talk and poster at the **78th Deutsche Physikalische Gesellschaft (DPG) spring meeting,** Dresden, Germany

05/2014 Talk at the **Project meeting of EURAMET EXL04 SpinCal,** Berlin, Germany

07/2014 Poster at the **Spin caloritronics VI,** Irsee, Germany

10/2014 Member of the organizing committee of the **SpinCaT PhD workshop,** Bielefeld, Germany

11/2014 Talk and poster at the **59th Annual Magnetism and Magnetic Materials (MMM) conference,** Honolulu (HI), USA

01/2015 Poster at the **580. WE-Heraeus Sminar on "Oxide Spintronics",** Bad Honnef, Germany

02/2015 Poster at the **Coloquium of the SPP 1538 (SpinCaT),** Bad Honnef, Germany

03/2015 Talk at the **79th Deutsche Physikalische Gesellschaft (DPG) spring meeting,** Berlin, Germany

06/2015 Talk at the **SpinCaT PhD workshop,** Munich, Germany

06/2015 Poster at the **Spin Mechanics 3 conference,** Munich, Germany

09/2015 Poster at the **Symposium "Spins, Waves and Interactions",** Greifswald, Germany

01/2016 Talk at the **13th Joint Magnetism and Magnetic Materials (MMM)-Intermag Conference**, San Diego (CA), USA

03/2016 Talk at the **Coloquium of the SPP 1538 (SpinCaT),** Bad Honnef, Germany

03/2016 Talk at the **80th Deutsche Physikalische Gesellschaft (DPG) spring meeting,** Regensburg, Germany

Acknowledgments

I am greatly indebted to the people and organizations that have contributed to the success of this thesis. Here, I would like to express my particular gratitude to some of them.

The work presented in this thesis has received funding from the German Research Foundation (DFG) within the priority project SPP1538 SpinCaT, the metrology project EMRP EXL04 SpinCal, and the HARFIR R&D project funded by the European Commission under the 7th Framework Programme (FP7-NMP-2013-EU-Japan). Furthermore, I acknowledge the German Academic Exchange Service (DAAD) for granting a scholarship that enabled me to spent a research stay of seven months at the Trinity College Dublin, Ireland.

I would like to thank Günter Reiss for reviewing and supervising my thesis. He has been a great mentor, scientific and personal, and numerous fruitful ideas evolved from the intense discussion within the last years. Besides him, I would like to thank all members of the "Center for Spinelectronic Materials and Devices" for their support and the positive atmosphere. It has always been a pleasure to work with all of you. Also, I would like to thank Timo Kuschel, who has always been a source of inspiration and honest opinions, as well as a valuable tutor for the induction into the global scientific community. I thank Andy Thomas for being a great teacher on writing publications and for always being able to spread a positive atmosphere. Thanks are also due to Alessia Niesen, Christian Sterwerf and Jana Ludwig who have helped a lot in the preparation of the high quality Heusler compound MTJs and not only because of this they made life in the lab much more pleasant. My thanks are also expressed to Karsten Rott, who kept the laboratory equipment in

a flawless state and was never getting tired in sharing his knowledge on the preparation of spintronic devices. Furthermore, I would like to thank Torsten Hübner for always enduring the long session in the laser lab and eagerly supporting all the ideas that crossed my mind, no matter what time of day or night. For DFT calculations and for not getting tired in answering my questions I express my thanks to Markus Meinert. I cordially thank Aggi Windman for mastering all administrative tasks, allowing me to concentrate on the scientific tasks.

I highly appreciate Markus Münzenberg's commitment and the efforts of his group at the Ernst-Moritz-Arndt Universität Greifswald to support my research. Particularly I would like to thank Marvin von der Ehe, Ulrike Martens, and Jakob Walowski for always providing an open and productive environment, perfectly maintained experimental equipment, and making my research stays as pleasant as possible.

Furthermore, I express my gratitude to Christian Heiliger from the Justus-Liebig Universität Gießen, who eagerly answered all my questions regarding the theoretical models and patiently listened to the description of my experiments. The models and DFT calculations provided by him, Michael Czerner and Christian Franz, have been a vital ingredient for new experimental ideas and for proving our observations. I would also like to thank him for reviewing this thesis.

I thank David Cahill and Johannes Kimling from the University of Illinois at Urbana-Champaign for supporting my ideas, and for their willingness to perform TDTR experiments on our samples. Their measurements might largely contribute to a determination of the temperature difference across a thin tunnel barrier.

I thank Hans Werner Schumacher, Niklas Liebing, and Patryk Krzysteczko from the PTB Braunschweig for interesting and enthusiastic discussions, and an open atmosphere that enabled a deep insight into their tunnel magneto-Seebeck experiments.

I kindly like to thank Michael Coey for giving me the opportunity to spend seven months in his thriving group at the Trinity College Dublin, Ireland. Cordial thanks are due to my mentor Zsolt Gercsi who patiently not only taught me a lot about physics but also about life in Ireland that I would not have learned without him. He and the whole group, particularly, my

colleagues Gwenael Atcheson, Karl Ackland, Karsten Rode, Plamen Stamenov, Stephen Porter, Jane Mary O'Reilly, João Coelho, Kiril Borisov, Davide Betto, Naganivetha Thiyagarajah, and Chris Murray made this an interesting and unforgettable time. Working with you was great and helped me progressing scientifically and personally!

Particularly, I would like to thank my close colleagues Christoph Klewe, Niclas Teichert, Christan Sterwerf, Frank Wittbracht, Peter Hedwig, Alessia Niesen, Lars Helmich, Andreas Hütten, Daniel Meier, Manuel Glas, Stefan Niehörster, Marvin von der Ehe, Robin Silber, Panagiota Bougiatioti, and Orestis Manos, who made a lot of things much easier and work much more enjoyable. Some of them became good friends over the last years and will hopefully always be.

Of course, I also want to thank my friends and family, who always supported me and did their best to cheer me up, when I had a bad day in the lab.

I would like to express special thanks to Birte Riechers, who has always been able to find the right words to brighten up my mood and who always brought me back on course. Without her the difficult days would have been more challenging, but also the successful moments would have been less glorious.

Finally, the greatest thanks of all are dedicated to my parents Inge and Dietmar, who have always been there and never let me down. They did their utmost in providing me with a thorough education and passing on their knowledge necessary for a successful and content life. Their support has been essential in reaching my goals and I highly appreciate their commitment. I could not imagine a better foundation for my future.

Thank you all!

Bibliography

[1] G. E. W. Bauer, E. Saitoh, B. J. van Wees, *Nature Materials* **2012**, *11*, 391–9.

[2] S. R. Boona, R. C. Myers, J. P. Heremans, *Energy & Environmental Science* **2014**, *7*, 885.

[3] M. Czerner, M. Bachmann, C. Heiliger, *Physical Review B* **2011**, *83*, 132405.

[4] M. Walter, J. Walowski, V. Zbarsky, M. Münzenberg, M. Schäfers, D. Ebke, G. Reiss, A. Thomas, P. Peretzki, M. Seibt, J. S. Moodera, M. Czerner, M. Bachmann, C. Heiliger, *Nature Materials* **2011**, *10*, 742–746.

[5] N. Liebing, S. Serrano-Guisan, K. Rott, G. Reiss, J. Langer, B. Ocker, H. W. Schumacher, *Physical Review Letters* **2011**, *107*, 177201.

[6] K. Uchida, S. Takahashi, K. Harii, J. Ieda, W. Koshibae, K. Ando, S. Maekawa, E. Saitoh, *Nature* **2008**, *455*, 778–81.

[7] K.-i. Uchida, H. Adachi, T. Ota, H. Nakayama, S. Maekawa, E. Saitoh, *Applied Physics Letters* **2010**, *97*, 172505.

[8] M. Julliere, *Physics Letters A* **1975**, *54*, 225–226.

[9] T. Miyazaki, N. Tezuka, *Journal of Magnetism and Magnetic Materials* **1995**, *139*, L231–L234.

[10] S. S. P. Parkin, C. Kaiser, A. Panchula, P. M. Rice, B. Hughes, M. Samant, S.-H. Yang, *Nature Materials* **2004**, *3*, 862–867.

[11] J. S. Moodera, L. R. Kinder, T. M. Wong, R. Meservey, *Physical Review Letters* **1995**, *74*, 3273–3276.

[12] D. Ebke, J. Schmalhorst, N.-N. Liu, A. Thomas, G. Reiss, A. Hütten, *Applied Physics Letters* **2006**, *89*, 162506.

[13] R. Meservey, P. Tedrow, *Physics Reports* **1994**, *238*, 173–243.

[14] C. Gould, C. Rüster, T. Jungwirth, E. Girgis, G. M. Schott, R. Giraud, K. Brunner, G. Schmidt, L. W. Molenkamp, *Physical Review Letters* **2004**, *93*, 1–4.

[15] S. A. Wolf, D. D. Awschalom, R. A. Buhrman, J. M. Daughton, S. von Molnár, M. L. Roukes, A. Y. Chtchelkanova, D. M. Treger, *Science (New York N.Y.)* **2001**, *294*, 1488–95.

[16] J. M. D. Coey, *Magnetism and Magnetic Materials*, Cambridge University Press, **2010**.

[17] A. Boehnke, M. Walter, N. Roschewsky, T. Eggebrecht, V. Drewello, K. Rott, M. Münzenberg, A. Thomas, G. Reiss, *The Review of scientific instruments* **2013**, *84*, 063905.

[18] A. Boehnke, M. Milnikel, M. Walter, V. Zbarsky, C. Franz, M. Czerner, K. Rott, A. Thomas, C. Heiliger, M. Münzenberg, G. Reiss, *Scientific reports* **2015**, *5*, 8945.

[19] C. Heiliger, C. Franz, M. Czerner, *Physical Review B* **2013**, *87*, 224412.

[20] N. Liebing, S. Serrano-Guisan, K. Rott, G. Reiss, J. Langer, B. Ocker, H. W. Schumacher, *Journal of Applied Physics* **2012**, *111*, 07C520.

[21] C. López-Monís, A. Matos-Abiague, J. Fabian, *Physical Review B* **2014**, *89*, 054419.

[22] Y. Xu, W. Lin, S. Petit-Watelot, M. Hehn, H. Rinnert, Y. Lu, F. Montaigne, D. Lacour, S. Andrieu, S. Mangin, *Journal of Applied Physics* **2016**, *119*, 023907.

[23] N. Liebing, S. Serrano-Guisan, P. Krzysteczko, K. Rott, G. Reiss, J. Langer, B. Ocker, H. W. Schumacher, *Applied Physics Letters* **2013**, *102*, 242413.

[24] W. Lin, M. Hehn, L. Chaput, B. Negulescu, S. Andrieu, F. Montaigne, S. Mangin, *Nature Communications* **2012**, *3*, 744.

[25] J. M. Teixeira, J. D. Costa, J. Ventura, M. P. Fernandez-Garcia, J. Azevedo, J. P. Araujo, J. B. Sousa, P. Wisniowski, S. Cardoso, P. P. Freitas, *Applied Physics Letters* **2013**, *102*, 212413.

[26] B. Geisler, P. Kratzer, *Physical Review B* **2015**, *92*, 144418.

[27] U. Sivan, Y. Imry, *Physical Review B* **1986**, *33*, 551–558.

[28] R. Gross, A. Marx, *Festkörperphysik*, Oldenbourg Wissenschaftsverlag, **2012**.

[29] S. Yuasa, *Journal of the Physical Society of Japan* **2008**, *77*, 031001.

[30] J. Slonczewski, *Physical Review B* **1989**, *39*, 6995–7002.

[31] N. W. Ashcroft, N. D. Mermin, *Solid state physics*, Saunders College, **1976**.

[32] W. H. Butler, X.-G. Zhang, T. C. Schulthess, J. M. MacLaren, *Phys. Rev. B* **2001**, *63*, 54416.

[33] X.-G. Zhang, W. H. Butler, *Journal of Physics: Condensed Matter* **2003**, *15*, R1603.

[34] S. Yuasa, T. Nagahama, A. Fukushima, Y. Suzuki, K. Ando, *Nature Materials* **2004**, *3*, 868–871.

[35] S. Yuasa, A. Fukushima, H. Kubota, Y. Suzuki, K. Ando, *Applied Physics Letters* **2006**, *89*, 87–90.

[36] D. D. Djayaprawira, K. Tsunekawa, M. Nagai, H. Maehara, S. Yamagata, N. Watanabe, S. Yuasa, Y. Suzuki, K. Ando, *Applied Physics Letters* **2005**, *86*, 1–3.

[37] S. Ikeda, J. Hayakawa, Y. Ashizawa, Y. M. Lee, K. Miura, H. Hasegawa, M. Tsunoda, F. Matsukura, H. Ohno, *Applied Physics Letters* **2008**, *93*, 15–18.

[38] W. Wang, H. Sukegawa, R. Shan, S. Mitani, K. Inomata, *Applied Physics Letters* **2009**, *95*, 182502.

[39] H. Sukegawa, H. Xiu, T. Ohkubo, T. Furubayashi, T. Niizeki, W. Wang, S. Kasai, S. Mitani, K. Inomata, K. Hono, *Applied Physics Letters* **2010**, *96*, 12–15.

[40] T. Tanaka, T. Arakawa, K. Chida, Y. Nishihara, D. Chiba, K. Kobayashi, T. Ono, H. Sukegawa, S. Kasai, S. Mitani, *Applied Physics Express* **2012**, *5*, 2–5.

[41] R. Pelster, *Physik und Didaktik in Schule und Hochschule* **2005**, *1*, 10–22.

[42] J. Jäckle, *The origin of the termoelectric potential*, Department of Physics, University of Konstanz, http://www.uni-konstanz.de/FuF/Physik/Jaeckle/, **2011**.

[43] K. Uchida, S. Takahashi, K. Harii, J. Ieda, W. Koshibae, K. Ando, S. Maekawa, E. Saitoh, *Nature* **2008**, *455*, 778–781.

[44] D. J. Griffiths, *Introduction to Quantum Mechanics*, Pearson Prentice Hall, **2005**.

[45] D. Comtesse, B. Geisler, P. Entel, P. Kratzer, L. Szunyogh, *Physical Review B - Condensed Matter and Materials Physics* **2014**, *89*, 094410.

[46] C. Kittel, *Introduction to solid state physics, 77th edition*, Wiley India Pvt. Limited, **2007**.

[47] C. Heiliger, P. Zahn, B. Y. Yavorsky, I. Mertig, *Physical Review B* **2006**, *73*, 214441.

[48] M. Bachmann, M. Czerner, C. Heiliger, *Journal of Electronic Materials* **2011**, *40*, 577–582.

[49] M. Czerner, C. Heiliger, *Journal of Applied Physics* **2012**, *111*, 07C511.

[50] M. Walter, *PhD Thesis*, Georg-August-Universität Göttingen, **2013**.

[51] M. Münzenberg, A. Thomas, *Physik in unserer Zeit* **2012**, *43*, 288–295.

[52] S. Curtarolo, W. Setyawan, S. Wang, J. Xue, K. Yang, R. H. Taylor, L. J. Nelson, G. L. Hart, S. Sanvito, M. Buongiorno-Nardelli, N. Mingo, O. Levy, *Computational Materials Science* **2012**, *58*, 227–235.

[53] N. Papanikolaou, R. Zeller, P. H. Dederichs, *Journal of Physics: Condensed Matter* **2002**, *14*, 2799–2823.

[54] R. Zeller, P. H. Dederichs, B. Újfalussy, L. Szunyogh, P. Weinberger, *Physical Review B* **1995**, *52*, 8807–8812.

[55] F. Heusler, *Verhandlungen der Deutschen Physikalischen Gesellschaft 5*, **1903**, p. 220.

[56] F. Heusler, *Verhandlungen der Deutschen Physikalischen Gesellschaft 5*, **1903**, p. 219.

[57] A. J. Bradley, J. W. Rodgers, *Proceedings of the Royal Society A: Mathematical Physical and Engineering Sciences* **1934**, *144*, 340–359.

[58] O. Heusler, *Annalen der Physik* **1934**, *411*, 155–201.

[59] I. Galanakis, P. H. Dederichs, N. Papanikolaou, *Physical Review B* **2002**, *66*, 174429.

[60] B. Balke, S. Ouardi, T. Graf, J. Barth, C. G. Blum, G. H. Fecher, A. Shkabko, A. Weidenkaff, C. Felser, *Solid State Communications* **2010**, *150*, 529–532.

[61] R. J. Gripshover, J. B. VanZytveld, J. Bass, *Physical Review* **1967**, *163*, 598–603.

[62] W. Fulkerson, J. P. Moore, D. L. McElroy, *Journal of Applied Physics* **1966**, *37*, 2639–2653.

[63] *elk*, `http://elk.sourceforge.net`.

[64] H. Ebert in *Electronic Structure and Physical Properies of Solids: The Uses of the LMTO Method* (Ed.: H. Dreyssé), Springer Berlin Heidelberg, Berlin, Heidelberg, **2000**, pp. 191–246.

[65] C. Sterwerf, *Diploma Thesis Bielefeld University* **2012**.

[66] M. Meinert, J.-M. Schmalhorst, M. Glas, G. Reiss, E. Arenholz, T. Böhnert, K. Nielsch, *Physical Review B* **2012**, *86*, 054420.

[67] S. Picozzi, A. Continenza, A. J. Freeman, *Physical Review B* **2004**, *69*, 094423.

[68] V. Popescu, P. Kratzer, D. Köderitzsch, H. Ebert, *Verhandlungen der DPG Frühjahrstagung Regensburg*, **2016**, p. MA 35.5.

[69] M. Czerner, C. Heiliger, *Journal of Applied Physics* **2012**, *111*, 07C511.

[70] J. M. Khosrofian, B. A. Garetz, *Applied Optics* **1983**, *22*, 3406.

[71] Y. Suzaki, A. Tachibana, *Applied optics* **1975**, *14*, 2809–10.

[72] P. LeClair, PhD thesis, Technische Universiteit Eindhoven, **2002**.

[73] Stanford Research Systems, *Manual - Model SR850 DSP Lock-In Amplifier*, Stanford Research Systems, 1290-D Reamwood Avenue, Sunnyvale, California 94089, **1992**.

[74] P. Rai-Choudhury, *Handbook of Microlithography, Micromachining, and Microfabrication: Microlithography*, SPIE Optical Engineering Press, **1997**.

[75] C. Sterwerf, M. Meinert, J.-M. Schmalhorst, G. Reiss, *IEEE Transactions on Magnetics* **2013**, *49*, 4386–4389.

[76] G. Eilers, H. Ulrichs, M. Münzenberg, A. Thomas, K. Thiel, M. Seibt, *Journal of Applied Physics* **2009**, *105*, 073701.

[77] M. J. Carey, N. Smith, B. A. Gurney, J. R. Childress, T. Lin, *Journal of Applied Physics* **2001**, *89*, 6579–6584.

[78] H. Schuhmann, M. Seibt, V. Drewello, A. Thomas, V. Zbarsky, M. Walter, M. Münzenberg, *arXiv:1405.1907* **2014**.

[79] R. Allmann, A. Kern, *Röntgen-Pulverdiffraktometrie: Rechnergestützte Auswertung, Phasenanalyse und Strukturbestimmung*, Springer Berlin Heidelberg, **2013**.

[80] B. D. Cullity, *Elements of X-ray Diffraction*, Addison-Wesley Publishing Company, **1956**.

[81] J. Als-Nielsen, D. McMorrow, *Elements of Modern X-ray Physics*, Wiley, **2011**.

[82] L. G. Parratt, *Physical Review* **1954**, *95*, 359–369.

[83] V. Holy, J. Kubeena, I. Ohlidal, K. Lischka, W. Plotz, *Physical Review B* **1993**, *47*, 15896–15903.

[84] J. Shiomi, K. Esfarjani, G. Chen, *Physical Review B* **2011**, *84*, 104302.

[85] C. S. Lue, Y.-K. Kuo, *Physical Review B* **2002**, *66*, 085121.

[86] A. Bentouaf, F. E. H. Hassan, *Journal of Magnetism and Magnetic Materials* **2015**, *381*, 65–69.

[87] H. C. Kandpal, PhD thesis, Johannes Gutenberg-Universität Mainz, **2006**.

[88] X.-Q. Chen, R. Podloucky, P. Rogl, *Journal of Applied Physics* **2006**, *100*, 113901.

[89] C. Papusoi, R. Sousa, J. Herault, I. L. Prejbeanu, B. Dieny, *New J. Phys.* **2008**, *10*, 103006.

[90] S. C. Beecher, R. B. Dinwiddie, A. M. Abeel, R. A. Lowden, *The thermal conductivity of silicon nitride with molybdenum disilicide additions*, Technomic Publishing Company, **1994**.

[91] B. L. Zink, B. Revaz, J. J. Cherry, F. Hellman, *Rev.Sci. Instrum.* **2005**, *76*, 24901.

[92] Q. G. Zhang, B. Y. Cao, X. Zhang, M. Fujii, K. Takahashi, *Phys. Rev. B* **2006**, *74*, 134109.

[93] S. M. Lee, D. G. Cahill, T. H. Allen, *Physical Review B* **1995**, *52*, 253–257.

[94] J. Chase, M.W., *Journal of Physical and Chemical Reference Data* **1998**, 1–1951.

[95] J. F. Shackelford, W. Alexander, *CRC Materials Science and Engineering Handbook, Third Edition*, CRC Press, 3rd ed., **2010**, p. 1980.

[96] J. Zhang, M. Bachman, M. Czerner, C. Heiliger, *Physical Review Letters* **2015**, *115*, 037203.

[97] Intel, *Intel® CoreTM i7 Processor Family for LGA2011 Socket*, `http://www.intel.com/content/dam/www/public/us/en/documents/datasheets/4th-gen-core-i7-lga2011-datasheet-vol-1.pdf`.

[98] C. Heiliger, P. Zahn, B. Yavorsky, I. Mertig, *Physical Review B* **2005**, *72*, 180406.

[99] H. Boeve, E. Girgis, J. Schelten, J. De Boeck, G. Borghs, *Applied Physics Letters* **2000**, *76*, 1048.

[100] T. Bohnert, V. Vega, A.-K. Michel, V. M. Prida, K. Nielsch, *Applied Physics Letters* **2013**, *103*, 092407.

[101] J. Ludwig, *Bachelor Thesis*, Bielefeld University, **2015**.

[102] A. Kato, N. Tamari, *Journal of Crystal Growth* **1975**, *29*, 55–60.

[103] D. Ebke, PhD thesis, Bielefeld University, **2010**.

[104] S. Wurmehl, G. H. Fecher, H. C. Kandpal, V. Ksenofontov, C. Felser, H.-J. Lin, J. Morais, *Physical Review B* **2005**, *72*, 184434.

[105] H. X. Liu, Y. Honda, T. Taira, K. I. Matsuda, M. Arita, T. Uemura, M. Yamamoto, *Applied Physics Letters* **2012**, *101*, 132418.

[106] S. Ikeda, J. Hayakawa, Y. Ashizawa, Y. M. Lee, K. Miura, H. Hasegawa, M. Tsunoda, F. Matsukura, H. Ohno, *Applied Physics Letters* **2008**, *93*, 082508.

[107] Y. Miura, S. Muramoto, K. Abe, M. Shirai, *Physical Review B* **2012**, *86*, 024426.

[108] T. Huebner, A. Boehnke, U. Martens, A. Thomas, J.-M. Schmalhorst, G. Reiss, M. Münzenberg, T. Kuschel, *arXiv:1604.07569* **2016**.

[109] D. G. Cahill, *Review of Scientific Instruments* **2004**, *75*, 5119–5122.

[110] J. Liu, G. M. Choi, D. G. Cahill, *Journal of Applied Physics* **2014**, *116*, 233107.

[111] G.-M. Choi, C.-H. Moon, B.-C. Min, K.-J. Lee, D. G. Cahill, *Nature Physics* **2015**, *11*, 576–581.

[112] H. Elsayed-Ali, T. Norris, M. Pessot, G. Mourou, *Physical review letters* **1987**, *58*, 1212–1215.

[113] H. Gu, X. Zhang, H. Wei, Y. Huang, S. Wei, Z. Guo, *Chemical Society reviews* **2013**, *42*, 5907–5943.

[114] V. A. Dediu, L. E. Hueso, I. Bergenti, C. Taliani, *Nature Materials* **2009**, *8*, 707–716.

[115] W. J. M. Naber, M. F. Craciun, J. H. J. Lemmens, A. H. Arkenbout, T. T. M. Palstra, A. F. Morpurgo, W. G. van der Wiel, *Organic Electronics* **2010**, *11*, 743–747.

[116] K. P. Pernstich, B. Rössner, B. Batlogg, *Nature Materials* **2008**, *7*, 321–325.

[117] W. J. M. Naber, S. Faez, W. G. van der Wiel, *Journal of Physics D: Applied Physics* **2007**, *40*, R205–R228.

[118] G. Szulczewski, S. Sanvito, M. Coey, *Nature Materials* **2009**, *8*, 693–5.

[119] G. Horowitz, *Advanced Materials* **1998**, *10*, 365–377.

[120] V. Dediu, M. Murgia, F. C. Matacotta, C. Taliani, S. Barbanera, *Solid State Communications* **2002**, *122*, 181–184.

[121] K. Bagschik, *Diploma thesis*, Bielefeld University, **2013**.

[122] E. Hall, *American Journal of Mathematics* **1879**, *2*, 287–292.

[123] D. Meier, PhD thesis, Bielefeld University, **2015**.

[124] A. v. Ettingshausen, W. Nernst, *Annalen der Physik* **1886**, *265*, 343–347.

[125] H. Kurt, K. Rode, P. Stamenov, M. Venkatesan, Y.-C. Lau, E. Fonda, J. M. D. Coey, *Physical Review Letters* **2014**, *112*, 027201.

[126] N. Thiyagarajah, Y.-C. Lau, D. Betto, K. Borisov, J. M. D. Coey, P. Stamenov, K. Rode, *Applied Physics Letters* **2015**, *106*, 122402.